Argonne National Laboratory

REACTOR DEVELOPMENT PROGRAM
PROGRESS REPORT

January 1970

The facilities of Argonne National Laboratory are owned by the United States Government. Under the terms of a contract (W-31-109-Eng-38) between the U. S. Atomic Energy Commission, Argonne Universities Association and The University of Chicago, the University employs the staff and operates the Laboratory in accordance with policies and programs formulated, approved and reviewed by the Association.

ARGONNE NATIONAL LABORATORY
9700 South Cass Avenue
Argonne, Illinois 60439

REACTOR DEVELOPMENT PROGRAM
PROGRESS REPORT

January 1970

Robert B. Duffield, Laboratory Director
Alfred Amorosi, Assistant Laboratory Director

Division	Director
Chemical Engineering	R. C. Vogel
EBR-II Project	M. Levenson
Materials Science	P. G. Shewmon
Reactor Engineering	L. J. Koch
Applied Physics	R. Avery

Report coordinated by
A. Glassner and A. D. Rossin

Issued February 25, 1970

FOREWORD

The Reactor Development Program Progress Report, issued monthly, is intended to be a means of reporting those items of significant technical progress which have occurred in both the specific reactor projects and the general engineering research and development programs. The report is organized in accordance with budget activities in a way which, it is hoped, gives the clearest, most logical overall view of progress. Since the intent is to report only items of significant progress, not all activities are reported each month. In order to issue this report as soon as possible after the end of the month editorial work must necessarily be limited. Also, since this is an informal progress report, the results and data presented should be understood to be preliminary and subject to change unless otherwise stated.

The issuance of these reports is not intended to constitute publication in any sense of the word. Final results either will be submitted for publication in regular professional journals or will be published in the form of ANL topical reports.

The last six reports issued
in this series are:

July 1969	ANL-7595
August 1969	ANL-7606
September 1969	ANL-7618
October 1969	ANL-7632
November 1969	ANL-7640
December 1969	ANL-7655

REACTOR DEVELOPMENT PROGRAM

Highlights of Project Activities for January 1970

EBR-II

The reactor was operated for 817 MWd during the reporting period, bringing its cumulative operational total to 31,027 MWd.

The Test-2 (fueled) instrumented subassembly completed its first in-reactor run on January 10 and is now in its second run. All sensors are performing satisfactorily. Except for the temperatures at the centerlines of the fuel pins, the measured temperatures are very close to the projected temperatures. The centerline temperatures are lower than projected. The reason for this difference is being sought.

Electron-microprobe examination of the stainless steel cans which contained graphite in materials-surveillance subassembly SURV-2 revealed no evidence of interaction between the stainless steel and the graphite.

ZPR-3

Upon the completion of the analysis of the radial perturbation traverses with Pu-239 and U-238 and the central perturbation measurements, experimental work with the benchmark plutonium-carbon Assembly 58 was concluded. In the lead-reflected Assembly 59, basic measurements, including that of the natural-uranium Doppler coefficient, were made, but have not yet been analyzed.

Following this, pre-loading of Assembly 60, an EBR-II mockup, was begun.

ZPR-9

FTR-3, the first plutonium-fueled fast spectrum reactor to be built at the Illinois Site (Assembly 26 of ZPR-9) achieved initial criticality on January 9, 1970. The critical mass was 537 kg of fissile plutonium, in reasonable agreement with predicted critical mass. Further reactor modifications needed for plutonium operation resulted in a temporary interruption of scheduled operation.

Data reduction and analysis of results obtained earlier with three null zones in Assembly 25 is still in progress.

ZPPR

The computer-controlled ZPPR counting-room gamma-spectroscopy system is now in full operation. Foil-counting throughput is expected to lie between 30 and 150 foils per day. An early application of this equipment was to the measurement of manganese- and sodium-activation traverses made in the ZPPR/FTR-2 shield configuration.

Following a period of shutdown maintenance, loading of the ZPPR Assembly 2, a 2600-liter core with a calculated critical mass of 1250 kg of plutonium, was begun.

TABLE OF CONTENTS

TABLE OF CONTENTS

I. LIQUID METAL FAST BREEDER REACTORS--CIVILIAN

A. Physics Development--LMFBR

1. Theoretical Reactor Physics

a. General Fast Reactor Physics

(i) Reactor Dynamics (D. A. Meneley)

Last Reported: ANL-7555, pp. 1-4 (Dec 1969).

An undetermined-parameter method,* developed to integrate the multimode kinetics equation, is known to overcome the limitations of time-step size of finite difference methods, but the extent of this improvement for space-time kinetics is not known. In an attempt to establish the degree of superiority of the undetermined-parameter method, some numerical calculations were made, with the results presented below.

The transient analyzed is initiated by a ramp increase in fission cross section for 0.1 sec in the inner 15 cm of the reactor described by Fuller.* The transient is terminated at t = 1.0 sec, by which time $1.23 in reactivity has been inserted. The initial and final flux shapes are shown in Fig. I.A.1. These are used as trial and weighting functions in a spatial weighted residual procedure (that results in the formation of the multimode kinetics equations) to obtain the results shown in Fig. I.A.2 and Table I.A.1. It should be noted that, in all cases, the correct flux shape was selected by the weighted residual procedure.

Figure I.A.2 shows the amplitude function (see Eq. 8.1 of Fuller) at the end of the ramp, versus the average time-step size, for various choices of polynomial trial functions for the temporal integration. WIGLE uses a finite-difference method for time integration, so that a linear variation in the amplitude function is assumed over the time step. Note, then, that the undetermined-parameter method is intrinsically more efficient because much larger time steps can be taken, even with linear trial functions, to obtain an accurate solution.

Fig. I.A.1. Shape Functions

*Fuller, E. L., III, ANL-7565 (1969).
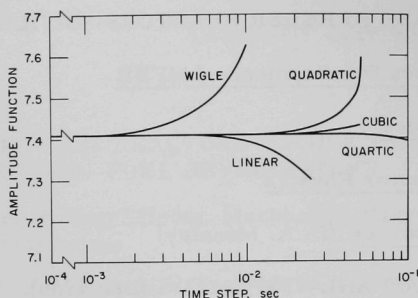
Fig. I.A.2

Amplitude Functions at
t = 0.1 sec vs Average
Time-step Size

TABLE I.A.1. Results at t = 1 sec for Two Modes

ϵ_1	Linear	Quadratic	Cubic	Quartic
		Amplitude Function		
1.0	4.20×10^{15}	1.13×10^{11}	6.37×10^{12}	4.22×10^{12}
0.1	5.34×10^{12}	1.11×10^{11}	4.06×10^{12}	3.94×10^{12}
0.01	4.22×10^{12}	3.93×10^{12}	3.94×10^{12}	3.94×10^{12}
0.001	3.95×10^{12}	3.94×10^{12}	3.94×10^{12}	3.94×10^{12}
		Time Steps		
1.0	21	11	11	25
0.1	78	14	30	131
0.01	180	90	54	137
0.001	727	183	98	159

WIGLE: 3.94×10^{12} for 2000 time steps.

   Some results at the end of the transient (t = 1.0 sec) are
shown in Table I.A.1. The parameter ϵ_1 is a measure of degree of con-
vergence in the procedure for time-step selection and is defined in
Fuller's Appendix B. The results are generally similar to those shown in
Fig. I.A.1. However, two pitfalls can be found by using the table. First, a
loose ϵ_1 can lead to unexpectedly large inaccuracies, as can be seen for
ϵ_1 = 1.0 and 0.1 with quadratic trial functions. Second, the method may
take overly small time steps (presumably to correct round-off errors)
when the degree of the trial polynomial becomes large (such as quartic).
Accuracy is not impaired, however.

   From this limited study, one could conclude that cubic
trial functions provide an optimum choice to obtain the most accurate

solutions in the most efficient manner. Quadratic trial functions, however, do nearly as well as far as computer time is concerned.

2. Experimental Reactor Physics

a. Fast Critical Experiments--Experimental Support--Idaho

(i) Development of Experimental Techniques (S. G. Carpenter)

Last Reported: ANL-7460, pp. 13-17 (Nov 1969).

(a) ZPPR Counting-room Gamma-spectroscopy System.
The ZPPR counting-room gamma-spectroscopy system is now in full operation. The basic system is composed of three lithium-drifted-germanium detectors with sample changers, three analog-to-digital converters, one small computer for data acquisition and system control, one storage oscilloscope for data display, and one incremental magnetic tape for data storage. Amplifiers, preamplifiers, live timers, high-voltage supplies, and a teletype unit complete the list of main-system components.

The gamma-spectroscopy system is presently operational in one of the two modes, either as a single multichannel analyzer or as three multichannel analyzers. The computer provides complete control of the system after the initial conditions are set. These initial conditions consist of selecting the proper controls on the amplifiers, analog-to-digital converters, and timers, entering, via the teletype, an 8-character identification code, the date, the starting time, the maximum counting interval allowed (in minutes), and the number of spectra to be accumulated.

For the single-multichannel-analyzer mode, additional entries include the detector chain to be used and the data area to be accumulated. The data area is comprised of 53 blocks of 64 channels each, and these can be selected from any portion of the incoming 8192-channel spectrum. For the three-multichannel-analyzer mode, a data area composed of 15 blocks of 64 channels must be specified for each of the three detector chains.

After the program is started and the initial conditions specified, the magnetic tape unit is interrogated and reset, and the sample changers are tested to see if a sample is in position to be counted. If the sample changers are not ready, the program waits until they are ready before executing the remainder of the program. The program then continues on to read and store the sample numbers, reset the live timers, and start accumulating data.

Data accumulation continues until all the live timers have stopped or the maximum counting time is reached. The data is then

displayed on a storage oscilloscope, if desired, and written on magnetic tape. The live timer "time" is also written on the magnetic tape along with the real (clock) start and stop time for each counting chain. The sample changers are also commanded to change samples, and then the program either goes back to the point of checking the sample changers or terminates, depending on sense-switch options.

The counting system also has available two small NaI detectors, and a lithium-drifted-silicon detector for beta and alpha counting or spectroscopy. These detectors can be used with the sample changers instead of the Ge(Li) detectors, or in coincidence with the Ge(Li) detectors if the experiment requires such a system. A 3 x 3-in. NaI detector and a small Ge(Li) are also available for use in a standard (3 x 3 x 3-ft) lead cave.

Experience to date indicates that foil-counting through-put, using the Ge(Li) detectors, could go as high as 150 foils per day for well-activated, short-half-life foils (such as manganese), and as low as 30 foils per day for fission product foils. This is well within the original design parameter of 200 to 300 foils per week.

Data analysis is presently being accomplished with the ZPPR computer (SEL-840). The limited size of this computer requires the analysis to be done in three steps, and this will probably increase to four or five steps as further modifications and improvements are made.

(ii) Selected Differential and Integral Data (S. G. Carpenter)

Not previously reported.

(a) Measurements of Manganese and Sodium Activation in ZPPR/FTR-2 Shield Configuration. A series of radial manganese- and sodium-activation traverses were performed at six axial elevations in the ZPPR/FTR-2 shield configuration (see Progress Report for October 1969, ANL-7632, pp. 14-22), both with and without fuel in the shield. The sodium was contained in standard 1/4 x 2 x 2-in. stainless steel-clad cans each of which contained 11.5 g of sodium metal on the average. Manganese was in the form of Mn-20% Cu alloy in circular foils measuring a nominal 0.005 in. thick by 0.500 in. in diameter, containing on the average 0.119 g manganese.

The principle azimuthal direction of the traverses was along the centerline of the partially represented shield. In the "fuel out" configuration, an additional radial traverse was performed at 90° to this, a direction in which the shield was not represented.

The capture reactions ^{23}Na$(n,\gamma)^{24}$Na and ^{55}Mn$(n,\gamma)^{56}$Mn were assessed from the gammas which follow beta decay, using the Ge(Li) spectroscopy system of the ZPPR Counting Facility. The gamma activity was measured in a series of short counts of each foil, interspersed with counts of all other samples, over a period which approached a half-life in some cases. This procedure allowed nearly all factors directly affecting counting precision to be evaluated directly. (Such effects include timing errors, live-timer accuracy, and nonreproducibility of counting geometry, as well as the usual nuclear-decay statistics.)

The resulting multichannel spectra were evaluated by the RAID Code (see Progress Report for November 1969, ANL-7640, pp. 17-18). This locates each peak, subtracts the underlying Compton background, and combines and statistically evaluates the repeated counts. The span of the measurement included at least two gamma rays for each isotope, further broadening the statistical basis on which the precision was assessed.

The results presented in Tables I.A.2, I.A.3, and I.A.4 are expressed in terms of the absolute disintegration rate at the time of reactor shutdown. No corrections have been made for gamma-ray attenuation or neutron self-shielding. Counting efficiency for each detector system was determined relative to a set of calibrated standard sources.

The manganese results are referred to the 846.8-keV gamma ray, with an assumed absolute transition intensity of 0.987 gamma/disintegration. The sodium activations are referred to the 1368.526-keV gamma ray, with an assumed absolute transition intensity of 1.00 gamma/disintegration. The counting geometry for the sodium plates differed considerably from that for which the efficiency calibration was established. Estimates, both internal and external to the present data, indicate that the geometric efficiency factor relative to the manganese was 1.27 ± 0.13, the sodium being counted more efficiently. This correction was not applied.

The uncertainties expressed in the tables are derived from nuclear counting statistics and observed nonreproducibilities, and represent one standard deviation in the precision of the counting measurement. They fairly represent the relative uncertainties within each (manganese or sodium) group of data. In addition to this, the absolute efficiency of the counting system is uncertain by a systematic 10%. In comparing the sodium and manganese traverses, there is an additional possibility of a 10% systematic error due to the differences in counting geometry.

All measurements reported here were done in two irradiations: Run 248 with fuel in the shield, and Run 250 without fuel in the shield. Each lasted 48 min.

6

TABLE I.A.2. Manganese and Sodium Activations: ZPPR/FTR-2 Shield
Configuration with Fuel in Shield Traverses along Row 37, Half 1[a]

Axial Elevation (in.)	Radius[b] (in.)	Absolute Manganese Disintegration Rates[c] (x 10^8 hr^{-1} g^{-1})	Absolute Sodium Disintegration Rates[c,d] (x 10^6 hr^{-1} g^{-1})
3	0.25	106.18 ± 0.21	51.65 ± 0.16
	4.60	95.02 ± 0.77	47.43 ± 0.21
	13.23	51.40 ± 0.22	37.38 ± 0.11
	21.98	55.17 ± 0.21	30.86 ± 0.44
	23.28	88.41 ± 0.24	45.46 ± 0.45
	27.62	115.77 ± 0.50	48.12 ± 0.31
	34.14	56.27 ± 0.18	26.58 ± 0.22
	43.46	13.590 ± 0.080	7.813 ± 0.065
	52.40	2.3664 ± 0.0090	1.153 ± 0.013
	56.75	1.152 ± 0.022	0.610 ± 0.022
7	43.46	13.113 ± 0.088	7.352 ± 0.054
	52.40	2.3600 ± 0.0077	1.045 ± 0.013
	56.75	1.160 ± 0.022	0.5834 ± 0.0095
11	43.46	12.05 ± 0.13	7.225 ± 0.059
	52.40	2.117 ± 0.021	0.924 ± 0.014
	56.75	1.1007 ± 0.0072	0.558 ± 0.010
14	0.25	88.18 ± 0.67	41.33 ± 0.43
	4.60	78.28 ± 0.36	37.64 ± 0.29
	13.29	43.98 ± 0.13	28.15 ± 0.18
	21.98	44.02 ± 0.23	23.57 ± 0.28
	23.28	66.68 ± 0.27	33.87 ± 0.14
	27.62	83.16 ± 0.28	38.28 ± 0.14
	34.14	41.12 ± 0.19	19.998 ± 0.076
	43.46	10.714 ± 0.047	6.11 ± 0.14
	52.40	2.084 ± 0.025	0.913 ± 0.024
	56.75	1.087 ± 0.066	0.514 ± 0.011
17	43.46	9.399 ± 0.032	5.471 ± 0.054
	52.40	2.205 ± 0.020	0.970 ± 0.016
	56.75	1.2047 ± 0.0072	0.5721 ± 0.0092
22	0.125	123.60 ± 0.99	45.48 ± 0.23
	4.47	119.91 ± 0.28	45.43 ± 0.46
	13.16	99.76 ± 0.83	36.71 ± 0.50
	21.86	73.97 ± 0.23	29.518 ± 0.068
	23.28	71.30 ± 0.26	31.37 ± 0.15
	27.62	51.63 ± 0.14	25.64 ± 0.16
	34.14	24.95 ± 0.16	12.708 ± 0.058
	43.46	7.317 ± 0.042	4.399 ± 0.066
	52.40	3.0606 ± 0.0085	1.633 ± 0.019
	56.75	1.8159 ± 0.0047	0.970 ± 0.014

[a]Refer to Fig. I.A.7 of Progress Report for October 1969, ANL-7632, p. 21.
[b]At center of 1/4 x 2 x 2-in. sodium can. Manganese radii are 1/8 in. less.
[c]At time of reactor shutdown.
[d]Geometric relative counting efficiency factor relating sodium cans to calibrated foil geometry is 1.27 ± 0.13.

6

TABLE I.A.3. Manganese and Sodium Activations: ZPPR/FTR-2 Shield
Configuration without Fuel in Shield Traverses along Row 37, Half 1[a]

Axial Elevation (in.)	Radius[b] (in.)	Absolute Manganese Disintegration Rates[c] (x 10^8 hr^{-1} g^{-1})	Absolute Sodium Disintegration Rates[c,d] (x 10^6 hr^{-1} g^{-1})
3	0.25	105.23 ± 0.58	53.41 ± 0.24
	4.60	93.49 ± 0.33	50.95 ± 0.20
	13.29	50.47 ± 0.33	39.47 ± 0.37
	21.98	55.25 ± 0.52	32.72 ± 0.29
	27.62	117.93 ± 0.33	53.32 ± 0.11
	34.15	56.12 ± 0.35	27.67 ± 0.26
	43.46	13.581 ± 0.086	8.280 ± 0.068
	52.15	5.378 ± 0.021	3.032 ± 0.029
	56.50	2.988 ± 0.015	1.685 ± 0.033
7	13.29	44.82 ± 0.18	33.44 ± 0.10
	21.98	48.53 ± 0.13	27.89 ± 0.085
	43.46	12.763 ± 0.067	6.813 ± 0.058
	52.15	5.014 ± 0.031	2.652 ± 0.075
11	13.29	43.43 ± 0.16	31.34 ± 0.17
	21.98	46.61 ± 0.14	25.97 ± 0.25
	43.46	12.17 ± 0.23	6.828 ± 0.024
	52.15	4.748 ± 0.071	2.636 ± 0.011
14	0.25	88.56 ± 0.43	38.92 ± 0.22
	4.60	77.24 ± 0.46	36.30 ± 0.14
	13.29	43.47 ± 0.12	28.69 ± 0.11
	21.98	43.76 ± 0.22	23.84 ± 0.32
	27.62	85.74 ± 0.22	37.27 ± 0.40
	34.14	40.81 ± 0.33	19.48 ± 0.054
	43.46	10.69 ± 0.028	6.335 ± 0.044
	52.15	4.296 ± 0.017	2.463 ± 0.0058
	56.50	2.541 ± 0.013	1.440 ± 0.047
17	13.29	53.18 ± 0.15	27.41 ± 0.20
	21.98	48.49 ± 0.13	22.73 ± 0.10
	43.46	9.535 ± 0.086	5.355 ± 0.086
	52.15	4.207 ± 0.024	2.145 ± 0.0097
22	0.125	122.22 ± 0.44	44.10 ± 0.18
	4.47	119.30 ± 0.57	41.83 ± 0.30
	13.16	99.43 ± 0.47	36.63 ± 0.30
	21.86	72.84 ± 0.35	28.59 ± 0.26
	27.62	50.60 ± 0.23	24.27 ± 0.13
	34.14	24.70 ± 0.15	12.31 ± 0.055
	43.46	7.120 ± 0.036	4.093 ± 0.055
	52.15	3.230 ± 0.032	1.925 ± 0.010
	56.50	2.087 ± 0.014	1.166 ± 0.029

[a]Refer to Fig. I.A.5 in Progress Report for October 1969, ANL-7632, p. 17.
[b]At center of 1/4 x 2 x 2-in. sodium can. Manganese radii are 1/8 in. less.
[c]At time of reactor shutdown.
[d]Geometric relative counting efficiency factor relating sodium cans to calibrated foil geometry is 1.27 ± 0.13.

TABLE I.A.4. Manganese and Sodium Activations: ZPPR/FTR-2
Shield Configuration without Fuel in Shield Traverse along
Column 37, Half 1[a] at Axial Elevation of 3 in.

Radius[b] (in.)	Absolute Manganese Disintegration Rates[c] (x 10^8 hr^{-1} g^{-1})	Absolute Sodium Disintegration Rates[c,d] (x 10^6 hr^{-1} g^{-1})
29.55	85.34 ± 0.24	40.11 ± 0.26
38.64	13.59 ± 0.045	8.141 ± 0.066
47.73	8.114 ± 0.010	5.616 ± 0.030
56.83	5.645 ± 0.017	4.055 ± 0.11

[a]Refer to Fig. I.A.5 of Progress Report for October 1969,
ANL-7632, p. 17.
[b]At center of 1/4 x 2 x 2-in. sodium can. Manganese radii are
1/8 in. less.
[c]At time of reactor shutdown.
[d]Geometric relative counting efficiency factor relating sodium cans
to calibrated foil geometry is 1.27 ± 0.13.

Auxiliary absolute measurements of the Pu-239 fission
rate and Na-23 capture rates were made near core center in each run. The
results are given in Table I.A.5. The fission rates were determined with an
absolute counter. The sodium reaction rates were found by activation of a
nominally 0.125-in.-thick by 0.485-in.-dia NaCl pellet, which could be
counted in the standard geometry. The ratio of total irradiations of the two
reactor runs was 1.00, within the approximate 0.5% uncertainties, as meas-
ured by each of the two methods.

TABLE I.A.5. Measurements of Reaction Rate near Core Center

Reaction	Location			Absolute Reaction Rate (g^{-1} sec^{-1})	
	Radius (in.)	Elevation (in.)	Half	Run 248 (Fuel in Shield)	Run 250 (No Fuel in Shield)
^{239}Pu(n,F)F.P.[a]	0.0	1.00	1	(7.016 ± 0.14) x 10^7	(6.978 ± 0.14) x 10^7
^{23}Na(n,γ)^{24}Na[b]	0.75	1.00	2	(1.477 ± 0.0067) x 10^4	(1.486 ± 0.0075) x 10^4

[a]Quoted errors include those relating to absolute calibration.
[b]Absolute calibration of sodium measurements is uncertain by 10%.

b. Fast Critical Experiments--Experimental Support--Illinois

(i) Selected Differential and Integral Data (R. Gold)

Last Reported: ANL-7618, pp. 4-6 (Sept 1969).

(a) Absolute Measurement of $\nu(^{252}Cf)$. The need for accu-
rate measurements of the total yield of neutrons (ν) in spontaneous fission

has continued. Previous studies* of the fundamental fission constants indicate that the most consistent values of ν for thermal fission are based on ratio measurements with $\nu(^{252}Cf)$. Thus, the absolute measurement of the californium yield underlies all precision values of thermal-fission yields and also propagates as the tiepoint for the yield as a function of energy.

We have recently completed an evaluation of $\nu(^{252}Cf)$ based on absolute measurements of the neutron rate and fission rate from three fission chambers. This experiment, which incorporates advances over previous work,** was accomplished with a high degree of authentication.

The neutron-emission rate factor in the yield was found with the aid of a manganese-bath facility independently calibrated with reference to absolute beta-gamma coincidence counting of ^{56}Mn. The calibration capability was reinforced through a limited international comparison of activated manganese aliquots.

Special measurements were made of other subsidiary parameters, such as parasitic absorption by high-energy neutrons in sulfur and oxygen, the effective thermal cross-section ratio of hydrogen to manganese, and source-holder thermal absorption.

Precise support in the accuracy of the neutron assay was obtained from comparison with standard sources. For example, the independent Argonne value for the international Ra-Be(α,n) standard neutron source is $(3.223 \pm 0.0014) \times 10^6$ neutrons/sec compared to the international average† of $(3.230 \pm 0.030) \times 10^6$. For the U.S. secondary standard, NBS-II, the Argonne result is $(1.1776 \pm 0.0043) \times 10^6$, whereas the average from the National Bureau of Standards is $(1.177 \pm 0.012) \times 10^6$.

The fission rate from each counter was obtained primarily from absolute fission-neutron coincidence data, with special attention to angular-correlation effects. One chamber with fission-fragment efficiency of less than 70% and another of less than 90% had rather large angular-correlation effects, resulting in reduced confidence. The third chamber, though, provided over 99% fragment efficiency; even so, the measured angular-correlation effect was as much as 1%. The fission rate obtained with high precision from the coincidence experiments is supported by direct evaluation under conditions of a small well-defined solid angle.

---

*De Volpi, A., "Current Values of Fundamental Fission Parameters," Reactor and Fuel-Processing Technology 10(4), 271-288 (1967).

**De Volpi, A., and Porges, K. G., Proceedings of Conference on Nuclear Data for Reactors, International Atomic Energy Agency, Vienna (1967), Vol. I, p. 297.

† Naggiar, V., Metrologia 3, 51 (1967).

The resulting value of $\nu(^{252}\text{Cf}) = 3.725 \pm 0.015$ (total yield) is generally independent of cross sections, neutron-spectrum assumptions, counting statistics, and fission-fragment self-absorption. The error assigned is a combination of statistical and systematic effects at a confidence level of 68%.

Two controversial correction factors remain: these are for leakage compensation and for sulfur-oxygen parasitic absorption. The upper limit for each is about two-thirds of a percent in opposing directions.

The implications of this measurement, in context with past and other concurrent values, suggest that neutron yields for ^{235}U and ^{239}Pu are lower than previously accepted, possibly by about $1/2\%$.

c. FFTF Critical Assembly Experiments--Planning and Evaluation (A. Travelli)

Last Reported: ANL-7655, pp. 6-9 (Dec 1969).

(i) Calculation of Reaction-rate Traverses in ZPPR/FTR-2 Shield Configuration. The radial variation of the Na-23 capture rate has been computed for axial positions at 7.62, 35.56, and 55.88 cm from the dividing plane. The neutron fluxes used in the computations were obtained in the way described in ANL-7655 from a DIFF 2D* diffusion solution for the ZPPR/FTR-2 assembly in its shield configuration (loading 120). For computational simplicity in r,z-geometry the shield sector was extended azimuthally from 60 to 360°. Thus, the neutron fluxes were applicable only along radii far from the azimuthal boundaries of the shield sector and only for the condition of no fuel storage in the shield. The 29-energy-group cross-section set 25004 (see Progress Report for December 1968, ANL-7527, p. 9) was used, giving $k_{eff} = 0.9946$.

The traverses at 7.62 and 35.56 cm pass through the depleted zone, core, radial reflector, shield, and 5.53 cm of iron, which simulates the heavy clamp that holds the matrix tubes in position. The core-axial reflector interface is at 45.811 cm and the axial reflector ends at 76.302 cm. Thus, the traverse at 55.88 cm passes through the axial reflector for radii smaller than the core radius, then through the radial reflector, shield, and iron clamp.

Two reaction-rate curves were computed at 7.62 and 35.56 cm. The calculation of the first reaction rate used the 29-group cross sections obtained from a 2100-group fundamental mode MC²** flux averaging

_____

* Toppel, B. J., ANL-7332 (1967).

** Toppel, B. J., et al., ANL-7318 (1967).

for the core composition at criticality. Calculation of the second reaction-rate traverse used the 29-group cross sections obtained from a 2100-group fundamental mode MC^2 flux averaging for the radial reflector composition with zero buckling. The fluxes used for all traverses were normalized so that the Na-23 capture rate for the first calculation was unity at zero radius in the 7.62-cm traverse.

Two reaction-rate curves were also computed for each traverse at 55.88 cm. The calculation of the first reaction rate used cross sections averaged for the axial reflector composition with zero buckling. The calculation of the second reaction-rate traverse used cross sections averaged for the radial reflector composition.

The computed reaction rates are compared in Fig. I.A.3 with the experimental values [see Sect. I.A.2.a.(ii)]. The experimental data for no fuel stored in the shield are indicated by crosses, reaction rates obtained by core spectrum averaging are indicated by dotted curves labeled "1," reaction rates obtained by radial reflector spectrum averaging are indicated by dotted curves labeled "2," and reaction rates obtained by axial reflector spectrum averaging are indicated by dotted curves labeled "3." Thus, type-1 curves are valid close to the core center, and types -2 or 3 curves are valid well inside the radial or axial reflectors, respectively.

The calculated Na-23 capture reaction rate, shown in Fig. I.A.3, is not strongly dependent on the averaging of cross sections. The region of greatest disagreement between calculated and measured reaction rate is in the core, where the calculated reaction rate is 15% too high at one point.

Fig. I.A.3. Na-23 Capture Rate vs Radial Position in ZPPR/FTR-2 Shield Configuration

The shielding calculations reported above are preliminary and do not take into account several factors that might affect the results considerably. More complete analysis of the FTR shielding experiments will be reported.

3. ZPR-6 and -9 Operations and Analysis

   a.   Zoned Critical Experiments (L. G. LeSage and J. W. Daughtry)

Last Reported: ANL-7632, pp. 7-8 (Oct 1969).

   (i)   ZPR-9 Assembly 25 Experiments

The final loading arrangement for Assembly 25 is given in Fig. I.A.4, Progress Report for September 1969, ANL-7618, p. 10. The arrangements for loading number 24, given in Figs. I.A.4.a and b for the stationary and moveable halves, are considered the reference configuration for Assembly 25. The number 1 null zone was installed at this time, as were the fission counter drawers and the axial oscillator which were used throughout the measurements. The critical condition for the arrangement was with rod 9 withdrawn 29 cm and all other rods at their most reactive position. Equivalent cylindrical radii and the average atomic concentrations for each region are given in Table I.A.6.

The null atomic concentrations for each of the three null zones (as described in ANL-7632) are listed in Table I.A.7. These values were derived from the sample-box measurements closest to null and corrected to the exact null using the measured worths of the constituent materials. There are some differences between the null compositions listed in Table I.A.7 and the average compositions for the null zone listed in Table I.A.6. There are two primary reasons for the difference. The zone-averaged compositions are reduced some by the void introduced when the fission counters are included. In addition, the average weight of the aluminum pieces used in the null-zone drawers next to the buffer was somewhat less than the weight of the pieces used near the center of the zone and in the null sample.

Some preliminary calculations have been completed, and the calculated values of k_∞ for the null compositions of zones 1 and 2 are both approximately 0.94. The cross-section sets were derived from the current ENDF/B tape using the MC^2 code. Each cross-section set was also corrected for plate heterogeneity using S_n-derived fluxes. The calculated values of k_∞ for the previous null zones have also been too low (<1.0), but the discrepancy is largest in Assembly 25. This is probably due to the larger fraction of ^{238}U in this assembly, but a more complete discussion of the results must wait until all the information on this assembly is available.

(a) STATIONARY HALF

DEPLETED REFLECTOR

STAINLESS STEEL REFLECTOR

DRIVER

6

FAR

BUFFER

NULL ZONE

FC

7

AO

FC

10

8

9

(b) MOVEABLE HALF

DEPLETED REFLECTOR

STAINLESS STEEL REFLECTOR

DRIVER

B

BUFFER

FAR

NULL ZONE

FC

5

AO

FC

2

4

3

AC-AXIAL OSCILLATER   FAR - FINE AUTO ROD   I THROUGH IO-FUEL ROD

FC-FISSION COUNTER   B - BORON ROD
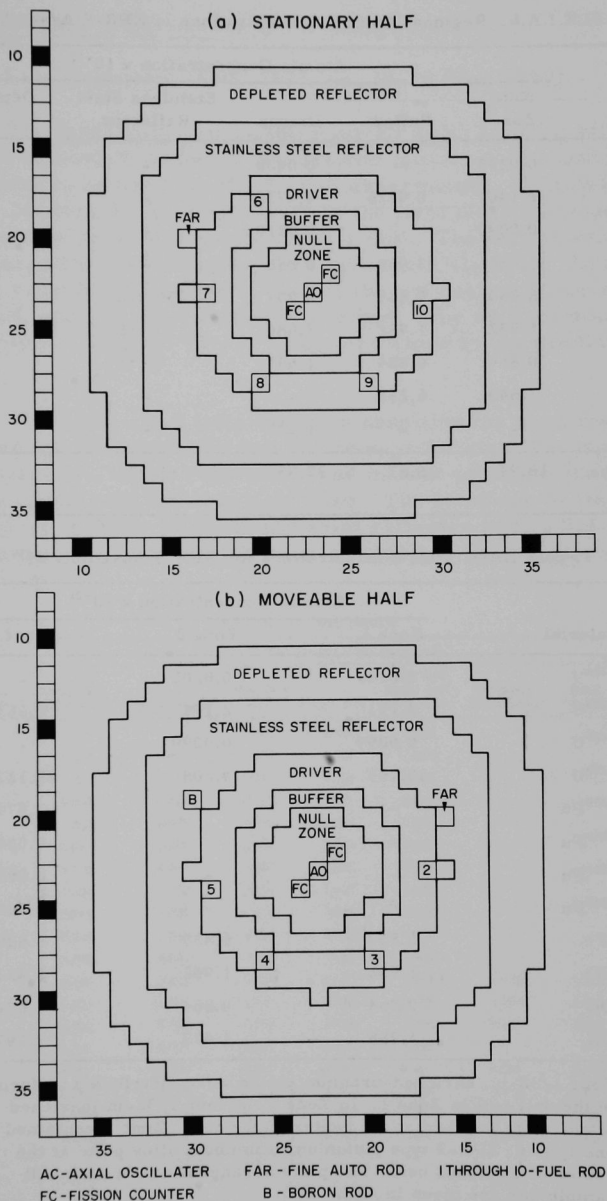
Fig. I.A.4. Loading Arrangement for ZPR-9 Assembly 25 (Loading 24)

14

TABLE I.A.6. Regional Atomic Concentrations in ZPR-9 Assembly 25

Material	Atomic Concentration x 10^{-21}				
	Null Zone	Buffer	Driver	Stainless Steel Reflector	Depleted-uranium Reflector
^{234}U	0.0203	-	0.0438	-	-
^{235}U	2.1401	0.0726	4.4737	-	0.081
^{236}U	0.0097	-	0.0210	-	-
^{238}U	33.234	33.959	0.255	-	39.93
Fe	6.839	6.839	12.907	56.472	4.332
Cr	1.952	1.952	3.684	16.115	1.14
Ni	0.864	0.864	1.631	7.136	0.54
Al	1.649	6.255	-	-	-
C	-	-	51.218	-	-
Region Radius (cm)	18.94	25.87	37.95	55.79	71.89

TABLE I.A.7. Null Concentrations for ZPR-9 Assembly 25[a]

Material	Atomic Concentration x 10^{-21}		
	Zone 1	Zone 2	Zone 3
^{234}U	0.0206	0.0206	-
^{235}U	2.173	2.174	0.0536
^{236}U	0.0099	0.0099	-
^{238}U	33.765	34.208	25.127
^{239}Pu	-	-	1.0749
^{240}Pu	-	-	0.0513
^{241}Pu	-	-	0.0049
^{242}Pu	-	-	0.00006
Fe	6.839	6.839	8.538
Cr	1.952	1.952	2.437
Ni	0.864	0.864	1.079
Al	1.785	1.477	2.197

[a]Four 1/32-in. enriched-uranium plates were distributed uniformly in the unit cell in Zone 1. In Zone 2 the four 1/32-in. enriched plates were bunched at the center of the cell. Zone 3 contained one 1/8-in. ZPR-3 type plutonium-aluminum alloy plate at the center of each unit cell. The plate arrangements in each null sample box are given in ANL-7632.

b.   <u>Mockup Experiments</u> (J. W. Daughtry)

Last Reported: ANL-7655, pp. 10-13 (Dec 1969).

(i) <u>Initial Critical Loading for FTR-3</u>. Loading of ZPR-9 Assembly 26 continued, based on the desired initial configuration for the critical system to be used for the FTR-3 experiments. Criticality was achieved on January 9. This assembly is the first plutonium-fueled fast-spectrum reactor to be built at the Illinois Site. The matrix and drawer-loading patterns for the assembly were given in ANL-7655. At criticality all ^{10}B rods were fully withdrawn, nine of the ten dual-purpose rods were fully inserted, and the tenth partially inserted. The critical mass was approximately 537.0 kg of ^{239}Pu + ^{241}Pu, very close to the predicted value of 537.4 kg.

Table I.A.8 lists the atom densities for each region of the assembly and for each drawer type, where appropriate. The inner-core Type A drawers are in the even-numbered matrix columns, the Type B drawers are in the odd-numbered columns. The locations of the ten ^{10}B rods were given in ANL-7655. In the axial reflector and radial reflector the spring gap at the rear of each front drawer has been neglected. This gap is 0.630 cm.

TABLE I.A.8. FTR-3 Atom Densities

Isotope or Element	Atom Densities (10^{21} atoms/cm^3)							
	Inner Core Type A Drawer	Inner Core Type B Drawer	Inner Core Avg[a]	Outer Core	Outer Core Drawer Next to ^{10}B Rods	Peripheral Control Zones	Radial Reflector	Axial Reflector
^{238}Pu	0.0006	-	0.0003	0.0006	0.0006	-	-	-
^{239}Pu	0.8814	1.0690	0.9784	1.4669	1.4466	-	-	-
^{240}Pu	0.1167	0.0510	0.0827	0.1723	0.1704	-	-	-
^{241}Pu	0.0181	0.0049	0.0113	0.0227	0.0225	-	-	-
^{242}Pu	0.0019	0.0001	0.0010	0.0022	0.0022	-	-	-
^{239}Pu + ^{241}Pu	0.8995	1.0739	0.9897	1.4896	1.4691	-	-	-
^{240}Pu + ^{242}Pu	0.1186	0.0511	0.0837	0.1745	0.1726	-	-	-
Pu	1.0187	1.1250	1.0737	1.6647	1.6423	-	-	-
^{235}U	0.0125	0.0069	0.0096	0.0125	0.0114	-	-	-
^{238}U	5.7811	3.2769	4.4864	5.9000	4.9970	-	-	-
U	5.7936	3.2838	4.4960	5.9125	5.0084	-	-	-
Mo	0.2340	0.0123	0.1194	0.4412	0.4338	0.0105	0.0078	0.0079
Na	9.1731	11.208	10.225	8.7013	6.2784	4.1257	6.7544	9.2102
C	0.0257	0.0356	0.0308	1.0686	1.0684	14.043	0.1646	0.0231
O	14.454	8.7577	11.509	12.717	8.0809	-	-	-
Fe	13.363	13.234	13.296	15.906	14.124	11.320	8.4575	8.5898
Cr	2.7593	3.8193	3.3073	3.1571	3.1204	3.2536	2.432	2.4614
Ni	1.3166	1.8224	1.5781	1.5064	1.4889	1.5525	48.072	38.1013
Mn	0.2026	0.2804	0.2428	0.2318	0.2291	0.2389	0.2864	0.2789
Al	-	0.1109	0.0574	-	-	-	-	-
^{10}B	-	-	-	-	-	10.698	-	-
^{11}B	-	-	-	-	-	43.387	-	-
B	-	-	-	-	-	54.085	-	-

[a] 140 Type A drawers and 150 Type B drawers.

The volume of the inner-core region is 406.3 liters, and the outer core region, including the ^{10}B rod drawers, is 638.9 liters, giving a total core volume of 1045.2 liters.

After reaching criticality with Assembly 26, operations were suspended temporarily in order to make a number of modifications to the facility for operation with plutonium fuel. Approximately 2750 kg of nickel were removed from the radial reflector of Assembly 26, to provide nickel for an EBR-II critical experiment to be done on ZPR-3. In order to maintain the present core configuration, the nickel that was removed will be replaced with stainless steel. Some additional drawers containing stainless steel and sodium will be added at the radial boundary to make up for the reactivity lost due to the replacement of nickel with stainless steel and to provide some additional excess reactivity. The new radius to be used for the outer boundary of the nickel-sodium radial reflector is 85.4 cm. The outer radius of the stainless steel-sodium region, designated as the radial shield, will be 97.4 cm.

4. ZPR-3 and ZPPR Operations and Analysis

    a. Support for Routine Operation of the Critical Facilities (P. I. Amundson and R. G. Matlock)

Last Reported: ANL-7655, pp. 13-14 (Dec 1969).

An extensive series of ZPPR shutdown-maintenance projects have been completed preparatory to the Assembly 2 critical experiments.

Successful in-place tests of the air-handling equipment to be used in the sand-gravel roof filter measurements have been performed.

    b. Clean Critical Experiments (P. I. Amundson)

Last Reported: ANL-7655, pp. 15-17 (Dec 1969).

    (i) ZPR-3 Assemblies 58 and 59. The final experiments with Assembly 58 have been analyzed, and those with Assembly 59 have been completed. The unloading of the latter has commenced.

The radial perturbation traverses in Assembly 58 with a Pu-239 annulus and a U-238 cylinder have been analyzed. The results were corrected for the reactivity of the traverse rod and of the steel in the Pu-239 annulus, using the values from traverses with an empty carrier and a steel sample. These corrected results are shown in Table I.A.9. Uranium blocks with a 0.625-in.-dia hole were used in the radial reflector.

TABLE I.A.9. Radial Perturbation Traverses
for ZPR-3 Assembly 58

	Sample Worths (Ih)	
Matrix Position	Pu-239 Annulus, 0.010 in. thick	U-238 Cylinder, 0.2 in. diameter
P 19	2.797 ± 0.019	-0.452 ± 0.044
P 18	3.509 ± 0.017	-0.967 ± 0.019
P 17	4.020 ± 0.016	-1.270 ± 0.014
P 16	4.216 ± 0.012	-1.384 ± 0.013
P 15/16	4.130 ± 0.015	-1.373 ± 0.019
P 15	3.981 ± 0.015	-1.304 ± 0.015
P 14/15	3.747 ± 0.019	-1.156 ± 0.020
P 14	3.482 ± 0.019	-0.959 ± 0.017
P 13/14	3.115 ± 0.020	-0.733 ± 0.017
P 13	2.758 ± 0.015	-0.489 ± 0.017
P 12/13	2.403 ± 0.014	-0.195 ± 0.014
P 12	2.111 ± 0.016	+0.129 ± 0.017
P 11/12	1.715 ± 0.016	+0.342 ± 0.015
P 11	1.244 ± 0.015	+0.348 ± 0.016
P 10	0.463 ± 0.009	+0.090 ± 0.021
P 9	0.171 ± 0.010	+0.040 ± 0.010

Note: (a) Errors from spread of inhour determinations only,
not including uncertainty in autorod calibration.
(b) Sample details are given in Table I.A.10.

TABLE I.A.10. Central Perturbation Worths for ZPR-3 Assembly 58

Sample	Ih	Mass (g)	Ih/kg
Pu-239 annulus, 0.010 in.	4.204 ± 0.008	4.801	875.7 ± 1.7
Pu-239 annulus, 0.007 in.	2.380 ± 0.008	2.761	862.0 ± 2.9
U-235 annulus, 0.010 in.	4.037 ± 0.011	7.128	566.4 ± 1.6
U-235 annulus, 0.005 in.	2.009 ± 0.004	3.638	552.4 ± 1.1
U-235 annulus, 0.003 in.	1.289 ± 0.008	2.327	554.0 ± 3.4
U-238 cylinder, 0.42 in. diameter	-4.703 ± 0.009	85.76	-54.8 ± 0.1
U-238 cylinder, 0.2 in. diameter	-1.413 ± 0.011	19.63	-72.0 ± 0.5
U-238 cylinder 0.1 in. diameter	-0.433 ± 0.010	4.908	-88.3 ± 2.0
B-10 cylinder, 0.06 in. diameter	-3.923 ± 0.011	0.0988	-39710 ± 110

Notes:
a) Errors only from spread of inhour determinations. Not included are errors in
sample masses and determination of autorod worth.
b) Compositions of samples
Pu-239: 98.78 wt % Pu; 95.05 wt % Pu-239; 4.50 wt % Pu-240; 0.45 wt % Pu-241
U-235: 0.010-in. annulus; 93.20 wt % U-235; others 93.10 wt % U-235
U-238: 0.21 wt % U-235
B-10: 92.8 wt % boron; 92.1 wt % B-10 in boron
c) All samples are 2 in. long. The annuli have OD's a little smaller than 0.40 in.

Central perturbation measurements were made with nine samples in the same environment. The manual oscillator which allows the sample and dummy to be changed in the control room without shutting down the reactor was utilized. After the worth of the empty rod had been determined, the various samples were compared with holders and dummies where applicable. Trials showed that the experimental results were most reliable with a quick change (~2 sec) between sample and dummy positions, and then a 100-sec wait before starting the 100-sec averaging of the auto-rod position. These results of the sample reactivities are given in Table I.A.10. The usual small increase of Ih/kg with mass for the Pu-239 and U-235 annuli and a large decrease in Ih/kg with mass for the depleted uranium cylinders can be seen. Agreement is found for the central results of the two samples used in the radial traverses which is encouraging but expected as the same environment was used for both experiments.

In Assembly 59, the autorod in position 0-22 consisted of the polyethylene wedge with a 1/4-in. column of boral on the core side. Its total worth was found by inverse kinetics to be 19.41 Ih. The differential worth was determined as before. A quadratic fit was appropriate. Central fission ratios were measured using the thin-walled spherical counters in the standard manner. The results are given in Table I.A.11, where it will be noted that the errors have been increased to include the extra uncertainty introduced by the U-235 fissions in the U-234, U-236, and U-238 foils. The special drawer loading to accommodate a counter is seen in Fig. I.A.5.

TABLE I.A.11. Central Fission Ratios for ZPR-3 Assembly 59

	Ratio to U-235	Error (%)		Ratio to U-235	Error (%)
U-233	1.466	1.0	U-238	0.0325	1.8
U-234	0.183	2.0	Pu-239	0.942	1.0
U-236	0.068	1.7	Pu-240	0.207	1.0

Note: Error arises mostly from uncertainty in thermal calibration of foils. (Assumed error was ~1% for all foils except U-238, for which the error was ~1.5%.) The errors in some of the fission ratios are higher to allow for the significant fraction of fission in the U-235 in the foils.

Fig. I.A.5

Core Drawer for Back-to-back Fission Counter in Half 1 of ZPR-3 Assembly 59

Axial and radial traverses of Pu-239 and U-238 fission rates were made in Assembly 59. The front 2 in. of the core drawers were rearranged for the radial traverse as in Assembly 58. The core drawer in position P-16 in both halves were arranged as in Fig. I.A.6 for the axial traverses. In both instances special lead blocks with a suitable 0.625-in.-dia hole were used. The results of the four traverses are shown in Tables I.A.12 and I.A.13. The Pu-239 reaction rate at P 20/21, the radial core-reflector interface, is significantly higher than at the symmetric position P 11/12. The trend continued into the reflector and was shown to be caused by the autorod at position 0-22. In the reflector the reaction rate was a function of the autorod position. As in Assembly 58, the fine structure is seen between the results at the core-drawer centers and drawer interfaces. As expected, no such fine structure is seen in the axial traverses.
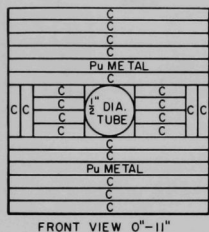

FRONT VIEW 0"-11"

Fig. I.A.6

Drawer Loading in Half 1 for Axial Traverse in ZPR-3 Assembly 59

TABLE I.A.12. Axial Fission-rate Distributions for ZPR-3 Assembly 59

Distance from Centerline (in.)	Pu-239		U-238		Distance from Centerline (in.)	Pu-239		U-238	
	Rel Count	Error (%)	Rel Count	Error (%)		Rel Count	Error (%)	Rel Count	Error (%)
-10.06	0.6332	0.6	0.4119	0.7	+6.00	0.8598	0.5	0.8197	0.5
-9.06	0.6695	0.6	0.5502	0.6	+7.00	0.8127	0.5	0.7598	0.5
-8.06	0.7257	0.6	0.6519	0.6	+8.00	0.7452	0.5	0.6797	0.5
-7.06	0.7871	0.5	0.7364	0.5	+9.00	0.6804	0.6	0.5789	0.6
-6.06	0.8443	0.5	0.7987	0.5	+10.00	0.6517	0.6	0.4421	0.7
-5.06	0.8916	0.5	0.8734	0.5	+11.00	0.6272	0.6	0.3124	0.8
-4.06	0.9379	0.5	0.9111	0.5	+12.00	0.5820	0.6	0.2272	0.9
-3.06	0.9666	0.5	0.9570	0.5	+13.00	0.5333	0.6	0.1691	0.7
-2.06	0.9813	0.5	0.9781	0.5	+14.00	0.4883	0.6	0.1271	0.8
-1.03	0.9990	0.5	0.9837	0.5	+15.00	0.4431	0.7	0.1008	0.9
0	1.0000	-	1.0000	-	+16.00	0.4004	0.7	0.0755	0.8
+1.00	1.0000	0.5	0.9954	0.5	+17.00	0.3569	0.8	0.0576	0.9
+2.00	0.9962	0.5	0.9773	0.5	+18.00	0.3127	0.8	0.0443	1.0
+3.00	0.9757	0.5	0.9590	0.5	+19.00	0.2678	0.9	0.0334	1.2
+4.00	0.9420	0.5	0.9288	0.5	+20.00	0.2273	0.9	0.0254	1.3
+5.00	0.9104	0.5	0.8799	0.5	+21.00	0.1849	1.0	0.0184	1.5

Note: Centerline is 1.03 in. from the interface in Half 1. Positive numbers are in Half 1.

TABLE I.A.13. Radial Reaction-rate Distributions for ZPR-3 Assembly 59

Position	Pu-239 Rel Count	Error (%)	U-238 Rel Count	Error (%)	Position	Pu-239 Rel Count	Error (%)	U-238 Rel Count	Error (%)
P 20/21	0.6431	0.5	-	-	P 14	0.9046	0.4	0.8764	0.5
P 20	0.6432	0.5	0.5292	0.6	P 13/14	0.8680	0.5	0.7940	0.5
P 19/20	0.7309	0.5	0.6119	0.6	P 13	0.7806	0.5	0.7290	0.5
P 19	0.7728	0.5	0.7245	0.5	P 12/13	0.7319	0.5	0.6175	0.5
P 18/19	0.8568	0.5	0.7856	0.5	P 12	0.6474	0.5	0.5344	0.6
P 18	0.8885	0.4	0.8760	0.5	P 11/12	0.6113	0.5	0.3818	0.7
P 17/18	0.9592	0.4	0.9003	0.4	P 11	0.5769	0.5	0.2633	0.8
P 17	0.9733	0.4	0.9651	0.4	P 10	0.4736	0.6	0.1359	1.1
P 16/17	1.0096	0.4	0.9690	0.4	P 9	0.3799	0.7	0.0739	1.1
P 16	1.0000	-	1.0000	-	P 8	0.2908	0.8	0.0421	1.2
P 15/16	1.0199	0.4	0.9657	0.4	P 7	0.2069	0.9	0.0229	1.4
P 15	0.9786	0.4	0.9733	0.4	P 6	0.1266	1.2	0.0125	1.6
P 14/15	0.9620	0.4	0.9095	0.4					

Other measurements for which the analysis still has to be completed are:

(a) radial and axial perturbation traverses with a Pu-239 annulus, and with a Cf-252 source at two power levels;

(b) central perturbation measurements with several samples in two environments;

(c) central substitution reactivity measurements;

(d) Doppler coefficient for a large, natural UO_2 sample;

(e) noise analysis for β_{eff}.

(ii) ZPPR Assembly 2. The predicted critical configuration for ZPPR Assembly 2 is a 2600-liter core with a mass of 1250 kg total plutonium. Due to material-inventory restrictions, a sodium-steel axial reflector could not be built in both halves, but the chosen configuration, with a sodium-steel axial reflector in the fixed half, will allow traverses to be made through this region. The core half-height is 18 in., with a resulting ratio of length to diameter of 0.48. The central zone, which represents one-half of the total core volume, consists of a single drawer cell, as shown in Fig. I.A.7. The two-drawer cell used in the outer zone, as well as the axial and radial blanket configurations, are also shown in Fig. I.A.7. The radial reflector and the axial reflector on Half 2 will be composed of 2 x 2-in. mild steel block of various lengths. Significant predicted reactor parameters are summarized in Table I.A.14.
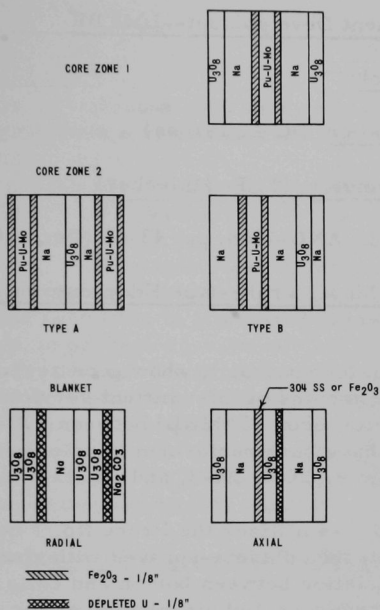
Fig. I.A.7

ZPPR Assembly 2 Drawer Configuration

TABLE I.A.14. Predicted Core Parameters for ZPPR Assembly 2

		Zone 1	Zone 2
I.	**Critical Size**		
	Volume	2600 ℓ	
	Mass of Plutonium	1250 kg	
II.	**Configuration**		
	Height	18 in.	
	Radii--Zone 1	26.5 in.	
	Zone 2	37.5 in.	
	Blanket	52.5 in.	
	L/D Ratio	0.48	
	Zone-1 vol/Zone-2 vol	1.0	
III.	**Zone Compositions**	Zone 1	Zone 2
	Vol %		
	Fuel (Oxide Equivalent)	31.6	32.1
	Sodium	40.1	40.1
	Steel	17.7	20.7
	Void	10.6	7.1
IV.	**Physics Parameters**		
	β_{eff}	0.003172	
	ℓ_p	4.95×10^{-7}	
	Ih/% Δk	1026.8	
	Enrichment Ratio, Zone 2/Zone 1	1.47	
	U/Pu		
	Zone 1	5.7/1	
	Zone 2	3.5/1	

B. Component Development--LMFBR

1. Instrumentation and Control

    a. FFTF Instrumentation (R. A. Jaross)

        (i) In-Core Flowmeter (T. P. Mulcahey)

        Last Reported: ANL-7655, pp. 43-45 (Dec 1969).

        (a) Tests of Model Probe-type Eddy-current Flowsensors (J. Brewer)

Probe No. 9 continues to show good reproducibility and stability after approximately 2 months of intermittent service in the Components and Materials Evaluation Loop (CAMEL) between 700-1200°F. Stability and sensitivity tests have been performed in an oven with several new probes: Nos. 7-4, X-9, 2X-9, 2X-3, 3X-3, and 2X-4.

Probe No. 7-4 utilizes the Probe No. 7 bobbin, but has been grit-blasted with #60 grit, then plasma-sprayed with alumina 4-8 mils thick to provide electrical insulation between bobbin and coils. The three coils were wet-wound with ceramic-coated nickel-clad silver wire and "ceramabond" cement. This probe exhibited a sensitivity of 0.81 mV rms/ft-sec in the oscillating rig with a drive current of 600 mA rms and 500 Hz. With the same current in the oven, it exhibited less than 0.01-mV deviation of unbalance signal from 700 to 1300°F.

Probes X-9 and 2X-9 utilize an Inconel-625 bobbin. Oven tests have shown no magnetic effects from 80 to 1100°F. The bobbin is being wound with ceramic-coated nickel-clad silver wire for tests at higher temperature. Inconel-625 is much harder to machine than Inconel-600.

Probe 2X-3 utilizes the X-3 bobbin (Inconel-600) that has been heated to 1800°F, then water-quenched. This treatment caused the magnetic effects to be much more prominent. The coils were removed, the bobbin was pickled to remove a thin oxide layer, the coils were rewound, and then the unit was designated as Probe 3X-3. The oven test up to 700°F showed no magnetic effects, but one secondary coil was shorted to the bobbin and balance was erratic, so this probe had to be rewound. This probe has been wet-wound with AWG-26 heavy Formvar copper wire and "ceramabond" cement in preparation for further tests.

Probe 2X-4 utilizes the X-4 bobbin (Inconel-600), and has been wet-wound with AWG-24 heavy Formvar copper wire and "ceramabond" cement. Oven tests are being performed on this probe.

To date, Probe 7-4 has shown the greatest stability in oven tests.

Inconel-600 with special treatment should be investigated further because it is so much easier to machine than Inconel-625.

(b) Preparation of Prototype Probe-type Flowsensors (F. Verber)

The specification for procurement of a Type-A flowsensor from a commercial source for tests in the CAMEL loop was completed, and submitted to interested parties for review and comment. The specification package consists of Technical Specification ANL-HTI-LMFBR-551-G [General Design and Performance Specification for an In-core, Solid Configuration, Permanent Magnet, Probe-type Flowsensor (November 1969)], a prerequisition write-up, list of prospective suppliers, design drawings, functional requirements of flowsensor, environmental condition of flowsensor, FFTF Type-A permanent magnet flowsensor assembly procedure, and quality assurance approval tabulation.

(ii) Gas Disengagement for Failed-fuel Monitoring (E. Sowa)

(a) Tests of Gas Disengagement

Last Reported: ANL-7606, p. 38 (Aug 1969).

Experiments were performed to evaluate the Failed-Element Detection and Location (FEDAL) module. These experiments were conducted with ~100-μCi injections of krypton-85 gas into flowing sodium while the activity levels in the module and surge tank were monitored.

The list of experiments is shown in Table I.B.1. The results of the experiments were mixed. In general, an initial rise in activity was encountered within ~45 sec after injection. Frequently, the activity appeared as a rapid rise to peak followed by a gradual decrease. This indicates that disengaged gas is transferred rapidly in the process. Subsequently, during gas recirculation, the gas is diluted, so the measured activity level is lowered gradually. The gas-circulation rate does not greatly affect the response time. Some decrease in the time required for

TABLE I.B.1. FEDAL Module Experiments Performed in the Failed-Fuel Detection Loop (FFDL)

Expt. No.	Sodium Temp (°F)	Sodium Flowrate (ft/sec)	Gas-circulation Rate (ft³/min)	Expt. No.	Sodium Temp (°F)	Sodium Flowrate (ft/sec)	Gas-circulation Rate (ft³/min)
20	500	2	0.77	24	500	0	4.0
21	500	2	2.0	25	500	2	4.0
22	500	2	4.2	26	800	2	4.0
23	500	2	5.0	27	1100	2	2.0-0

detection of the initial peak was observed with faster gas flow, but the decrease was not very significant. More importantly, in the majority of the experiments, the initial peak did not show quantitative recovery of the injected gas. Frequently, after the initial peak was recorded and the activity diluted to its equilibrium level, a further activity rise would occur after the sodium flow was stopped. Subsequently, restart of the sodium pump produced a second peak, which then resulted in quantitative recovery of the gas.

The implications of these results are that the gas is effectively disengaged by the cascade but is partially trapped in the lower portion of the module. Restart of the sodium pump forces the gas upward by a piston-like compression that serves to inject the active gas into the recirculating gas.

The results of the 500°F tests were confirmed by the test at 800°F. In addition, the activity levels measured at the surge tank were always equal to background. This shows that all the separation took place in the module and that none of the gas is carried downstream with the sodium.

At 1100°F, the experiment was started with the gas-circulation rate set at 2.0 ft^3/min. However, plugging was encountered very quickly, so the flowrate dropped to zero. Because of this, quantitative gas recovery was not possible. After the loop was cooled to room temperature and the gas system was dismantled for examination, it was found that the plug was caused by aerosol deposition of sodium droplets on the upstream glass-wool filter. The nature of the deposition was apparent by its pyrophoricity. The upstream filter is a necessary component because the fine Na_2O powder that is carried with the circulating gas tends to foul the circulation pumps.

Several tentative conclusions can be drawn from these results. The first is that a low rate of gas circulation (in the vicinity of 1.0 ft^3/min) is preferable because it reduces the possibility of plugging, and the response time is not greatly affected. The second conclusion is the need for a better configuration for gas circulation, possibly impingement of gas upon the sodium surface so that entrainment of the active gas is more effective. Finally, a longer and more efficient vapor trap is needed in the return gas line to reduce the carryover or formation of the sodium aerosol.

The loop has been frozen and the gas system has been reconditioned. When operations are resumed, further experiments will be performed at 1100°F.

2. Fuel Handling, Vessels and Internals

    a. Core Component Test Loop (CCTL) (R. A. Jaross)

        Last Reported: ANL-7655, p. 48 (Dec 1969).

        (i) Loop Modifications to Accommodate Second FFTF Subassembly. Installation of the pump bypass piping and 4-in. flowtube has been completed. Mechanical modification of the plugging loop has been completed, but electrical work continues. The inlet and outlet sodium piping for a vacuum-distillation sampler and materials-surveillance facility has been completed. The high-temperature dry test of the gate-valve air-lock assembly has been completed at an ambient isothermal temperature of 575°F.

        ANL calibration of the four fuel-assembly pressure transducers (Taylor) has been successfully concluded, with confirmation of the factory-calibration curves.

        The test of the 1/2-in. Nupro prototype valve has been successfully completed with 500 cycles of operation at 125-150 psig and 1060°F; 200 additional cycles were completed at 1200°F with no failure of the prototype valve. This type of valve will be used in the new, modified sodium-sample and plugging-meter loop.

        Sodium testing is in progress.

        A fire-retardant insulation has been sprayed on the bottom of the sheet-metal decking over the CCTL pit, and high-temperature tempered glass has been installed in the CCTL elevator enclosure.

C. Sodium Technology

1. Sodium Chemistry

    The basic work on sodium chemistry is directed toward the development of a sound scientific foundation for understanding the behavior of common nonmetallic contaminants in sodium, for interpreting and evaluating existing corrosion data, and for predicting potential corrosion problems in sodium systems.

    a. Studies of Carbon Transport in Sodium-Steel Systems
       (K. Natesan, J. Y. N. Wang, and T. F. Kassner)

        Last Reported: ANL-7632, pp. 35-37 (Oct 1969).

        (i) Fe-Cr-Ni Alloys. The information on carbon transport in sodium-steel systems presented in ANL-7632 was based, in part, on

estimates of carbon activity in Fe-Cr-Ni alloys.* Estimation was necessary because experimental data for these alloys are scarce in the temperature range of interest, 500 to 800°C. To increase the reliability of the computed data on carbon transport, measurement of a wide range of carbon activities in Fe-Cr-8 wt % Ni alloys,** with chromium contents ranging from 0 to 22 wt %, has been undertaken. The experiments involve equilibration of the Fe-Cr-Ni alloys with carburized Fe-Ni alloys whose carbon activities are known or are being determined.

A number of 10-mil foils of Fe-8 wt % Ni were carburized at 1000°C by exposure to hydrogen gas bubbled through a mixture of 1 part benzene to 50 parts dipentene. The carburized foils are now being equilibrated with various Fe-Cr-8 wt % Ni foils at temperatures of 600, 655, 725, 800, and 900°C in Vycor capsules under partial vacuum. After equilibrium has been reached, the alloys will be water-quenched and analyzed for carbon. For some of the Fe-Cr-8 wt % Ni alloys, the carbon activities will be obtained from the Fe-Ni alloys having carbon activities in the already established range of 0.4 to 1[†] (with graphite as the standard state). For the experiments with lower carbon activities--the range 0.01 to 0.1 is of interest for the studies of carbon transport in sodium-steel systems--the carbon activities of the Fe-Ni alloys is being determined as follows.

High-purity iron wires, both 65- and 18-mil diameter, are being equilibrated with Fe-Ni alloys of different carbon contents at 700°C in quartz capsules. The total carbon concentrations used in the various capsules were calculated to yield carbon activities in the range from 0.01 to 0.5. After the equilibration, the capsules will be quenched in brine solution. The 65-mil iron wires and the Fe-Ni alloys will be analyzed for carbon by the combustion method, and the results will be used to derive activity-versus-concentration plots for the Fe-Ni alloys. In addition, the combustion analyses of the 65-mil wires, in conjunction with measurements of the internal friction of the 18-mil wires, will be used to calibrate the internal-friction method of determining carbon concentrations.

Experimental evidence pertaining to the calculated equilibrium relationship* between the total carbon content of Type 304 stainless steel and the carbon concentration in sodium is also being obtained. Foils of high-purity iron, Fe-8 wt % Ni, Fe-16 wt % Ni, and Type 304 stainless steel were exposed to flowing sodium at temperatures of 600 and 700°C for one month. The flow rate of sodium in the molybdenum test section was 0.6 gpm; the oxygen in sodium, analyzed by vacuum distillation,

---

*Natesan, K., and Kassner, T. F., Calculations of the Thermodynamic Driving Force for Carbon Transport in Sodium-Steel Systems, ANL-7646 (Dec 1969).

**Supplied by Armco Steel Research Lab., Middletown, Ohio.

[†]Heckler, A. J., and Winchell, P. G., Trans. Met. Soc. AIME 227, 732-736 (1963); Smith, R. P., Trans. Met. Soc. AIME 218, 62-64 (1960).

was 10.5 ppm; and the carbonate carbon in sodium, analyzed by titration, was 2.5 ppm. Sodium for total-carbon analysis was obtained with flow-through samplers. The equilibrated iron and iron-base alloys are being analyzed for carbon by the combustion method.

(ii) Carburization by Cyanide. An experimental program is in progress to evaluate the carburizing potential of various carbon species in sodium relative to that of dissolved carbon. Foils of Fe-8 wt % Ni and Fe-18 wt % Cr-8 wt % Ni in molybdenum capsules were contacted with sodium containing 0, 570, 980, or 1400 ppm CN at 800°C for 10 days. The sodium phases were hydrolyzed under vacuum, and no significant amounts of carbon-bearing off-gas were detected. The hydrolyzed solutions are now being analyzed for cyanide, and the foils for carbon and nitrogen. The results of these analyses will establish the distribution of carbon in the alloys versus carbon (as CN) in the sodium.

b. Characterization of Carbon- and Nitrogen-bearing Compounds in Sodium (F. A. Cafasso and A. K. Fischer)

Last Reported: ANL-7632, pp. 37-38 (Oct 1969).

(i) Nitrogen Compounds. Research is now being undertaken to determine the stabilities, solubilities, and reaction chemistry of compounds that are potential nitriding agents in liquid sodium systems. Interest in nitridation stems from the fact that nitrogen gas is a prime candidate for use as a cover over liquid sodium in LMFBRs. Such a plentiful source of nitrogen may lead to nitridation and consequent embrittlement of reactor components.

Nitridation of stainless steels in sodium, although demonstrated by several investigators, is not well understood. A common contention is that calcium in sodium promotes nitridation by forming calcium nitride, which is the carrier for the nitrogen. The magnesium generated in primary reactor coolant by radioactive decay of ^{24}Na could behave similarly. Accordingly, the initial effort in this program will be to examine the extent to which stainless steel is nitrided in sodium at 650°C in the presence of calcium and of magnesium under a nitrogen atmosphere.

2. Sodium Analytical Development

a. Development of Reference Analytical Methods for Oxygen, Carbon, and Nitrogen (R. Meyer and M. Roche)

Last Reported: ANL-7632, pp. 38-39 (Oct 1969).

The sodium analytical group is developing reference methods of analysis for total oxygen, carbon, and nitrogen in sodium. Reference

methods having sensitivities of the order of 100 ± 10 ppb and incorporating reliable sampling techniques are needed in the LMFBR program to certify the quality of other analytical methods and to establish acceptance standards for reactor-grade sodium. Proton activation of stirred molten sodium is being investigated as a reference method for oxygen for the reasons discussed in ANL-7632. Because proton activation is a promising method for carbon and nitrogen as well, the investigation was broadened to include these elements. Current efforts involve proton activation experiments with sodium fluoride, and the design and construction of a sampling/irradiation cell.

(i) <u>Proton Activation Experiments.</u> Bombardments of sodium fluoride pellets spiked with Al_2O_3, C, or AlN were made in a preliminary feasibility study of the proton-activation approach. The results of these experiments indicated that (1) a 6-mil nickel window was adequate for the irradiation cell; (2) activation of sodium to ^{22}Na and ^{24}Na could be kept to an acceptably low level through elimination of neutron and deuteron contamination of the proton beam; (3) with minimum activation of sodium, the projected sensitivity of the analyses, barring other interferences, would be approximately as shown below:

Element	Reaction	Sensitivity (ppb)
O	$^{18}O(p,n)^{18}F$	50 ± 25
C	$^{13}C(p,n)^{13}N$	20 ± 10
N	$^{14}N(p,\alpha)^{11}C$	2 ± 1

Two potential interfering proton reactions were also investigated. It was determined that ^{13}N, the basis for the carbon assay, was produced from oxygen by the reaction $^{16}O(p,\alpha)^{13}N$. A correction for this interference can be made by using the independent oxygen assay from the $^{18}O(p,n)^{18}F$ reaction. This interference becomes serious, however, when the O/C ratio exceeds ten. The other reaction investigated was $^{11}B(p,n)^{11}C$, which constitutes an interference in the nitrogen analysis. This interference is serious even at equal concentrations of boron and nitrogen. A correction* can be made after bombarding at two proton energies, 5 and 14 MeV, since the cross section increases much more rapidly with energy for the nitrogen reaction than the boron reaction.

(ii) <u>Sampling/Irradiation Cell.</u> The cell shown in Fig. I.C.1 is a nickel flow-through sampler, designed for the dual purpose of sampling and irradiating sodium. After the sample (~20 cm^3) is isolated by closing the needle valves, the cell can be removed from the flowing-sodium system,

---

*Kuin, P. N., <u>Proceedings of the Second Conference on Practical Aspects of Activation Analysis with Charged Particles</u>, Liege, Belgium (EUR 3896 d-f-e), pp. 31-42 (1967).

connected to the cyclotron, and bombarded with protons without contaminating the sodium. The proton beam will enter the cell through the 6-mil nickel window, activating the sodium as it is inductively stirred at 400°C. Following activation, the sodium will be transferred from the cell to a counting system for assay of positron activities. The cell and the necessary peripheral counting equipment are now being fabricated.
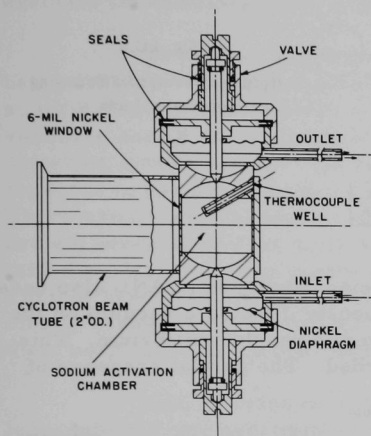

Fig. I.C.1. Sampling and Irradiation Cell for Sodium

3. On-line Monitors

    a. Evaluation and Improvement of the Hydrogen-activity Meter (J. Holmes and D. Vissers)

Last Reported: ANL-7632, pp. 39-40 (Oct 1969).

An objective of this work is to develop a system that detects leaks in LMFBR steam generators by the detection of products of the sodium-water reaction. The detection system now under development is based on monitoring hydrogen in sodium, although electrochemical cells for oxygen in sodium will be considered for future systems. Another objective of this work is to develop an accurate hydrogen-activity meter for monitoring hydrogen impurities in both the primary and secondary sodium systems of LMFBRs, and for use in related research and development programs.

The requirements of a hydrogen meter for detecting water leaks and those for monitoring hydrogen activity differ; the leak detector must be sensitive, rapid, and reliable, whereas the main requirement for the activity monitor is accuracy. Consequently, two distinct units having somewhat different operating principles are now under development.

The in-sodium hydrogen monitor (see Fig. I.C.2) being developed at ANL for leak detection is based on the rate of diffusion of hydrogen through a nickel membrane. A vacuum is drawn at a steady rate by an ion pump, thus causing a hydrogen-activity gradient from the sodium side to the vacuum side of the membrane and resulting in diffusion of hydrogen through the membrane. The partial pressure of hydrogen on the vacuum side, a measure of the hydrogen flux and the hydrogen activity in the sodium, is determined by a mass-spectrometer detector. Possibly the system could be simplified by using the ion pump itself as the detector; the ion current of the pump would be monitored as a measure of the hydrogen flux through the nickel membrane. Calculations indicate that, with a 10-mil membrane, such meters will respond in about 10 sec to a step change in hydrogen concentration in sodium at 500°C.
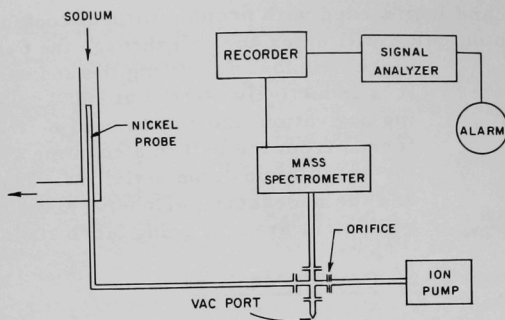
Fig. I.C.2

Hydrogen Monitor for Detecting
Steam-generator Leaks

The hydrogen-activity meter being developed at ANL also uses
a nickel membrane, but rather than continuously drawing a vacuum on the
membrane, the hydrogen pressure is allowed to reach equilibrium. This
equilibrium pressure is continuously recorded. The partial pressure of

hydrogen in equilibrium with so-
dium has been shown to be related
by Sievert's law to the hydrogen
concentration in the sodium.*
The principal components of the
meter (see Fig. I.C.3) are a high-
surface-area nickel membrane
that is immersed in the sodium
and a pressure-sensing device
such as a hot cathode-triode ion
gauge. Auxiliary components in-
clude an ion-pump vacuum sys-
tem for periodic pumpdown and
an apparatus for adding hydrogen
to permit approach to equilib-
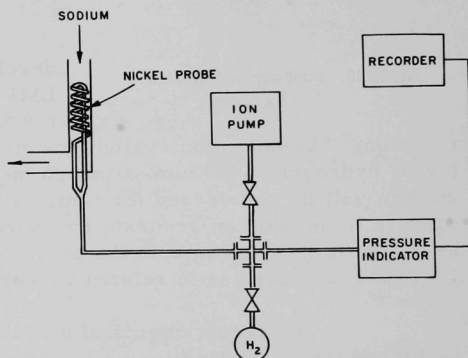rium from above the equilibrium
hydrogen pressure. The time

Fig. I.C.3. Hydrogen-activity Meter

to attain equilibrium varies directly with the hydrogen content of the sodium,
the gas volume of the meter system, and the surface area and thickness of
the membrane; and inversely with the temperature of the membrane and the
diffusion coefficient. For example, with a system containing 1 ppm dissolved
hydrogen in sodium, a gas volume of 100 ml, a membrane temperature,
thickness, and surface area of 500°C, 10 mils, and 100 cm^2, respectively,
it can be calculated that the time to attain 99% of the equilibrium hydrogen
pressure, starting from a high vacuum, is about 5 min.

Current development work on this program is progressing
along three lines: 1) bench-top tests of the hydrogen meter for water-leak

---

*Meacham, S. A., Hill, E. F., and Gordus, A. A., Quarterly Technical Progress Report on AEC-Sponsored
Activities, APDA-228 (1968).

detection, 2) modification of SAL (Sodium Analytical Loop) for evaluation of both types of hydrogen meter, and 3) construction of a test apparatus to evaluate the diffusion properties of nickel membranes.

Two mass spectrometers, a sector and a cycloidal type, are being evaluated for the leak-detector meter by using standard leaks to admit hydrogen to the detection system. Both spectrometers appear to be sensitive enough to indicate a change in hydrogen partial pressure in the detection system of less than 10%, even at hydrogen levels below those expected in normal operations with the membrane immersed in sodium. There are occasional instabilities in the readout, but the overall results are encouraging and the tests are continuing. Two ion pumps have been tested as detector components and appear to have sufficient sensitivity. Further tests are required to determine whether the ion pumps are sufficiently stable and whether their nonspecificity for hydrogen gas will limit their usefulness as the detector component of leak-detector meters.

SAL is being modified to serve as a test apparatus for both the leak-detector and hydrogen-activity meters. SAL will also be used for basic studies on the characterization of oxygen- and hydrogen-bearing species in sodium. The modifications include the installation of a new air-cooled cold trap, two in-line sodium-sample points, and a prototype on-line leak detector with both a mass-spectrometer and an ion-pump detector. A nickel membrane, 9 in. long, of 0.25-in. OD, and 10 mils thick, has been installed. A system has been provided to sample the hydrogen on the gas side of the nickel membrane. SAL is again in operation, and hydrogen-in-sodium monitoring experiments are being planned.

A test apparatus to evaluate diffusion of hydrogen gas through nickel membranes, before and after their insertion into SAL, has been designed and is being constructed. Measurements of the hydrogen flux across the membranes will be made for various hydrogen concentrations in argon.

4. Fission Product Behavior and Control

   a. Low-level Irradiation Loop Tests (N. Chellew and W. E. Miller)

   Last Reported: ANL-7632, pp. 40-41 (Oct 1969).

   Further work on an irradiation experiment to study the behavior of short-lived fission products in sodium has been suspended. This work will be resumed following an evaluation study, now under way, to define the problems of LMFBR plant operation that arise from fuel failure and the consequent deposition of fission products.

b. <u>Development of a Continuous Process for Removal of Radioactive Contaminants</u> (H. M. Feder and C. Postmus)

Last Reported: ANL-7632, p. 41 (Oct 1969).

This investigation seeks methods for the continuous purification of the coolant sodium in a fast-breeder reactor system. The removal of a wide spectrum of contaminants into a discardable waste stream is being sought. One possible method of accomplishment may be a semibatch solvent-extraction system installed in a bypass loop and operated at a temperature of ~150°C. The extracting medium must necessarily have extremely small miscibility with and reactivity toward sodium at 150°C, be appreciably less dense than sodium, boil above 170°C, and be a suitable solvent for the complexes formed during the selective extraction of the impurities to be removed.

A literature search led to the conclusion that suitable solvents might be available among certain classes of organic compounds, such as alkanes, alkylated aromatics, alkyl ethers, amines, phosphines, amides, and nitrides. A program for testing the stabilities of these classes toward sodium at 150°C was instituted. Initial trials, made with dried, commercially available solvents, revealed that none of those selected for test reacted rapidly or in gross fashion; however, superficial signs of reaction--solvent darkening, solvent turbidity, formation of a film on the sodium--were apparent and the cause of ambiguity in the results. Some of the ambiguous reactions were undoubtedly due to impurities in the solvents; reactive functional groups are part of such common organic solvent contaminants as alcohols, ketones, acids, esters, double- and triple-bonded compounds, polycondensed aromatics, and sulfur- and halogen-substituted compounds.

To eliminate such reactive impurities, the following procedure has been adopted. The dried commercial solvent is first pretreated with sodium for 24 hr at 150°C. The solvent is then vacuum distilled, and the middle third of the distillate is retained for the stability tests. Decane, n-octylamine, and tri-n-butylamine were subjected to this procedure and, subsequently, to the stability test of contact with sodium at ~150°C. After 40 hr at temperature, the three solvents show negligible color formation and no turbidity, and the sodium surfaces remain lustrous. These tests are still in progress.

5. <u>Cover-gas Monitoring</u>

a. <u>Nature and Control of Sodium Aerosol Formation</u> (W. E. Miller and R. Kessie)

Last Reported: ANL-7632, pp. 41-42 (Oct 1969).

Sodium aerosol formed by condensation in a vapor space or by turbulence in liquid sodium contacting a vapor space can present serious

problems during reactor operation. The aerosol may clog the gap between moving parts, and transport fission products and other impurities from the liquid-sodium phase to the reactor cover gas. Information on the kinetics and mechanism of aerosol formation and on aerosol control is needed to help eliminate potential problems. The objectives of the present work include 1) collection of data on formation of sodium aerosol, and translation of this data to the design of reactor containers and equipment; 2) assessment of the magnitude of aerosol formation under reactor conditions; 3) evaluation of devices for removal of aerosols.

Formation of sodium aerosol has been observed in qualitative experiments carried out in a glovebox having a high-purity argon atmosphere. About 50 g of sodium were placed in the bottom of a stainless steel vessel measuring 2 in. in ID and 12 in. long. The lower 4 in. of the vessel were heated in a furnace, while the upper 6 in. were externally cooled. Argon from the glovebox was drawn at 0.5 liter/min into and out of the gas space above the sodium via 3/16-in.-OD tubes welded to the upper part of the vessel. The exiting gas stream then passed through an enclosure containing a 47-mm-dia Millipore filter on which the sodium aerosol was collected. The axis of the vessel was inclined 30° to the vertical during the experiments. The top of the vessel was fitted with a Pyrex window through which the sodium surface could be readily seen with the aid of an external light source. The experiments consisted of gradually heating the sodium under the argon cover gas, observing the aerosol formation, and collecting the aerosol particles on the filters.

At 200°C, no aerosol was observed visually or on a filter that had passed 30 liters of cover gas. At 300°C, a light haze was seen, and the filter surface was slightly discolored. At 400°C, the inside wall of the vessel could be made out up to 2 in. beyond the window, and the filter surface was covered with aerosol particles after passage of 1 liter of cover gas. At 500°C, visibility was reduced to 0.5 in. At 600°C, the exit tube plugged before the filter had collected any aerosol. The sodium was next cooled to 300°C, and the sodium surface was again readily visible through the slightly coated window. At the end of these experiments, which lasted only a few hours, it was found that a layer of aerosol 1/8 to 3/16 in. deep had settled on the lower inside wall of the inclined vessel in the cool region.

No problems attributable to sodium aerosol have been encountered in the primary containment vessel of EBR-II, whose sodium pool is at ~375°C. The qualitative results above forewarn that a much greater formation of sodium aerosol can be expected in the primary vessel of an LMFBR, whose sodium pool is at ~500°C.

D. Systems and Plant Development

1. Plant and Design

    a. Contract Management, Technical Review, and Evaluation
(L. W. Fromm and K. A. Hub)

Last Reported: ANL-7632, p. 45 (Oct 1969).

    (i) Evaluation of 1000-MWe Follow-on Study Task Reports.
The first draft of the 1000-MWe LMFBR Follow-on Study Evaluation Report
has been completed. This report is divided into four volumes:

    Volume 1--Summary. General background and objectives;
general scope of study work and expenditures; reviews of design rationale,
brief plant description, and summary of ANL evaluation thereof for each
contractor; summary of parametric and trade-off studies, and ANL evalua-
tion thereof for each contractor; summary of ANL plant-temperature study;
summaries of safety and economics evaluations; summaries of each con-
tractor's proposed R&D programs in each of the nine technical areas of the
LMFBR Program Plan, with ANL comments; and general ANL observations
on results, conclusions and recommendations.

    Volume 2--Plant Design. Detailed descriptions of each
contractor's reference conceptual design, with ANL's critical evaluations
thereof; ANL evaluations of contractors' trade-off and parametric studies
and safety work; capital, fuel-cycle and final energy costs for each con-
tractor's design, with ANL comments; and the ANL plant-temperature study.

    Volume 3--Research and Development. Summarization of
the R&D proposed by each contractor, and ANL evaluation of the programs
proposed; ANL comments on the cost of R&D and the benefits to be derived
therefrom.

    Volume 4--Backup and Contractual Material. Tables of
capital cost estimates for each contractor, and evaluation thereof by
Pioneer Service and Engineering Co.; brief description of the content of
the contractors' reports; and contractual material.

    The draft copies of Vol. 1 were transmitted to RDT for their
review on January 16, 1970. Volumes 2 and 3 were transmitted to RDT upon
completion of the reproduction process. Volume 4 material required further
work and is expected to be completed in February.

E. EBR-II--Research and Development

1. New Subassemblies and Experimental Support (E. Hutter)

a. Experimental Irradiation Subassemblies
(O. Seim and E. Filewicz)

Last Reported: ANL-7655, pp. 54-56 (Dec 1969).

(i) Mark-B61B Subassembly. Hydraulic flowtests of an un-
orificed Mark-B61B subassembly were performed to determine the charac-
teristics of flow versus pressure drop. The tests were made in the stainless
steel pressurized-water loop, and data were collected for reactor Rows 1
through 7. Table I.E.1 gives the data obtained from the tests, converted to
sodium conditions. For comparison, Table I.E.2 shows the reference values
of flow-versus-pressure drop for a standard EBR-II core subassembly.

TABLE I.E.1. Results of Flowtest of Mark-B61B
Irradiation Subassembly

Reactor Row	Effective Pressure Drop (psi)	Sodium Flowrate at 800°F (gpm)
1,2	38	122
3	39	112
4	34.5	88
5	34	77
6,7	40.8	68

TABLE I.E.2. Reference Values of Flow vs Pressure Drop
for an EBR-II Standard Core Subassembly

Reactor Row	Effective Pressure Drop (psi)	Sodium Flowrate at 800°F (gpm)
1,2	38	139
3	39	123
4	34.5	93.5
5	34	78
6	40.8	70

2. Instrumented Subassemblies (E. Hutter and A. Smaardyk)

a. Tests 1 and 2

(i) Operation and Performance of Test 2 (R. Dickman)

Not previously reported.

Outputs from 23 sensors in the Test-2 instrumented sub-assembly have been providing information and records about in-reactor performance of the sensors, the in-reactor environment, and the instrumented subassembly itself.

Except for the temperatures at the centerlines of the fuel pins, the actual measured values during the first reactor run were very close to the projected values. The measured temperatures at the centerlines were lower than projected. One fuel-centerline thermocouple gave an erratic output, and then no output, when about 150 MWd of reactor operation had been completed. In addition, an outlet-coolant thermocouple was inoperative during the first reactor run. Otherwise, all sensors remained functional and consistent throughout 750 MWd of operation.

Representative measurements were:

Fuel-centerline Thermocouples

> In fuel element closest to core center--no output
> In two fuel elements next closest to core center--
> 1250-1320°C
> In fuel element farthest from core center--1160°C

Spacer-wire and Cladding Thermocouples

> Closest to core center and at periphery of capsule
> bundle--418°C
> In center capsule bundle--442°C

Coolant-inlet Thermocouple--365°C

Coolant-outlet Thermocouple--440°C

Thermocouple in Center of Structural-materials Test
Capsule--455°C

Coolant Flow through Subassembly--~28.1 gpm

Fission-gas Pressure at Tops of Four Fuel Capsules--
~24 psia (1.0-mV instrument reading)

These measured values are for a reactor power level of 50 MWt. They are typical of the as-recorded values but have been rounded off.

The first reactor run ended on January 10. The second run began on January 14. The outlet-coolant thermocouple which had been inoperative throughout the first run has recovered and is reading expected temperatures. The fuel-centerline thermocouple that ceased giving an output in the first run is now operating also. Except for slight downward shifts in some fuel-centerline temperatures, the sensor outputs in the second run have been close to those in the first run.

An experimental movable, self-powered neutron-flux monitor is performing as expected.

Preliminary analysis of the initial operation of Test 2 is discussed in Sect. E.6.g of this Progress Report.

3. Coolant Chemistry (D. W. Cissel)

a. Sodium Coolant Quality Monitoring and Control (W. H. Olson, C. C. Miles, T. P. Ramachandran, E. R. Ebersole, and G. O. Haroldsen)

Last Reported: ANL-7655, pp. 59-62 (Dec 1969).

(i) Radionuclides in Sodium. Table I.E.3 lists results of analyses for ^{137}Cs and ^{131}I in primary sodium. The ^{22}Na activity on December 29, 1969 was 3.7×10^{-2} μCi/g.

TABLE I.E.3. ^{137}Cs and ^{131}I in Primary Sodium[a]

Sample Date	Sample Size (g)	Sample Flow (gpm)	Flush Time (min)	Sample Temperature (°F)	^{137}Cs (μCi/g x 10^2)	^{131}I (μCi/g x 10^4)
12/29/69	13.3	0.3	15	390	1.1	0.68
1/5/70	12.9	0.4	15	605	1.1	1.30

[a]All samples taken in Pyrex beaker.

Samples of primary sodium taken in September and November 1969 have been analyzed for tritium. Table I.E.4 shows the tritium history of the primary coolant of EBR-II from 1963 to the present. Within experimental error, the tritium concentration over the past six years has been directly proportional to total accumulated megawatt days of operation.

(ii) Trace Metals in Sodium. Table I.E.5 lists the results of analyses for trace metals in EBR-II sodium. All samples were taken in tritium. Primary sodium was distilled in the laboratory, secondary sodium was distilled in-line. Impurity concentrations were determined by atomic-absorption spectrophotometry.

TABLE I.E.4. Tritium History of Primary Sodium

Sample Date	Tritium (atoms/liter)	Accumulated MWd(t)	Tritium Increase (10^{15} atoms/MWd(t))	Sample Date	Tritium (atoms/liter)	Accumulated MWd(t)	Tritium Increase (10^{15} atoms/MWd(t))
3/7/63	<6 x 10^{11}	0	-	9/18/69	11.4 x 10^{13}	2.9 x 10^4	1.3
7/9/65	1.2 x 10^{13}	2.5 x 10^3	1.5	11/11/69	11.5 x 10^{13}	3.0 x 10^4	1.2
11/14/67	3.8 x 10^{13}	1.5 x 10^4	0.81				

TABLE I.E.5. Trace Metals in Sodium, ppm

Sample Date	Sample Size (g)	Sample Flow (gpm)	Flush Time (min)	Sample Temp (°F)	Ag	Al	Bi	Ca	Co	Cr	Cu	Fe	In	Mg	Mn	Mo	Ni	Pb	Sn
								Primary Sodium											
12/23/69	56	0.6	15	560	~0.04	<0.6	2.1	<0.02	<0.02	0.035	0.07	0.7	~0.03	0.01	0.007	<0.07	0.04	9.3	21.8
								Secondary Sodium											
12/5/69	125	0.4	20	340	0.01	<0.05	<0.02	0.03	<0.02	0.035	<0.005	2.0	<0.02	0.05	0.008	<0.02	<0.02	0.7	<0.08
12/18/69	125	0.8	18	533	0.01	<0.2	<0.04	<0.02	<0.02	0.01	<0.015	0.1	<0.01	0.02	0.003	<0.07	0.01	0.8	<0.2

Recovery of trace metals in the residue from vacuum distillation of sodium was studied further. Microgram quantities of metal powder were mixed thoroughly with 50 g of sodium in a titanium cup and then vacuum distilled. Both the residue and the sodium distillate were analyzed for trace-metal content. The distillation residues were dissolved in acid and analyzed by atomic absorption. The sodium distillate was dissolved and acidified; the metals were separated by oxine extraction or coprecipitation and determined by atomic absorption. Residue recoveries, listed in Table I.E.6, were calculated by dividing the amount of trace metal found in the residue by the sum of the amounts found in the residue and the distillate.

TABLE I.E.6. Recovery of Trace Metals in the Residue from Vacuum Distillation of Sodium

Metal	Total Metal in Residue plus Distillate (ppm)	Metal in Residue (%)	Metal	Total Metal in Residue plus Distillate (ppm)	Metal in Residue (%)
Aluminum	1.10	98	Lead	0.80	90
Bismuth	2.40	100	Magnesium	0.30	100
Calcium	0.20	100	Manganese	0.32	98
Chromium	0.40	100	Molybdenum	0.74	100
Cobalt	0.53	97	Nickel	0.47	97
Copper	0.12	94	Tin	19.5	100
Iron	0.11	100			

(iii) Oxygen in Sodium. Table I.E.7 lists the results of analyses for oxygen in primary sodium by the mercury-amalgamation method. All samples of 15-g size, were taken in stainless steel vessels and extrusion aliquoted for analysis. Concentrations as measured by plugging indicators are listed for comparison.

TABLE I.E.7. Oxygen in Primary Sodium

Sample Date	Sample Flow (gpm)	Flush Time (min)	Sample Temp (°F)	Number of Aliquots[a]	Average Concentration (ppm)	Oxygen Equivalent of Plugging Run (ppm)
10/30/69	0.3	15	320	6	1.4 ± 0.7	<0.5
11/19/69	0.4	15	490	4	1.8 ± 0.2	<0.5

[a]Aliquot size was ~1 g.

Continuing efforts to improve the amalgamation method for oxygen in sodium have revealed two possible clues to the high results that have been obtained. Cooling the mercury to freezing and using glassware exposed to the glovebox atmosphere for long periods have resulted in lower results. Cooling the mercury does not inhibit the desired reaction of sodium and mercury, but may inhibit the reaction of the glass container with the sodium amalgam. Lower results are obtained for those analyses, regardless of cooling, which have been performed in glassware exposed to the glovebox atmosphere for a week or longer. Higher results have been obtained for those analyses performed in glassware immediately after it is cleaned, baked, and placed in the glovebox.

(iv) <u>Carbon in Sodium.</u> Table I.E.8 lists the results of analyses for carbon from 15-g samples taken at sample flows of 0.4 gpm by the oxyacidic flux method.

TABLE I.E.8. Carbon in Sodium

Sample Date	Flush Time (min)	Sample Temp (°F)	Number of Aliquots[a]	Average Concentration (ppm)
		Primary Sodium		
11/19/69	15	490	3	0.6 ± 0.1
12/12/69	15	600	3	1.3 ± 0.1
		Secondary Sodium		
12/5/69	20	340	3	0.4 ± 0.1

[a]Aliquot size was ~1 g.

(v) <u>Hydrogen in Sodium.</u> Table I.E.9 lists the results of analyses for hydrogen in sodium by the isotope dilution method.

TABLE I.E.9. Hydrogen in Sodium

Sample Date	Concentration (ppm)	Sample Date	Concentration (ppm)
Primary Sodium		Secondary Sodium	
10/31/69	1.3	9/22/69	1.3
12/9/69	1.4		

(vi) <u>Hydrogen and Nitrogen in Cover Gas.</u> Table I.E.10 summarizes the concentrations of hydrogen and nitrogen in the primary and secondary argon cover-gas systems. Measurements are made with on-steam gas chromatographs.

TABLE I.E.10. Hydrogen and Nitrogen in Primary and
Secondary Argon Cover-gas Systems, ppm

	Primary			Secondary		
	High	Low	Average	High	Low	Average
			December			
H_2	140	4	10	8	4	4
N_2	3500	2000	2700	700	100	300
			January			
H_2	320	4	10	4	4	4
N_2	4100	2200	3200	500	100	400

(vii) Particulate Matter in Secondary Sodium. In ANL-7655 it
was reported that a portion of the residue from distillation of sodium
samples taken from the secondary storage tank was insoluble in acid. Fol-
lowing return of the secondary system to normal operation, a sample of
sodium was distilled, and no acid-insolubles were found in the residue. The
sample was analyzed for trace-metal impurities, and the results are in-
cluded in Table I.E.5 (secondary-sodium sample of 12/18/69). The values
are typical of those previously reported for secondary sodium.

4. Experimental Irradiation and Testing (R. Neidner)

a. Experimental Irradiations

Last Reported: ANL-7655, pp. 62-63 (Dec 1969).

Table I.E.11 shows the status of the experimental subassem-
blies in EBR-II on January 15, 1970. During the loading changes for
Run 39B, two new experimental subassemblies were installed: XO70, con-
taining fuel capsules from Ge, W, NUMEC, LASL, and BMI; and XO74,
containing mixed-oxide unencapsulated elements of the PNL-8 Series.

One subassembly (XO62) was returned to its former position in
the grid after having been in the reactor storage basket during Run 39A.
Two other subassemblies (XO40A and XO64) were relocated within the grid.

5. Materials-Coolant Compatibility (D. W. Cissel)

a. Evaluation and Surveillance of EBR-II Materials

Last Reported: ANL-7655, pp. 62 and 64 (Dec 1969).

(i) Evaluation of EBR-II Materials Subassembly XA08
(S. Greenberg)

Subassembly XA08 was in the primary tank of EBR-II for
43 months. Its exposure was equivalent to 278 full-power days at 45 MWt
and 136 full-power days at 50 MWt. The average midplane fluence was
8.5×10^2 nvt.

TABLE I.E.11. Status of EBR-II Experimental Irradiations as of January 15, 1970 (Run 39B in Progress)

Subassembly No. and (Position)	Date Charged	Capsule Content and (Number of Capsules)	Experimenter	Accumulated Exposure (MWd)	Estimated Goal Exposure (MWd)	Burnup[a]
XG03 (7D1)	7/16/65	UO_2-20 wt % PuO_2 (2)	GE	25,712	37,000	6.6
XG04 (7B1)	7/16/65	UO_2-20 wt % PuO_2 (2)	GE	26,908	45,000	6.9
XO12A (4B2)	12/12/69	UO_2-20 wt % PuO_2 (19)	NUMEC	802	4,200	$0.4 + 10.3^b = 10.7$
XO18B (4E2)	10/2/69	Structural (3)	GE	1,402	10,000	$0.5 + 5.8^b = 6.3$
		Structural (2)	ANL			$0.5 + 5.8^b = 6.3$
		Structural (1)	ANL			0.5
		Structural (1)	PNL			0.5
XO20 (6B5)	1/13/67	UO_2-PuO_2 (9)	GE	16,871	20,400	6.8
		$(U_{0.8}$-$Pu_{0.2})C$ (3)	UNC			7.4
		Structural (4)	PNL			4.7
		Structural (2)	ANL			4.7
		Graphite (1)	PNL			4.7
XO21B (2D1)	2/23/69	Structural (6)	PNL	17,042	23,200	$3.3 + 4.1^b = 7.4$
		Structural (1)	PNL	8,078	9,000	3.3
XO27 (4B3)	11/21/67	UO_2-25 wt % PuO_2 (18)	GE	14,194	17,600	7.8
		Structural (1)	PNL			5.6
XO34A (2F1)	9/30/69	Structural (4)	ORNL	1,402	7,500	$0.6 + 4.8^b = 5.4$
		Structural (3)	ORNL			0.6
XO35 (7B3)	4/13/68	Structural (7)	ORNL	13,986	44,800	3.2
XO36 (7E1)	7/25/68	UO_2-25 wt % PuO_2 (19)	GE	11,592	43,300	3.1
XO38 (7C5)	5/7/68	Structural (7)	INC	13,568	17,700	2.9
XO40A[c] (5B4)	9/30/69	UO_2-20 wt % PuO_2 (18)	ANL	1,402	4,800	$0.7 + 3.5^b = 4.2$
		UO_2-25 wt % PuO_2 (16)	GE			$0.7 + 3.4^b = 4.1$
XO41 (7A3)	7/24/68	Structural (7)	PNL	12,028	16,700	2.6
XO43 (4D2)	2/20/69	UO_2-25 wt % PuO_2 (37)	GE	7,308	11,000	4.0
XO50 (4C2)	2/23/69	UO_2-20 wt % PuO_2 (4)	GE	7,308	9,200	$3.8 + 7.6^b = 11.4$
		UO_2-28 wt % PuO_2 (4)	GE			3.8
		UO_2-20 wt % PuO_2 (5)	ORNL			3.8
		$(U_{0.82}$-$Pu_{0.18})C$ (2)	W			3.8
		Structural (4)	GE			$2.8 + 5.3^b = 8.1$
XO51 (3A2)	12/16/68	UO_2-25 wt % PuO_2 (37)	PNL	7,853	16,400	1.6
XO54 (4E1)	3/31/69	UO_2-25 wt % PuO_2 (37)	PNL	6,708	10,000	3.5
XO55 (6A4)	2/23/69	$(U_{0.85}$-$Pu_{0.15})C$ (19)	UNC	8,078	20,000	2.5
XO56 (5C2)	4/2/69	UO_2-25 wt % PuO_2 (37)	GE	6,708	10,600	3.3
XO57 (2B1)	2/23/69	Structural (7)	PNL	8,078	15,000	3.3
XO58 (6F1)	4/24/69	UO_2-25 wt % PuO_2 (37)	GE	6,132	16,000	2.2
XO59 (4A1)	4/23/69	UO_2-25 wt % PuO_2 (37)	PNL	6,132	17,500	2.1
XO61 (7A5)	4/23/69	Structural (7)	INC	6,902	18,000	1.5
XO62 (6F3)	5/23/69	UO_2-25 wt % PuO_2 (37)	GE	4,229	13,400	1.8

TABLE I.E.11 (Contd.)

Subassembly No. and (Position)	Date Charged	Capsule Content and (Number of Capsules)		Experimenter	Accumulated Exposure (MWd)	Estimated Goal Exposure (MWd)	Burnup[a]
X063 (7F5)	6/29/69	Magnetic Materials	(7)	ANL	4,568	5,400	1.0
X064 (4F2)	5/28/69	UO_2-25 wt % PuO_2	(19)	GE	5,000	10,700	2.8
X069 (4F1)	10/1/69	UO_2-25 wt % PuO_2	(37)	PNL	1,402	20,700	0.5
X070 (3E1)	1/10/70	UO_2-20 wt % PuO_2	(8)	NUMEC	31	6,000	0.0 + 6.5[b] = 6.5
		UO_2-20 wt % PuO_2	(7)	GE			0.0 + 5.1[b] = 5.1
		$(U_{0.8}-Pu_{0.2})C$	(1)	LASL			0.0 + 1.4[b] = 1.4
		$(U_{0.8}-Pu_{0.2})C$	(1)	LASL			0.0
		$(U_{0.8}-Pu_{0.2})C$	(1)	W			0.0
		$(U_{0.8}-Pu_{0.2})N$	(1)	BMI			0.0
X072 (6E2)	12/12/69	UO_2-20 wt % PuO_2	(18)	ANL	802	9,200	0.3
		Structural	(1)	ANL			0.2
X073 (6C3)	12/12/69	UO_2-25 wt % PuO_2	(37)	PNL	802	29,600	0.2
X074 (5A2)	1/10/70	UO_2-25 wt % PuO_2	(37)	PNL	31	14,500	0.0
XX01[d] (5F3)	11/19/69	UO_2	(16)	ANL	802	2,700	0.3
		Structural	(2)	ANL			0.3

[a]Estimated accumulated center burnup on peak rod, based on unperturbed flux and without depletion corrections (fuels, at. %; nonfuels, nvt x 10^{-22}).
[b]Previous exposure from another subassembly.
[c]The regular position for XO40A is 5B2; the subassembly was relocated to position 5B4 for Run 39B.
[d]ANL Test-2 Instrumented Subassembly.

A section of the hexagonal can enclosing the subassembly was examined optically and with the electron microprobe. Optical microscopy showed a sensitized structure, but no evidence of accelerated, localized, or other unexpected forms of corrosion. The electron-microprobe examination showed no selective dissolution of major alloying elements (iron, chromium, nickel, and manganese) from the surface. The small observed increase (~1/2%) in chromium concentration in grain boundaries--both interior and close to the surface--is consistent with the observed sensitized structure. The sample is being examined for evidence of carbon transfer at the surface.

The estimated temperature of exposure of the sample is being determined; the metallurgical structure indicates a minimum temperature of at least 425°C.

(ii) <u>Interaction of Sodium-Tin Solutions with Type 304 Stainless Steel</u> (W. E. Ruther)

In July 1965, a sufficient quantity of bismuth-tin eutectic alloy found its way into the EBR-II primary tank to raise the tin concentration of the primary sodium to 15-20 ppm and the bismuth concentration to ~45 ppm. The action of the reactor purification system (cold trap) reduced the bismuth concentration to <2 ppm, but did not alter the tin concentration (tin solubility at the cold-trap temperature is >1000 ppm).

Irradiation-capsule bodies exposed during the period of high bismuth concentration showed no evidence of penetration of the stainless steel by either tin or bismuth. Both optical metallography and the electron microprobe were used in this examination.

It is apparent that a leak in the fusible-seal trough or some other occurrence which would cause tin to enter the primary sodium coolant could increase the tin concentration in the coolant to much larger values; at present, there is no provision for removing the tin from the coolant. A series of ex-reactor capsule experiments have been performed to provide advance information as to whether such a hypothetical occurrence would result in a destructive interaction of the sodium-tin solution with the stainless steel cladding of the fuel element.

For these experiments, six capsules of Type 304 stainless steel were filled with sodium-tin solutions having different tin concentrations, closed by electron-beam welding, and then exposed to high temperatures (see Table I.E.12). The capsules were protected by enclosure in a quartz vacuum ampule. Weighed Type 304L stainless steel tabs were included in each capsule. No significant weight changes occurred (see Table I.E.12). A loose deposit was noted on the inside of the capsules after dissolution of the sodium in alcohol, but too little of the deposit was available for analysis. Chemical analysis of the alcohol used to dissolve the sodium-tin indicated incomplete recovery of the tin. It is probable that the deposit observed was tin thrown out of solution in the sodium during the slow cooling of the capsule.

TABLE I.E.12. Results of Capsule Experiments with Sodium-Tin Solutions

Capsule No.	Temp (°C)	Days Exposed	Conc of Tin in Test Solution (ppm)	Description of Surface of Exposed Type 304 L SS Sample	Change in Weight of Type 304L SS Sample (mg/cm²)
SN1	650	7	1460	Brown film; wiped off	-0.21
SN2	550	30	1470	Brown film; remained on	+0.07
SN3	550	7	1500	Brown film; remained on	+0.05
SN4	650	30	0	Metallic, cloudy	+0.05
SN5[a]	650	30	1480	Metallic, etched	+0.03
SN6	650	30	1880	Metallic, cloudy	+0.05

[a]Sodium solution was inadvertently exposed to air during fabrication of capsule.

Sections of the exposed capsule walls and the Type 304L stainless steel tabs were examined in the as-polished condition and after being electroetched in 2 wt % oxalic acid. A comparison of the blank (no tin) specimen from Capsule No. SN4 with the others showed no observable effect resulting from the presence of tin. One capsule (No. SN5) in which

the sodium-tin solution had inadvertently been exposed to air briefly during electron-beam welding showed evidence of very slight grain-boundary attack at the surface. This is characteristic of the attack of sodium containing oxygen. A similar capsule whose solution had not been exposed to air showed no grain-boundary attack.

The specimens with the longer exposure are scheduled for examination by the electron microprobe to see if tin was picked up internally.

b. Examination of Materials from EBR-II Surveillance Subassemblies (S. Greenberg)

Last Reported: ANL-7655, pp. 64-65 (Dec 1969).

Electron-microprobe examination of the stainless steel graphite cans from SURV-2 showed no evidence of interaction between the stainless steel and the graphite.

6. Reactor Analysis, Testing and Methods Development

Last Reported: ANL-7655, pp. 66-75 (Dec 1969).

a. Measurements of Subassembly Outlet Temperature (W. R. Wallin)

Additional measurements of subassembly outlet temperatures have been made with melt-wire and silicon carbide temperature sensors located in subassemblies in three different grid positions. In each of the three subassemblies, the silicon carbide sensors were in the upper shield section and the melt wires were in the upper adapter.

Table I.E.13 compares the indicated temperatures with calculated temperatures and those read by outlet thermocouples. The lower value in each range for the melt-wire data is the temperature determined from the wire with the lowest melting temperature that did not melt. The upper value was determined from the wire with the highest melting temperature that did melt. The two temperature values cited for the silicon carbide sensors are those indicated from two sensors located in the same position.

TABLE I.E.13. EBR-II Coolant Temperatures Measured with Melt-wire and Silicon Carbide Sensors

Run	Maximum Nominal Reactor Power (MWt)	Subassembly No.	Grid Position	Calculated Temperature at Top of Fuel ($^\circ$F)	SiC Temperature ($^\circ$F)	Melt-wire Temperature ($^\circ$F)	Thermocouple Temperature ($^\circ$F)
33B-35A	50	A-838S[a]	7F5	885	989-1014	890-926[b]	No T/C
37	50	C-2211S	3E1	842	898-934	845-890	858
38A	62.5	C-2214S	4B1	925	918-1035	890-926[b]	891

[a]Special experiment testing Na-Ni compatibility.
[b]One 926°F melt wire was partially melted.

b. Rod-drop Design for Kinetics Studies (J. K. Long)

The drop rod described in the Progress Report for June 1969 (ANL-7581, pp. 36-38) provides the fast reactivity step which is desired for kinetics studies, but its total worth is less than optimum. The reactor noise which always is present in the signal interferes with the interpretation of results to the extent that the details on a short time scale are obscured. It would be desirable to have a drop rod with about two to four times the worth of the one last described, which had a worth of 6-7 Ih. When this shortcoming became evident, moving of the rod from its location on a corner of the hex (control-rod position No. 1) to a position on a flat (any even-numbered position) to increase its worth was considered. The worth characteristics of the rod at this alternative location were calculated with a two-dimensional perturbation code, PETULA, which takes multigroup fluxes and adjoints from an independent reactor calculation (e.g., CANDID-2D) and determines relative worths of materials along axial traverses at various radii. It is therefore conveniently adaptable to rod design. A code for

determining rod worths from perturbation data and selecting those which conform to a desired pattern was available from the previous study. This package of codes was applied to the evaluation of relocating the drop rod. It was found that the rod worth probably would decrease as the rod was moved closer to the reactor center and that its pattern of worth versus position would almost certainly be distorted. Moving the rod to a flat does not seem to offer the desired improvement.

Rebuilding the rod with absorptive rather than reflective components was investigated next. Tantalum was selected for study as a replacement for the stainless steel segments of the present rod.

The worth of tantalum was calculated from the CANDID and PETULA codes (two-dimensional diffusion-perturbation theory), using cross-section set 23806.* This calculational method was checked against two tantalum control-rod followers whose worths were measured in ZPR-3.** A follower containing 3668 g of tantalum was found to be worth 4.91 Ih/kg, and one containing 1834 g of tantalum (same length, but half the lineal density) was found to be worth 5.45 Ih/kg. If the deviation from linearity is attributed to self-shielding in the tantalum, the worth of a very thin rod would be 6.0 Ih/kg by extrapolation. The worth of that very thin rod was calculated to be 6.65 Ih/kg. This close agreement gives assurance that the worths of these followers can be calculated reasonably well by perturbation theory if allowance is made for a self-shielding correction of the order of 10-20%, depending on the lineal density.

The calculational scheme for selecting drop rods with the proper pattern of worth then was modified so that as many as four sections of rods and five sodium gaps could be inserted between the lower adapter and the upper follower. These rod sections need not all be the same material. Although surveys are not completed, it has been determined that rods worth 16-18 Ih can be constructed from tantalum, and that the first 2 in. and last inch of travel can be made to have negligible worth. The use of nickel as the material for the third section of the rod is being investigated because it is believed there would be an improvement in the shape of the final portions of the reactivity change.

A parallel effort is under way to improve the acceleration characteristics of the rod by using a high-pressure assist at the start of the drop. Further work in the physics design will be directed toward shaping the worth pattern to take the most advantage of the improved velocity patterns which are now being obtained.

---

* Kucera, D. A., and Madell, J. T., in Reactor Physics Division Annual Report, July 1, 1967 to June 30, 1968, p. 209, ANL-7410 (1968).

** Keeney, W. P., and Long, J. K., in Idaho Division Summary Report, July, August, September 1960, p. 52, ANL-6301 (1960).

c. <u>Drop-rod Calibration before and after Reactor Operations in Run 38B</u> (I. A. Engen)

Two sets of zero-power (500 kW thermal) rod-drop experiments were conducted during Run 38B to investigate the effect of power operation (50 MWt) on the rod calibration. One series of zero-power experiments was conducted before the reactor was taken to power, and a second series of experiments was conducted after the reactor had been operated at 50 MWt for several days.

Inverse-kinetics computations were performed to assess the system reactivity during the experiments, and the results of individual tests were averaged--four rod drops in the first series of experiments and three in the second. Averages of power and system reactivity before and after the rod drops are shown in Figs. I.E.1 and I.E.2 for the two series of experiments.
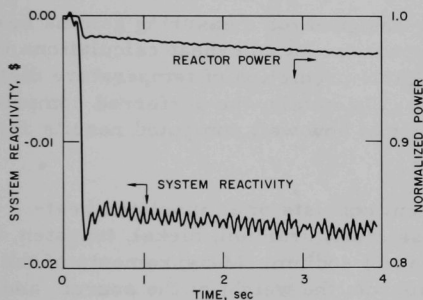
Fig. I.E.1. Results of 500-kW Rod Drops Made before Power Operation in Run 38B
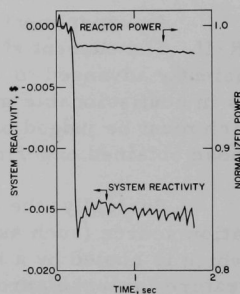
Fig. I.E.2. Results of 500-kW Rod Drops Made after 50-MWt Operation in Run 38B

The experiments show that the change in reactivity after reactor operation at 50 MWt is slightly smaller than the change before power operation. The difference between the results is about $0.0005, or 3.0% of the calibrated rod worth obtained from the second series of experiments.

The temperature coefficient of reactivity and system noise must be considered when examining the results. The noise magnitude is about $0.0015, or three times the difference in two experiments. The temperature coefficient of reactivity is about -1.0 Ih/°F, or -$0.0033/°F. This indicates that a temperature difference of 0.15°F or an error of 50 kW in power can produce a difference of $0.0005 in system reactivity.

The computed reactivity as a function of time shows a recovery of about $0.0015 within 0.2 sec after the drop and then a gradual loss of

reactivity approaching the value of reactivity computed at the time of the rod drop. The recovery of $0.0015 can be associated with cooling of the reactor core; a reduction of 0.45°F in core temperature will produce a reactivity change of +$0.0015. The time constant for fuel and coolant is assumed to be in the range from 0.2 to 0.4 sec, which agrees with the time required for the reactivity recovery noted above. The slight recovery of power following the prompt drop is consistent with this explanation and indicates that temperature effects are not entirely negligible at 500 kW. Conducting the tests at some lower power level is complicated by the low worth of the drop rod and by ion-chamber noise.

The small difference in reactivity found from these experiments performed before and after power operation is not sufficient to disqualify rod calibration at startup, prior to power operation.

d.   Measurements of Gamma Heating in EBR-II (W. R. Wallin)

An experiment is being designed for measuring gamma heating in EBR-II. The current state of the art for gamma-heat calculations is insufficiently advanced to allow reliable prediction of temperature distributions in nonfissionable materials. Ultimately, the preferred computational approach must be judged on the basis of how well computed results agree with those obtained experimentally.

Basically, the experiment consists of an insulated heat-generation source (such as stainless steel, uranium, nickel, tungsten, or B_4C) which is cooled by a known flow of sodium. Measurements of the temperature increase across the source, the weight of the source, and the flow rate of the sodium may be used directly to establish the specific heat-generation rate. The heat-generation source or susceptor will consist of a rod of the material under investigation. The rod will be surrounded radially by a hollow, cylindrical, gas-filled shroud which will eliminate flow of heat in the radial direction (see Fig. I.E.3). Coolant flow around the susceptor will be admitted through a calibrated orifice. A temperature sensor will be immediately above each susceptor, in the exit coolant stream.

The basic irradiation vehicle will be a Mark-B7 irradiation subassembly. Although by no means definitive or final, Fig. I.E.3 illustrates the nature of the modifications of the subassembly that will be necessary. These will include the incorporation of an insulated shroud, special orifice plates, and mounts for the susceptors and temperature sensors. Any one or all of the seven positions in the Mark-B7 subassembly may be used. For experiments in which only one position is used, the remaining positions will be filled with typical blanket or reflector material. Of particular interest is the fact that the vehicle will permit as many as seven independent gamma-heat measurements. This feature should prove particularly valuable in mapping rates of gamma-heat generation in those regions where the gamma-flux profile is changing rapidly.
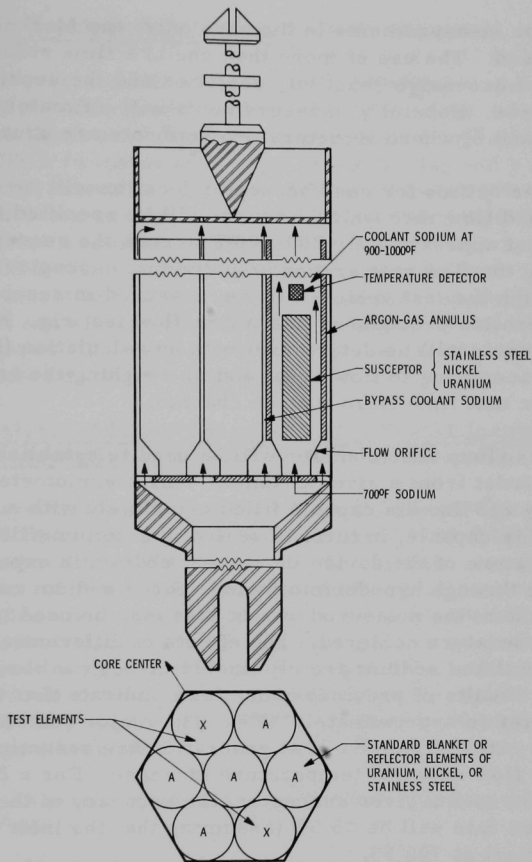
Fig. I.E.3. Arrangement for Suggested Gamma-heating Experiment

The anticipated experimental program will consist of measuring rates of gamma-heat generation in: (1) the blanket with a depleted-uranium-blanket reflector, (2) a nickel or simulated nickel reflector, and (3) a typical experimental subassembly in the core. For measurements in the depleted-uranium-blanket reflector region, two Mark-B7 vehicles will be used. Both will be installed and removed simultaneously. One will be installed in Row 7 and the other in Row 8.

Measurements in a simulated nickel-reflector region will require an as yet unspecified number of prototypal nickel-reflector units assembled in a zone. Four Mark-B7 vehicles with nickel susceptors will be dispersed throughout the zone, with one each in Rows 7 through 10.

For measurements in the core only, one Mark-B7 vehicle at a time will be used. The use of more than one at a time suffers from the disadvantage of excessive reactivity depletion and the sacrificing of needed irradiation space. Hopefully, measurements will ultimately be made in Rows 2, 4, 5, and 6, where structural experiments are usually located.

The orifice for each susceptor location will be sized to yield a predetermined flow rate which, in turn, will be specified to give a temperature rise of approximately 200-300°F across the susceptor. No problem in establishing the flow rate around an individual susceptor is envisioned. The flow through the test vehicle will be measured in accordance with standard calibration procedures in a water-flow test rig. Flow rates in individual channels will be determined both by calculation (from apportioning the total flow according to flow area) and by weighing the amount of effluent discharged per unit time from a given channel.

A sodium thermometer will be used to establish the temperature of the mixed outlet from a given channel. This thermometer consists of a $1\frac{1}{2}$-in.-long by 3/8-in.-dia capsule filled completely with a known weight of sodium. This capsule, in turn, is sealed in a helium-filled outer capsule. As the temperature of the device increases, sodium is expelled from the inner cylinder through hypodermic tubing. Since sodium cannot re-enter the inner cylinder, the measured weight loss may be used to establish the maximum temperature achieved. The effects of differential expansion in the cylinder wall and sodium are eliminated through calibration tests in a furnace. The results of previous bench tests indicate that the accuracy of the thermometer is approximately ±5°F. The major contributors to the uncertainty in rates of gamma-heat generation are assumed to be uncertainties in the flow rate and temperature increase. For a 200°F temperature increase across a given susceptor, the accuracy of the measured heat-generation rate will be ±5.5% (assuming that the inlet temperature remains invariant at 700°F).

e.   <u>Reactivity Monitoring</u> (J. R. Karvinen)

The prototype of the reactivity meter was operated throughout Run 39A. On December 21, an overpower condition caused the reactor to trip. Inspection of the strip-chart record from the reactivity meter suggests that a maximum reactivity insertion of 5.2 Ih was obtained from control-rod motion in approximately 20 sec. Negative feedback effects reduced the excess reactivity to 1.7 Ih. The reactor power level increased to 55 MWt. Also of interest is the response of a thermocouple (FCTC-3) located at the center of an oxide-fuel element in the instrumented subassembly. During the power increase, the thermocouple output indicated an increase of approximately 260°F, going above about 2200°F. Subsequent inoperability of this thermocouple has been attributed to thermal shock.

f.   Post-incident Recall System (J. R. Karvinen)

The post-incident recall system (PIRS) was operating in a loop mode during a reactor trip on December 26. Transient responses were indicated by two thermocouples in the instrumented subassembly. Outlet thermocouple OTC-14 indicated a 1-sec transport lag and a 3-sec system time constant, and inlet thermocouple ITC-14 indicated a 0.4-sec transport lag and a 2.8-sec system time constant. A flowmeter in the subassembly indicated a flow reduction of 5% in less than 200 ms. Spacer-wire thermocouple CTC-3 in the subassembly may have become inoperable during this scram; it indicated a noisy discontinuity approximately 2 sec after the scram and an unaccountably large step decrease after the noise phenomenon ceased. The self-powered (Rh) neutron detector responded almost as expected during the scram.

g.   Analysis of Initial Operation of the Test-2 Instrumented Subassembly to 50 MWt (R. A. Cushman and S. M. Masters)

The initial power operation with the Test-2 instrumented subassembly in EBR-II took place on December 17-18, 1969, when the power was increased from 0 to 50 MWt. (For further operating history, see Sect. I.E.2.a of this Progress Report.) Instrumentation in the subassembly includes fuel-centerline thermocouples in several fuel elements and coolant-channel (spacer-wire) thermocouples in several coolant channels. Calculations with the THTB program had been made to predict the temperature distribution within the fuel element and capsule in the vicinity of the annular-pellet/solid-pellet interface. These calculations were based on the following assumptions:

1.   The gap conductance of the fuel-cladding interface was 1000 Btu/hr-ft^2-°F.

2.   The thermal conductivity of the fuel was given by the equation*

$$k = 0.013 + \frac{1}{[0.4848 - 0.4465(TD)]\,T},$$

where k is in W/cm-°C, TD is the percent of theoretical density of the fuel, and T is in °C.

3.   The solid pellets, which ended at 8.1 in. from the bottom of the fuel column, had a density 96% of theoretical.

4.   The annular pellets, which began at 8.1 in. from the bottom of the fuel column (6.1 in. from the top of the column), had a density of 94% of theoretical.

---

*Asamoto, R. R., Anselin, F. L., and Conti, A. E., The Effect of Density on the Thermal Conductivity of Uranium Dioxide, GEAP-5493 (April 1968).

5. The volumetric heat-generation rate in the annular pellets was 95.8% of that in the solid pellets. Two percent of the reduction in the rate in the annular pellets was due to the lower density, and another 2% was due to the axial flux distribution.

6. The volumetric heat-generation rate in the solid pellets was that at the axial elevation $X/L = 0.55$. At 50 MWt, this corresponded to the linear power rates given below for the various elements containing fuel-centerline thermocouples:

Element No.	Linear Power Rate at 50 MWt, kW/ft ($X/L = 0.55$)
1	9.50
2	9.64
3	9.76
7	9.64
10	9.27
15	9.14
17	8.78

Fifteen radial nodes were used, ten in the fuel region and one each in the gas gap, element cladding, sodium bond, capsule wall, and flowing sodium. Nineteen axial nodes were used, 13 in the 0.592 in. above the annular-pellet/solid-pellet interface (in the annular-pellet region) and 6 in the 0.206 in. of solid-pellet region below the interface. No axial heat transfer was allowed across either axial boundary, although axial heat transfer did occur within the length containing the 19 nodes. Sufficient axial distance was taken on either side of the interface between pellet regions to make axial heat transfer negligible near the thermocouple location at the top of the annular-pellet region.

Results of the calculations are plotted in Fig. I.E.4, which gives expected thermocouple temperature versus linear power for the assumed gap conductance of 1000 Btu/hr-ft^2-°F as well as for gap conductances of 750, 1250, and 1500 Btu/hr-ft^2-°F. Also plotted in Fig. I.E.4 are the readings of the seven fuel-centerline thermocouples, which were taken at nine power-level increments on the approach to 50 MWt. The thermocouple readings were consistently lower than predicted and were also in a consistent pattern from one power level to the next.

The spread of readings at each power level along the abscissa (the linear-power axis) results from the elements being located in a flux gradient. The temperature values at any power level are consistent, with two exceptions. Element 15 consistently records a higher temperature than might be expected. The second exception relates to Elements 2 and 7. These

elements are symmetrically located. Element 7 has a xenon tag, and Element 2 contains helium without xenon. One would expect the thermocouple in Element 2 to read lower than that in Element 7, but the opposite is consistently true.
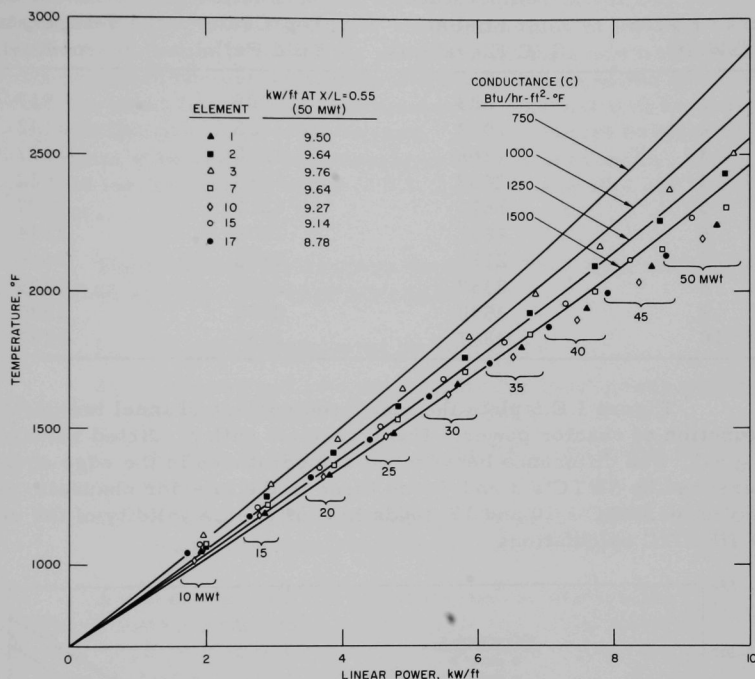

Fig. I.E.4. Calculated and Measured Centerline Temperatures in Fuel Elements of the Test-2 Instrumented Subassembly at Various Reactor Powers

The calculated temperatures in other points in the fuel are considerably higher than the fuel-centerline thermocouples indicated. Table I.E.14 gives the temperatures at three points in the element, at different linear power ratings, as calculated using the assumptions given earlier. The three points considered are the fuel adjacent to the thermocouple, the center of the solid pellet directly under the thermocouple (but approximately 1/2 in. away), and the center of the solid pellet an additional 0.2 in. away. (The last temperature is listed in the table as the maximum temperature of the fuel.) It can be seen that there is about a 500°F difference between the maximum fuel temperature and the thermocouple reading.

TABLE I.E.14. Calculated Temperatures (°F) of Fuel at Various
Locations in Fuel Element in Instrumented Subassembly

Linear Power (kW/ft)	Temperature of Fuel at T/C Elevation	Temperature of Fuel at Top Center Solid Pellet	Maximum Temperature of Fuel
1	883	909	917
2	1072	1125	1142
3	1266	1350	1377
4	1467	1584	1622
5	1676	1827	1879
6	1891	2078	2144
7	2111	2336	2419
8	2337	2603	2705
9	2570	2878	2999
10	2807	3156	3297

Figure I.E.5 plots the measured coolant-channel temperatures
as a function of reactor power. The agreement with predicted values is
quite good. The difference between the temperatures in the edge channels,
as measured by SWTC's 3 and 7, and those in the interior channels, as
measured by SWTC's 10 and 17, tends to confirm the validity of the results
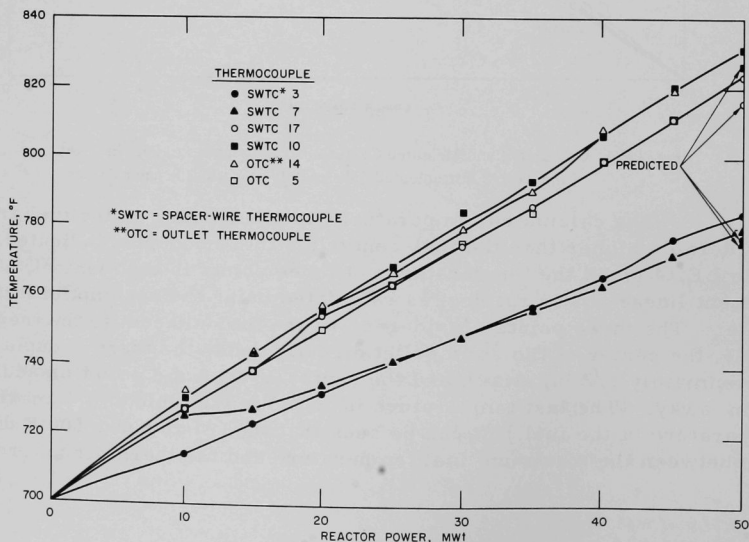of the HECTIC calculations.

Fig. I.E.5. Calculated and Measured Coolant-channel (spacer-wire) Temperatures
in Test-2 Instrumented Subassembly at Various Reactor Powers

h. <u>Digital Data-acquisition System</u> (R. W. Hyndman, M. R. Tuck, K. D. Tucker, E. W. Laird, and R. A. Call)

The input patch panel for the digital data-acquisition system (DAS) has been received from MAC Panel Co. This panel can handle 800 shielded-twisted-pair inputs and 320 digital lines to the DAS. Initial plans have been made for installing the panel. A preliminary wiring list has been prepared for approximately 215 initial inputs to the patch board and from the patch board to the multiplexers. This list will be used to make up detailed drawings of the system. A preliminary breakdown of the DAS inputs with respect to scanning rates has been made. The inputs are grouped for scanning at rates of 0.5, 1.0, 5.0, and 30.0 sec and of 1 and 5 min.

The following preliminary decisions have been made with regard to DAS software and core allocation:

1. All subroutines must be re-entrant.

2. Absolute and computed limits for input points will be stored in two separate tables in the core.

3. A table of offset voltages for DAS inputs will be held in the core.

4. A table of computed values useful to many codes will be maintained in a common area of the core.

A means for effective signal isolation between the DAS and the other EBR-II instrumentation is being sought for initial utilization. One approach is to place resistors of 100 kohms (max) in each leg carrying critical signals to the DAS so that even a complete short circuit of the signal lines at the DAS will not affect other plant instrumentation.

i. <u>Reactivity Effect of Radial Movement of Nickel Reflector in EBR-II</u> (D. Meneghetti and K. E. Phillips)

The reactivity effect of radial movement of a nickel reflector surrounding an EBR-II core has been calculated. The calculation simulates the possible movement of nickel reflector material within the clearance in the subassembly can, which is provided for assembly and for accommodating swelling of fuel during irradiation. The radial movement from inward to outward position were assumed to be 0.158 cm, which is about a 3% movement relative to the thickness of the nickel slug. In the calculation, it was assumed that all the nickel slugs in the subassemblies of the first two rows of reflector moved in unison radially. The third and fourth rows of the nickel reflector and the surrounding additional four rows of depleted-uranium blanket were assumed to remain immobile. Only the effects of the physical displacements were considered, i.e., possible simultaneous variations in dimensions and compositions due to temperature effects were not considered.

The one-dimensional SNARG transport code was used with six-group cross-section set 23806 in cylindrical geometry. Axial leakages were accounted for by use of group-dependent leakage-absorption cross sections corresponding to core composition, homogenized nickel-reflector composition, and depleted-blanket composition.

The reactivity effects calculated in S_2, S_4, and S_6 approximations were: -0.042% $\Delta k/k$, -0.045% $\Delta k/k$, and -0.046% $\Delta k/k$, respectively, for the gross simultaneous movements described above.

j.   Operation of EBR-II at 62.5 MWt in Run 38A   (R. A. Cushman)

During Run 38A, the power level of EBR-II was increased in two increments: first, from 50 to 56 MWt and then, two days later, from 56 to 62.5 MWt. The core loading for the run differed from the usual recent irradiation loadings (Run 29C through Run 37) using the radial depleted-uranium blanket. Except for a portion of Run 32, three structural experiments were in Row 2 in all recent runs. For Run 38A, three sub-assemblies simulating structural experiments were located on Row-3 flats. The four Row-3 corner positions that did not contain safety rods were occupied by half-worth subassemblies. In effect, the seven standard driver subassemblies in Rows 1 and 2 were virtually surrounded by a ring of stainless steel in Row 3. The seven standard driver subassemblies were intentionally located in Rows 1 and 2 as part of a special investigation relating to temperature prediction in EBR-II. Because of their reduced coolant flow rates, all reduced-flow subassemblies (Rows 2 and 3) were removed prior to Run-38 startup. These included both Mark-I and Mark-II fuel subassemblies. Only two structural irradiation experiments were left in the core. These were located in Row 5.
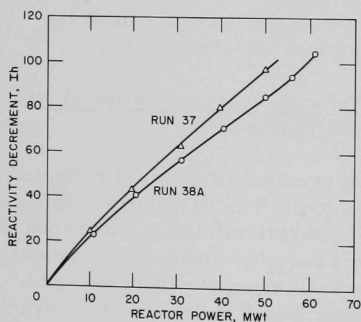

Fig. I.E.6. Curves Comparing Initial Power-Reactivity Decrement in Runs 37 and 38A

The effect of the revised core loading (Run 38A versus Run 37) on the power coefficient was reflected by an overall decrease in the PRD. For example, the PRD at 50 MWt in Run 38A was approximately 10 Ih smaller than that measured at 50 MWt during the Run-37 startup (see Fig. I.E.6). Since the slope of the measured PRD curve for Run 38A was essentially independent of reactor power, it is reasonable to conclude that the decrease in the PRD was not per se a consequence of higher-power operation. Instead, the decrease is believed to be the result of the removal of the controlled-flow subassemblies and a possible

decrease in negative, mechanically originated feedback effects. The slight, but perceptible, increase in the slope of the PRD curve for power levels above 50 MWt has been tentatively associated with the higher fuel-expansion coefficient which resulted from an increase in the fraction of fuel material in the higher-temperature gamma phase above 50 MWt.

Measured control-rod worths during Run 38A were approximately 6-8% smaller than those for previous runs, and a 25% reduction in the worth of the experimental stainless steel drop rod was noted. The reduction in drop-rod worth was the consequence of locating XO21B (a structural experiment) next to the drop rod.

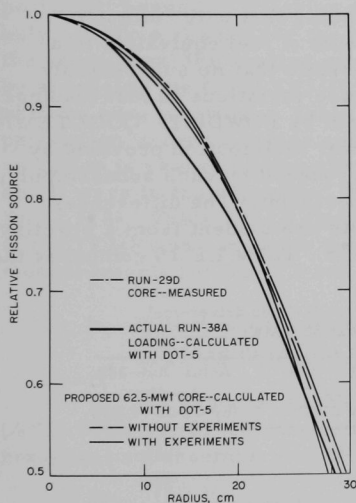The results of physics calculations for the Run-38A configuration clarified the differences noted in control-rod worths relative to previous runs. The increased steel content of Row 3 caused a change in the radial fission-rate distribution for Run 38A as compared with distributions in previous loadings. Such effects are illustrated in Fig. I.E.7.* An additional curve has been added; this gives the results of DOT-5 X-Y calculations for the radial fission distribution for the actual loading for Run 38A. As the figure shows, the calculated radial fission distribution in 38A is different from that measured in Run 29D. The larger maximum-to-average fission-rate ratio in Run 38A is the cause of the measured reduction in control-rod worth relative to previous runs. The reactivity decrease due to burnup of fuel that was measured during Run 38A was about 0.02 Ih/MWd greater than the 0.12 Ih/MWd generally realized since Run 29D. The central peak in fission rate, coupled with the greater worth of central subassemblies, resulted in a larger reactivity-burnup coefficient.

Fig. I.E.7. Relative Radial Distribution of Fission Source in EBR-II

The temperatures indicated by core-outlet thermocouples were found to lie within the allowable range of values predicted from measurements made at 50 MWt. Over the range from 50 to 62.5 MWt, all thermocouple readings increased linearly with respect to power. The readings of outlet thermocouples in Rows 1 and 2 (which contained seven standard driver subassemblies) were used to provide data for relating power, flow, and temperature. The outputs of all seven thermocouples were consistent

---

*The loading diagrams for the two proposed 62.5-MWt cores are presented in a report to be published: Cushman, R. A., et al., Proposal for EBR-II Operation at 62.5 MWt (ANL/EBR-012). Figure 1 of that report shows the loading with no experiments in core, and Fig. 2 shows the loading with experiments in the core.

within an envelope of 11°F. The temperature data suggest that the error in existing power-flow calculations is approximately 2-4% for the cases analyzed. Calculated subassembly-outlet temperatures were up to 10°F higher than measured temperatures. When the influence of adjacent subassemblies is considered, the discrepancy decreases to about 7°F for the cases studied. If the predicted subassembly flows were slightly too high, or if some combination of these possibilities were to occur, approximately a 4% change in the ratio of power density to subassembly flow would effect a reasonable agreement between measured and predicted temperatures.

The calculated DOT X-Y fission distribution for Run 38A was used in two different programs (POWDIST and COOLTEMP) to determine power generation and temperature distributions in the core. The POWDIST program considers the average radial fission-rate distribution and determines the power produced by driver subassemblies located in the various core positions (e.g., 2N1, 4N1, and 4N3) assuming that only "effective" subassemblies (i.e., those containing the amount of fuel equivalent to a driver subassembly) are used. It is quite possible that no subassembly actually produces its designated power, because variations in fuel loadings, burnup, and flux asymmetry are not considered by POWDIST. COOLTEMP, on the other hand, can utilize the detailed power distribution provided by DOT and thus calculates the power actually produced by each subassembly, whether driver, control or safety rod, or experiment. The differences between the POWDIST and COOLTEMP results are evident from a scrutiny of data summarized in Tables I.E.15 and I.E.16. Table I.E.15 compares the

TABLE I.E.15. Predicted Power Distribution (kW per driver-fuel subassembly) for Various Cores at 62.5 MWt

Core Position	Case 1B (Fig. 1 in ANL/EBR-012)	Actual Run-38A Loading (by POWDIST)	Actual Run-38A Loading (by COOLTEMP)
1N1	960	1024	1022
2N1	935	997	996
3N1	886	914	-
3N2	902	940	939
4N1	799	820	813
4N2, 3	835	853	849
5N1	671	694	-
5N2, 4	725	751	753
5N3	744	769	-
6N1	515	532	532
6N2, 5	583	604	604
6N3, 4	618	639	635
Number of "Effective" Subassemblies	76.8	73.8	73.8

TABLE I.E.16. Results of COOLTEMP Calculations for the Actual
Run-38A Loading at 62.5 MWt

Core Position	Subassembly Power (kW)	Temperature at Top of Fuel (°F)	Coolant Temperature at Top of Blanket (°F)	Measured Outlet Temperature (°F)
1A1	1022.4	882.5	882.2	872
2A1	1010.8	880.4	880.5	875
2B1	981.9	875.3	874.1	869
2C1	972.7	873.6	873.2	875
2D1	997.0	878.0	878.1	873
2E1	1007.1	879.8	879.6	880
2F1	1008.3	880.0	879.5	873

power-production predictions for driver subassemblies in various core
positions, assuming a fission distribution which depends on radial position
only. It gives results for the proposed core loading from ANL/EBR-012,
the actual Run-38A loading as calculated by POWDIST, and those obtained
by averaging the COOLTEMP results for driver subassemblies in the
various core positions. Table I.E.16 illustrates the variation in power
production in Row 2, which contained only driver subassemblies. This
variation is caused principally by angular asymmetry in the core (Sectors C
and D were in the depressed flux positions of the core loading; see
Fig. I.E.8). Table I.E.16 also gives the temperatures predicted by
COOLTEMP and compares these with the outlet-thermocouple temperature
measurements for Rows 1 and 2.

k. Effect of Circumferential Temperature Distribution in a
Subassembly Can on Bowing (L. K. Chang)

As reported in the Progress Report for November 1969
(ANL-7640, pp. 61-62), the differential equation of a thermally bowed
hexagonal subassembly can be written as

$$\frac{d^2y}{dz^2} = \frac{C(z,j)\alpha\Delta T(z)}{D},$$

where j is the number of the row where the subassembly is located, and the
other terms are as described in ANL-7640. The value of C depends on
temperature distribution around the circumference of the subassembly can.
Details of this temperature distribution are not available at this time.
However, the approximate temperature distributions as a function of the
azimuthal angle (θ) in r-θ coordinates can be expressed by curves A and B
in Fig. I.E.9. The values of C for temperature functions A and B are 0.72
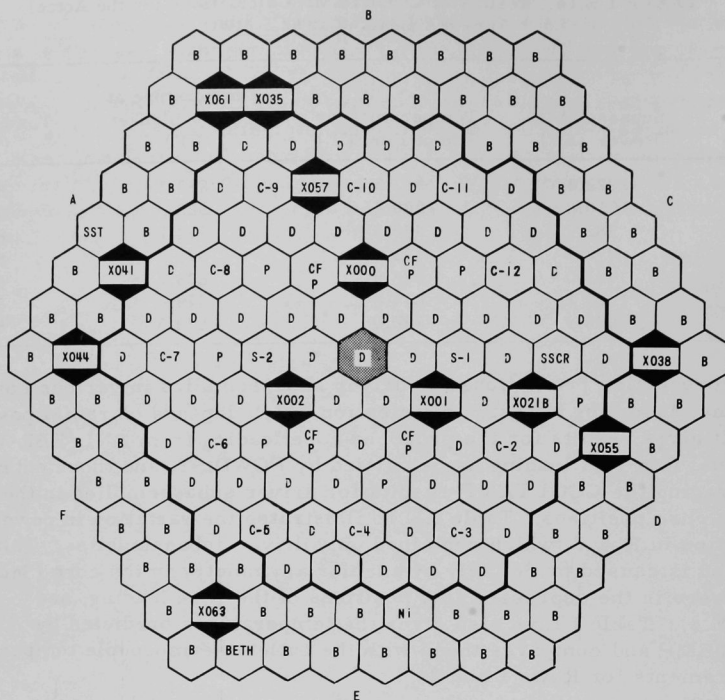and 0.76, respectively.

Fig. I.E.8. Loading Diagram for EBR-II Run 38A. CODE: B--Depleted Uranium; BETH--Beryllium Thimble; C--Control Rod; CF--Controlled-flow Subassembly; D--Driver Fuel; Ni--Nickel-corrosion Subassembly; P--1/2 Driver Fuel - 1/2 Stainless Steel; S--Safety Rod; SSCR--Stainless Steel Control Rod; SST--Stainless Steel Thimble; and X--Experimental Subassembly.
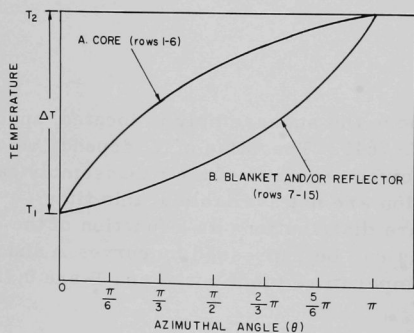

Fig. I.E.9

Asymmetric Temperature Distribution around the Circumference of a Subassembly Can

1. <u>Flow Calibration of Experimental Subassemblies, Using Argon as the Modeling Fluid</u> (A. Gopalakrishnan)

Pressure-drop calculations for air flow through a 91-element EBR-II subassembly have been made to determine the range of inlet pressures and flow rates to be used in some planned flow-modeling tests. Results were obtained by solving the following set of coupled, first-order conservation equations on the IBM/360 computer, using the CSMP code:

Continuity: $\dot{m} = \rho A V = \text{constant}$

Energy: $\dfrac{dT}{dx} + \left(\dfrac{V}{g_c J c_p}\right)\dfrac{dV}{dx} = \dfrac{q}{\dot{m}c_p}$

Momentum: $\left(\dfrac{dp}{dx}\right)_{fric} = \dfrac{-4f\rho V^2}{2g_c D_e}$

$\left(\dfrac{dp}{dx}\right)_{accl} = \dfrac{-\rho V}{g_c}\left(\dfrac{dV}{dx}\right)$

$\left(\dfrac{dp}{dx}\right)_h = -\rho\dfrac{g}{g_c}$

State: $p = \rho R T.$

In these equations, ρ, V, and T are, respectively, the local density, velocity, and temperature of the gas, and q is the linear heat rate along the flow direction x.

Results calculated for air flow with inlet pressure $p_{in} = 100$ psia and with negligible wall heating in the channel are given in Table I.E.17 for five different values of Reynolds number. As expected, the static head losses are negligible. In this particular case, the percentage of the total pressure drop due to acceleration is also small, even though there is appreciable change in the gas velocity across the channel when the flow rate is high.

TABLE I.E.17. Calculated Air Flow through 91-element Subassembly

($p_{in} = 100$ psia)

Reynolds No. $(\times 10^{-4})$	Volume Flow Rate (scfm)	Δp_{fric} (psi)	Δp_{accl} (psi)	Δp_h (psi)	V_{in} (fps)	V_{out} (fps)	T_{out} (°F)
1	158.0	0.90	~0.0	0.02	29.0	29.2	70.0
2	316.0	3.16	0.01	0.02	58.0	59.9	70.0
3	474.0	6.69	0.06	0.02	87.0	93.2	69.9
4	632.0	11.52	0.20	0.02	116.0	131.3	69.7
5	790.0	17.84	0.52	0.02	145.0	177.4	69.1

The initial air-flow tests are planned for a variety of different subassemblies, with inlet air pressures in the range from 20 to 100 psia, using an out-of-pile subassembly-flowtest facility.

m. Development of the MELT-II Code (R. H. Shum and L. B. Miller)

A provisional version of the MELT-II code has been adapted for use with the IBM 360/75 computer. Small differences between the results of a sample problem provided with the code and the results computed on the 360 are being investigated. Input data are being generated to repeat a reactivity-feedback calculation on a wet-critical EBR-II configuration that was studied earlier with the MELT-I code (see Progress Report for Nov 1969, ANL-7640, p. 63). More detailed input is required for the MELT-II calculation, e.g., a program for least-squares fitting is being used to obtain coefficients for polynomial expressions of the heat capacities of fuel and cladding.

n. Safety Evaluation of the 0-3 Group of Mixed-oxide Fast-reactor Fuel Elements for Irradiation in EBR-II at 143% of Full Power and 10 at. % Burnup (L. K. Chang)

The temperature distributions in these fuel elements were calculated with the equations given by Golden,[*] and the pressure and thermal hoop stresses were obtained by assuming that the gas is ideal and that the temperature gradient through the cladding thickness is constant. Two cases are being considered in the present evaluation:

1. Reduction in wall thickness of the cladding caused by fuel-cladding interaction and allowance for a 1.4-mil defect are neglected.

2. The depth of a possible fuel-cladding interaction is assumed to be 4 mils in addition to a 1.4-mil allowance for defect.

In Case 1, the calculated inner and outer cladding temperatures were 761.5 and 714.5°C, respectively. The corresponding hoop stress resulting from internal fission-gas pressure was 8000 psi, and the thermal hoop stress was 13,600 psi. The pressure stress is below the yield strength (about 13,000 psi for Type 316 stainless steel), but the combined thermal and pressure stress is above the yield strength at some point in the cladding. According to Miller,[**] yield and growth will occur only on the first thermal cycle.

---

[*]Golden, G. H., Heat-transfer Equations for LIFE, internal memo (Dec. 26, 1969).
[**]Miller, D. R., Thermal-stress Ratchet Mechanism in Pressure Vessels, Trans. ASME 81, Series D, No. 2 (June 1959).

In Case 2, the inner cladding temperature was 726°C and the temperature difference through the thickness 25°C. The pressure and thermal hoop stresses were 13,800 and 7,200 psi, respectively. The pressure stress exceeds the yield strength of the material (13,500 psi), and repetitive loading could produce cladding failure. Although experimental fatigue data at this temperature are not available, it is believed unlikely that the cladding will fail at less than 2000 cycles.

o. <u>Temperature Distribution in a Mechanically Mixed Oxide Fuel</u>
(R. K. Lo)

The transient-heat-transfer computer code THTB was used to determine the temperature distribution in heterogeneous UO_2-PuO_2 fuel for the case of a power burst following a postulated accidental insertion of an EBR-II driver-fuel subassembly at high speed into a near-critical core. The reactor was assumed to be tripped on a 25-sec period. The fuel rod considered was 0.25 in. in diameter, the cladding was 0.015 in. thick, the PuO_2 particles were 20 μm in size, and the UO_2 particles 500 μm. The contact conductance between PuO_2 and UO_2 particles was taken as 4000 Btu/hr-ft^2-°F, and that between UO_2 particles and the cladding as 1500 Btu/hr-ft^2-°F. The heat-transfer coefficient between flowing sodium and cladding was 1400 Btu/hr-ft^2-°F, and the linear heat generation was 16 kW/ft.

Assuming that the fuel was located in Row 1 and that all uranium was ^{238}U, the relative power density in the plutonium was calculated to be 74.2%, and that in the uranium to be 25.8%. (The volumetric heat generation of PuO_2 particles was 4.695×10^8 Btu/hr-ft^3, and that of UO_2 particles was 1.633×10^8 Btu/hr-ft^3.) Using the power trace shown in Fig. I.E.10 (as computed from the AIROS II-A code) and the physical data outlined above as input to the THTB code, the temperature distribution in the PuO_2 and UO_2 particles was obtained. The calculated volume-weighted average temperatures are shown in Fig. I.E.11. For this case, the volume-weighted temperature of PuO_2 is almost exactly that of the UO_2.
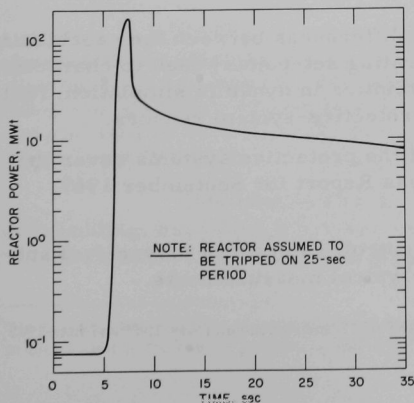

Fig. I.E.10

Power Burst Following a Postulated Insertion of an EBR-II Central Driver-fuel Subassembly at High Speed into a Near-critical Core

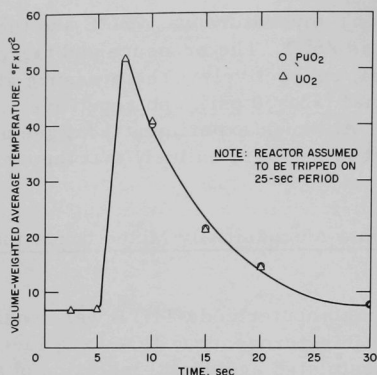NOTE: REACTOR ASSUMED TO BE TRIPPED ON 25-sec PERIOD

Fig. I.E.11

Calculated Transient Average Temperatures for a Power Burst Following a Postulated Insertion of an EBR-II Central Driver-fuel Subassembly at High Speed into a Near-critical Core

p.   EBR-II Reactor Safety Analyses (A. V. Campise)

Dynamic system studies are being made to evaluate the response of the EBR-II protective system to operational abnormalities in the primary system. The studies cover postulated events which may cause the operational set-points for flux, flow, and temperature to be approached or exceeded. The assumptions on which these studies are based are:

1.   The dynamic feedback model is identical with the 8-channel fuel-element model which gave excellent agreement with data from EBR-II rod-drop experiments.

2.   The postulated abnormal conditions of operation are those originally characterized in ANL-5719 and its Addendum.*

3.   The capabilities of the various experimental-irradiation and driver-fuel elements under transient conditions are characterized on the basis of expected thresholds for damage (e.g., uranium-stainless steel eutectic temperature, fuel-melting temperature, and sodium-boiling temperature).

4.   The margins (i.e., the differences between the capabilities under transient conditions and the operating set-points) used to characterize the set-points reflect the known uncertainties in dynamic simulation, fuel-element fabrication, and response of protective-system sensors.

5.   The response times of the protective systems cover the range of values reported in the Progress Report for September 1969, ANL-7618, pp. 44-46.

6.   Reactivity worths of control, safety, and driver-fuel subassemblies are consistent with recent typical measurements.

---

*Koch, L. J., et al., Hazards Summary Report, EBR-II, ANL-5719 and Addendum (May 1957 and June 1962, respectively).

Preliminary results of one of these dynamic studies are presented here.

(i) Safety Rods Driven into a Near-critical Reactor. This hypothetical system malfunction is postulated to occur under conditions of reduced primary-coolant flow.* The event is being studied to determine how the protection for high outlet-coolant temperature would respond. Figure I.E.12 shows the power and reactivity increases following the insertion of the safety rods. The system reactivity already is decreasing at the point of a trip for high coolant temperature, thus demonstrating the inherent stability of the EBR-II core to credible reactivity insertions. Figure I.E.13 shows some of the peak fuel-element centerline temperatures during and following a high-coolant-temperature trip. Peak fuel temperatures do not approach postulated damage thresholds (i.e., metal-fuel temperature equals 1834°F, and oxide-fuel temperature equals 5074°F). The delay-time response for the protective circuits involving a high-coolant-temperature trip were varied within the range of values measured in the recent tests reported in ANL-7618. The set-point was held constant at 940°F for 62.5-MWt operation.
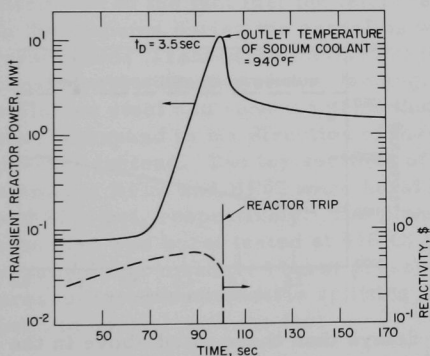

Fig. I.E.12

Increase in Power and Reactivity Following a Postulated Insertion of Safety Rods into a Near-critical EBR-II Core with Reduced Primary-coolant Flow and a 3.5-sec Time Delay (t_D) in the Trip for Outlet Coolant Temperature
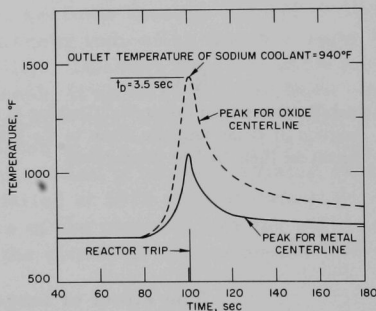

Fig. I.E.13

Peak Fuel Temperatures Following a Postulated Insertion of Safety Rods into a Near-critical EBR-II Core with Reduced Primary-coolant Flow and a 3.5-sec Delay (t_D) in the Trip for the Outlet Coolant Temperature

Depicted in Fig. I.E.14 are the peak temperatures of driver-fuel cladding, assuming a 3.5-sec and a 4.0-sec delay (t_D) in the high-coolant-temperature trip. Also shown is the uranium-stainless steel

*The postulate regarding the occurrence of this event assumes the very unlikely simultaneous malfunction of fuel-handling and reactor-monitoring activities.

eutectic temperature. For a delay response time of 4.0 sec in the high-coolant-temperature trip circuit, the peak cladding temperature never exceeds 1150°F and is 169°F below the uranium-stainless steel eutectic temperature. Figure I.E.15 shows the peak temperature of driver-fuel cladding as a function of the delay response time in the high-coolant-temperature trip circuit. These temperatures remain below the uranium-stainless steel eutectic temperature for the initial range of response times studies.
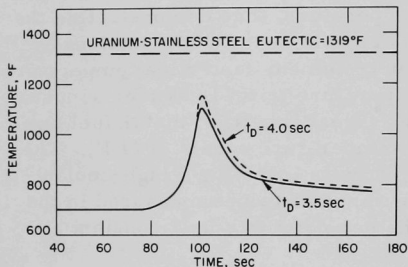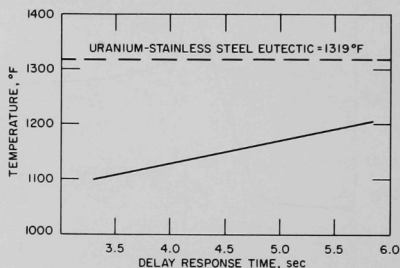

Fig. I.E.14

Peak Temperature of Driver-fuel Cladding Following a Postulated Insertion of Safety Rods into a Near-critical EBR-II Core with Reduced Primary-coolant Flow

Fig. I.E.15

Peak Temperature of Driver-fuel Cladding as a Function of Delay Response Time in the Trip Circuit for High Coolant Temperature

The effect of longer delays than those cited above in the high-coolant-temperature trip are being similarly evaluated.

The above example represents only one within the range of postulated events being analyzed. The primary objective of the studies is to use quantitative dynamic analysis to relate protective-system set-points and response times to current and future experimental-irradiation core loadings. Thus, a quantitative basis ultimately will be developed to identify the interdependence and inter-relationships of protective-system action, transient limits, safety margins, and maximum irradiation performance of core constituents.

7. <u>Driver Fuel Development</u> (C. M. Walter)

    a.   <u>High Burnup Encapsulated Irradiations</u> (W. N. Beck)

        Last Reported: ANL-7655, p. 76 (Dec 1969).

        (i) <u>Postirradiation Examination of Encapsulated Mark-IA Elements BF02 and BF03</u>. Elements BF02 and BF03 were successfully irradiated to a calculated burnup of 3.7 at. % at a maximum cladding temperture of 494°C. The maximum measured increase in diameter of each element was 2.2%, of which 0.9% is calculated to be due to cladding swelling. The fuel had swollen to make intimate contact with the inside of the cladding except in the areas about $1\frac{1}{2}$ in. from each end. In these areas, the fuel was separated from the cladding by a 1.8-mil annulus. The fuel column had elongated, but was an average of 0.17 in. below the restrainer, which is twice the separation observed in specimens irradiated to 2.5 at. % burnup.

        The small, localized splits that were found in the claddings of elements after postirradiation annealing (reported in ANL 7655) have been attributed to the fact that the temperatures--and, therefore, the pressures-- in the plenums during the annealing were higher than they were during irradiation. Transverse metallographic sections through the splits showed considerable thinning of the cladding, thereby indicating that the Type 304L stainless steel had retained some ductility. The fuel does not show a tendency to expand in the direction of the break; it appears to have been compressed instead. The top sections of tubing which were the plenums of elements BF02 and BF03 were burst tested at 410°C; they failed at 8825 and 9175 psi, respectively. The plenum section of an unirradiated Mark-IA tube also was burst tested at 410°C; it failed at 5575 psi. It cannot be assumed that measured burst pressures of the plenums are the same as the pressure which caused the splitting of the cladding. The plenums had not been in contact with the fuel.

        Examination of polished sections of the fuel revealed no unusual structures. Neither microtearing nor interlinking of gas bubbles was discernible at a magnification of 750X. No reaction zones between fuel and cladding were noted.

        The examination is still in progress. A careful study is being made of the conditions and properties of the cladding.

    b.   <u>Fuel and Cladding Surveillance</u> (A. K. Chakraborty and G. C. McClellan)

        Last Reported: ANL-7655, p. 77 (Dec 1969).

        (i) <u>Controlled-flow and 70%-enriched Experiments</u>. Controlled-flow Subassembly E-2188 was removed from the reactor at the end of Run 38,

after reaching a calculated maximum burnup of 1.76 at. %. It contained both Mark-IA and Mark-IB fuel elements. Thirty of the former and 15 of the latter have been examined. Fuel-swelling data for both types of the elements are summarized in Table I.E.18.

TABLE I.E.18. Summary of Fabrication and Irradiation Data for Controlled-flow Driver-fuel Subassembly C-2188S

(Calculated Burnup: 1.76 at. % max; 1.57 at. % avg)

Injection-casting Batch No.	Silicon Content of Fuel (ppm)	Number of Elements	Element Burnup Range (at. %)	Total Volume Swelling of Fuel ($\Delta V/V$, %)	
				Average	Range
Mark IA					
95II	290	3	1.69-1.73	16.09	15.72-16.58
96II	308	4	1.71-1.73	16.33	15.96-16.59
97II	276	7	1.70-1.75	16.12	15.56-16.53
98II	289	16	1.67-1.76	16.58	15.80-18.01
Mark IB					
95II	290	2	1.71-1.72	18.78	17.72-19.87
96II	308	2	1.70-1.73	20.60	19.67-21.53
97II	276	1	1.74	20.72	20.72
98II	289	10	1.67-1.76	19.40	17.47-21.20

The data for the Mark-IA fuel show a saturation in the fuel swelling occurring at the same $\Delta V/V$ at which driver fuel irradiated under 50-MWt conditions exhibits swelling saturation. This saturation is shown in Fig. I.E.16.
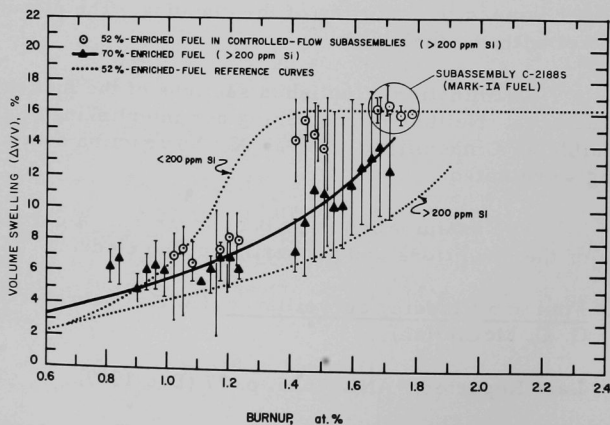

Fig. I.E.16. Volume Swelling of U-5 wt % Fs Fuel in 70%-enriched and Controlled-flow Subassemblies as a Function of Burnup

Mark-IB fuel exhibited a higher fuel swelling than the Mark-IA fuel. This is attributed to the larger plenum in the Mark-IB element. The larger plenum provides more room for the gas. Therefore, plenum pressures are lower at a given burnup, and the pressure restraint on the rather compressible U-5 wt % Fs fuel is less.

Table I.E.19 summarizes the changes in cladding diameter (ΔD) for controlled-flow Subassembly C-2188S and 70%-enriched Subassembly C-2184S. Both went to a maximum burnup of about 1.7 at. %. With the exception of elements 25 and 47 in subassembly C-2184S, all the ΔD values are consistent with the values for stainless steel swelling alone as calculated from the PNL equation.*

TABLE I.E.19. Summary of Postirradiation Measurements of the Cladding Diameters of Elements from Controlled-flow Subassembly C-2188S and 70%-enriched Subassembly C-2184S[a]

Subassembly	Element No.	Calculated Burnup (at. %)	Volume Swelling of Fuel (%)	Max ΔD at 0° Orientation (in.)	Max ΔD at 90° Orientation (in.)	Upper 95% Confidence Limit of Stainless Steel Swelling Band
C-2188S[b]	3	1.76	16.3	0.00000	0.00049	0.00082
	6	1.76	16.1	0.00031	0.00054	0.00082
	11	1.75	16.8	0.00062	0.00066	0.00081
	50	1.72	18.0	0.00069	0.00044	0.00078
C-2184S	17	1.68	12.1	0.00039	0.00049	0.00041
	25	1.66	17.5	0.00056	0.00069	0.00040
	38	1.65	16.0	0.00031	0.00045	0.00040
	10	1.69	15.2	0.00044	0.00041	0.00041
	5	1.71	16.1	0.00044	0.00021	0.00042
	47	1.63	16.7	0.00059	0.00044	0.00040
	20	1.68	13.5	0.00033	0.00039	0.00041
	7	1.69	9.7	-0.00014	-0.00002	0.00041
	13	1.69	9.7	0.00009	0.00032	0.00041
	26	1.66	16.9	0.00015	-0.00006	0.00040
	2	1.71	11.0	-0.00005	-0.00021	0.00042

[a]Nominal cladding OD is 0.174 in.
[b]Three more elements from this subassembly are being surveyed.

(ii)   Instrumented Subassembly (J. R. Honekamp and W. N. Beck)

(a)   Comparison of Fuel Temperatures and Plenum Pressures Predicted by SWELL 2D Code with Measured Values Obtained from the Instrumented Subassembly. The SWELL 2D code for fuel-element lifetime was used to calculate the expected fuel-centerline temperatures and plenum-gas pressures in the instrumented subassembly (XX01) currently being irradiated in EBR-II. Since the SWELL code was not designed to treat fuel elements with a central thermocouple, hand calculations were used to correct the temperatures for this difference in geometry.

The temperatures predicted by SWELL at the thermocouple locations, corrected for the geometry difference, ranged from 200 to 300°C higher than measured.

---

*Claudson, T. T., Pacific Northwest Laboratories, private communication.

The average heat rating of the fuel elements in the instrumented subassembly is in the range from 8 to 9 kW/ft. At this low heat rating, the SWELL 2D code predicts essentially zero gas release during the 17 days of operation that have been logged to date and a plenum-gas pressure of 40 psia at the end of the 17 days. The measured pressures range from 35 to 44 psia. (The pressure corresponding to 100% gas release during the 17 days would be 60 psia.) The agreement between measured and calculated pressure is considered very good.

The temperature data are being evaluated to determine the most probable source of the 200 to 300°C difference. Since the spacer-wire thermocouples which measured the sodium temperature in the sub-assembly are reading close to the values predicted by the HECTIC code, it does not appear that all the difference can be attributed to uncertainty in the power generation. Subsequent calculations have indicated that increasing the conductance of the gap between the fuel and cladding from 700 Btu/hr-ft²-°F, as predicted by the SWELL 2D code, to 1500 Btu/hr-ft²-°F produces good agreement with the measured temperatures. Gap conductances in this range are consistent with some of the observations reported in the literature.*

8. Operation with Failed Fuel

Last Reported: ANL-7640, pp. 73-75 (Nov 1969).

a. Studies of Transient Performance of Driver Fuel

(i) Fuel-motion Transducer (A. A. Madson)

Preliminary tests of the instrument for detecting temperature-induced axial motion of fuel have been concluded. The instrument response and the remote manipulation of the fuel-motion fixture were encouraging.

The fuel elements selected for the test were made from vendor-fabricated fuel which had shortened, or slumped, during irradiation to 0.6 at. % burnup in Subassembly 2178. Each element was prepared for testing by cutting through its cladding about $1\frac{1}{2}$ in. above the fuel and removing the top end restrainer. The bottom spade end was then cut through just above the weld of the spacer wire. Excess sodium above the fuel was removed with a flat-bottom drill bit. The resultant element has no spiral spacer wire and is open, with the fuel exposed, at the top.

---

*Baily, W. E., et al., "Thermal Conductivity of Uranium-Plutonium Oxide Fuels," Nuclear Metallurgy, Vol. 13, International Symposium on Plutonium Fuels Technology (October 1967); Craig, C. N., el al., Heat Transfer Coefficients between Fuel and Cladding in Oxide Fuel Rods, GEAP-5748 (January 1969).
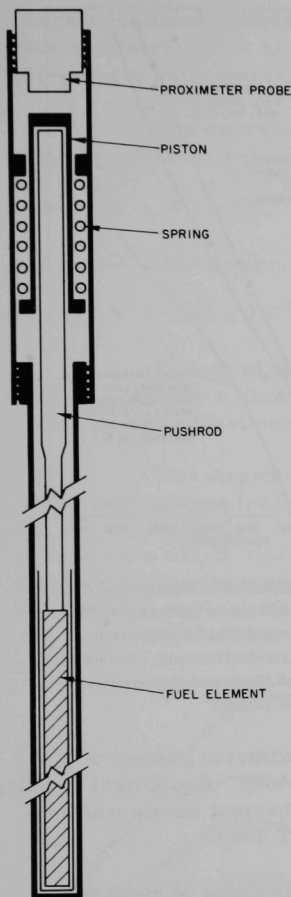
Fig. I.E.17. Fixture Used for Detecting Axial Fuel Motion

As shown in Fig. I.E.17, the fuel element to be tested is positioned at the bottom of a stainless steel tube. A pushrod fits into the element tube and rests in contact with the fuel. This pushrod fits into a spring-loaded piston which ensures that the pushrod will be in continuous contact with the fuel and will keep the fuel element at the bottom of the fixture tube. Motion is transmitted from the fuel through the push rod to the piston. The axial location of the top of the piston is detected by a Bently-Nevada Corporation proximeter probe. In the range of interest, the proximeter output changes 0.1 V for each 0.001 in. of movement. For the tests, the fixture was inserted into a furnace to a depth slightly above the end of the fuel-element cladding. The amount of expansion of the fixture when heated was determined before the tests by using a quartz rod in place of the fuel element. The entire fixture is designed to fit into a Mark-I TREAT loop.

Figure I.E.18 shows the results of thermal cycles of two fuel elements. Both elements were cycled to temperatures slightly less than 550°C until reproducible zero points at ambient temperature were obtained. One fuel element (S/N 1638) was taken to 610°C to observe the effect of temperatures greater than the phase-transformation temperature (552°C). The fuel in this element exhibited an axial growth of 0.026 in. at ambient temperature, which was due to the retained phase formed at the higher temperature.

Figure I.E.19 compares the normalized axial movement of one tested element with similar data for unirradiated fuel alloy, as reported by Zegler and Nevitt.* It also shows a response curve obtained during a TREAT transient with a high-swelling (low-silicon) fuel element preirradiated to 2.5 at. % burnup, as reported by Rothman et al.** The almost linear response of the slumped fuel is attributed to an averaging effect resulting from the nonuniformity of the temperature in the test furnace and the nonuniformity of the fuel itself over its 13-in. length.

*Zegler, S. T., and Nevitt, M. V., Structures and Properties of Uranium-Fissium Alloys, ANL-6116 (1961).
**Rothman, A. B., Renken, C. J., Stewart, R. R., Chakraborty, A. K., Dickerman, C. E., Dewey, G. G., Matras, S., and Hutchinson, D. R., Transient Behavior of "High-swelling" EBR-II Mark-IA Driver Fuel in TREAT (to be published).
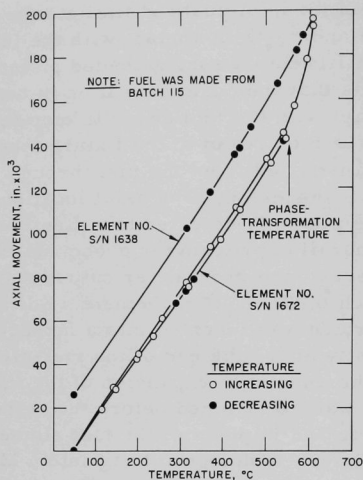
Fig. I.E.18. Axial Movement vs Temperature for Two Vendor-fabricated Driver-fuel Elements in Which the Fuel Had Slumped during Irradiation to 0.6 at. % Burnup
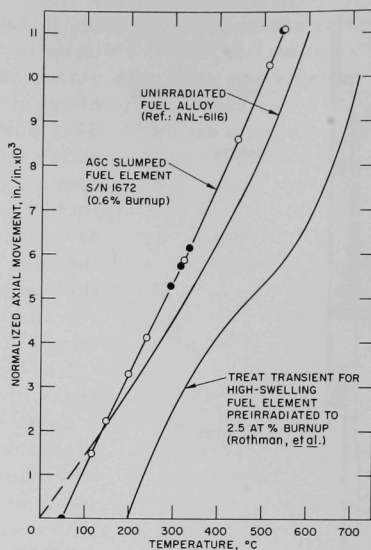
Fig. I.E.19. Comparison of Normalized Axial Movement vs Temperature for Slumped Vendor-fabricated Driver-fuel Element, Unirradiated Fuel Alloy, and High-swelling Fuel Element

An order has been placed for proximeter probes of a special design more suitable for use in a TREAT loop. Equipment is being designed to enable calibration of the fixture in a thermal configuration closely matching that expected in a Mark-I TREAT loop.

b. Comparison of Provisional Cladding-swelling Models and Correlations (J. R. Honekamp and G. H. Golden)

The ability of empirical correlations and theory-based models to predict fast-neutron-induced swelling of Type 304 stainless steel is being studied. Initial comparisons were made between provisional versions of one such model developed by ANL and two correlations, one made by PNL-Westinghouse, and the other by GE. Encapsulated elements from experimental subassemblies XG05 and XP12, irradiated in EBR-II, were used as a basis for the comparison. In each case, an estimate was made of the axial distribution of power, averaged over the history of the irradiation. This distribution was used to calculate corresponding temperature distributions in the element cladding and the capsule wall. The

correlations and models then were compared, using history-averaged fluence distributions based on neutronics calculations, together with the foregoing temperatures, to compute changes in diameter $(\Delta D/D)$.

The correlations used were: PNL-Westinghouse for Types 304 and 316 solution-treated stainless steel, which is*

$$100 \; \Delta V/V \; = \; 4.9 \times 10^{-49} \times (\phi t)^{1.71} \times 10[(1.55 \times 10^4/T) - (5.99 \times 10^6/T^2)],$$

and the GE correlation,**

$$100 \; \Delta V/V \; = \; 7.53 \times 10^{-5}(\phi t \times 10^{-22})^{1.62} \; (T - 360)^{0.898} \; (775 - T)^{0.711}.$$

In both of these correlations, $100 \; \Delta V/V$ = % swelling of cladding, and ϕt = fluence in neutrons/cm^2. The temperature (T) is in °K in the PNL-Westinghouse correlation and in °C in the GE correlation.

The Argonne model used was Harkness subroutine VϕI. Results of the calculations for Capsules F2H and C-17 are shown in Figs. I.E.20 and I.E.21, respectively. It is seen that the GE correlation significantly over-predicts the $\Delta D/D$; this was also found to be the case for Capsules F2R, F2C, and F2T from Subassembly XG05. The PNL-Westinghouse correlation and the Argonne model both gave closer agreement with measured values of $\Delta D/D$, although neither was consistently better than the other.
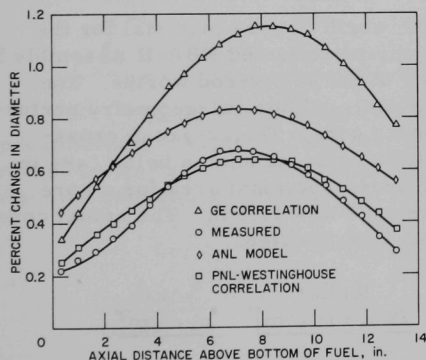
Fig. I.E.20. Measured vs Calculated Swelling of Type 304 Stainless Steel Capsule F2H from Subassembly XG05
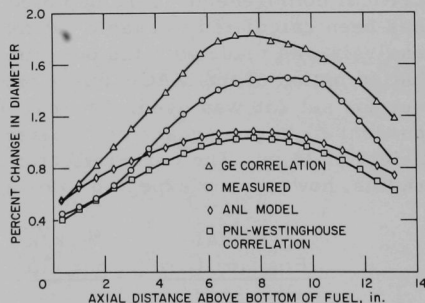
Fig. I.E.21. Measured vs Calculated Swelling of Type 304 Stainless Steel Capsule C-17 from Subassembly XO12

*Letter to Mr. James M. Shivley, Project Administrator, FFTF Program, Richland Operations Office, USAEC, "Fluence-temperature Dependency of Stainless Steel Swelling in FTR (12215-B-1)," August 18, 1969.
**General Electric Company, Nuclear Energy Division, Presentation Outline for Tenth General Meeting, "Irradiation Effects on Reactor Structural Materials," October 21-24, 1969, Fig. 10.

74

9. Physics Mock-up Studies

Last Reported: ANL-7640, pp. 76-78 (Nov 1969).

a. Estimate of ^{235}U Mass for EBR-II Assembly I (ZPR-3 Assembly 60) (D. Meneghetti)

It was estimated that the mass of ^{235}U for criticality of EBR-II Assembly I, the homogeneous-core depleted-blanket assembly, should be about 245 kg. This is for a core height of 13 in. and a homogenized core composition closely similar to the intradrawer loading containing one 1/8-in.-thick ^{235}U column, six 1/32-in.-thick ^{235}U columns, one 1/16-in.-thick 20%-enriched ^{235}U column, five 1/4-in.-thick sodium columns, one 1/8-in.-thick ^{238}U column, one 1/8-in.-thick U_3O_8 column, and two 1/16-in.-thick steel columns. A plate-heterogeneity effect of about 1% $\Delta k/k$ should reduce the mass of ^{235}U for criticality to 235 kg.

The larger fissile mass relative to that of usual EBR-II system loadings is due to the half-inch less axial height and to the smaller average fissile density of the critical-assembly core.

b. Estimated Radial Dependence of the Worth of Core Material for EBR-II Critical Assembly I on ZPR-3 (D. Meneghetti and K. E. Phillips)

The radial dependence of the worth of core material for the critical homogeneous-core depleted-uranium-reflected EBR-II Assembly I has been calculated to enable estimation of the safety-rod worths. The analysis was made with the one-dimensional, cylindrical-geometry perturbation option of the MACH diffusion-theory code. The 22-group cross-section set 238 was used. The calculated worths, tabulated below, are in percent $\Delta k/k$ per square centimeter of cross-sectional area for a core height of 13 in. The core-reflector interface was 11.5 in. The actual core radius, however, is expected to be about 1 in. greater.

Radial Position (cm)	%$\Delta k/k$ per cm^2	Radial Position (cm)	%$\Delta k/k$ per cm^2
0	0.030	20	0.020
5	0.029	25	0.016
10	0.027	29	0.013
15	0.024		

The same values can be used for safety-rod estimates for EBR-II Assembly II, the nickel-reflected assembly. In this case, however, the actual radius is expected to be close to the value used in the analysis.

c. **Estimated Effective Delayed-neutron Fractions and Inhour-reactivity Relationships for EBR-II Critical Assemblies I and II** (D. Meneghetti and K. E. Phillips)

The effective delayed-neutron fractions and inhour-reactivity relationships were calculated by the BAILIFF option of the MACH diffusion code for the homogeneous-core, depleted-blanket, critical EBR-II Assembly I and for the nickel-reflected critical EBR-II Assembly II. Spherical-geometry simulations were used, with separate calculations corresponding to radial and axial reflectors. The 22-group cross-section set 238 was used.

Table I.E.20 lists the calculated values of β_{eff}, Ih/%ρ, and prompt-neutron lifetimes for the case of a spherical core surrounded by the radial blanket and by the axial reflector. Results using two radii are listed to indicate the sensitivity of the values to the radial dimension of the core.

TABLE I.E.20. β_{eff}, Ih/%ρ, and ℓ_p for Spherical Approximations of EBR-II Critical Assembly I

Geometry:	Sphere			
Radius (cm):	27.65		30.19	
Reflector:	Radial	Axial	Radial	Axial
β_{eff}	0.00707	0.00701	0.00701	0.00694
Ih/%ρ	441	427	442	431
$\ell_p \times 10^8$, sec	9.5	60.2	9.7	55.6

Table I.E.21 lists corresponding quantities for spherical approximations of EBR-II Assembly II, the cylindrical EBR-II critical having nickel instead of depleted uranium as the radial reflector. The axial reflectors are identical with those for Assembly I.

TABLE I.E.21. β_{eff}, Ih/%ρ, and ℓ_p for Spherical Approximations of EBR-II Critical Assembly II

Geometry:	Sphere			
Radius (cm):	27.65		30.19	
Reflector:	Radial	Axial	Radial	Axial
β_{eff}	0.00684	0.00701	0.00679	0.00694
Ih/%ρ	436	427	439	431
$\ell_p \times 10^8$, sec	27.2	60.2	25.8	55.6

Both the nonfertile axial reflector composed of sodium and steel and the nonfertile radial reflector of Assembly II, composed of nickel, greatly increase the prompt-neutron lifetime relative to the depleted-uranium-blanketed case. The variations in the values of the quantities β_{eff} and $Ih/\%\rho$, however, are much smaller.

F. EBR-II--Fuel Fabrication

1. Cold Line Operations (D. L. Mitchell)

Last Reported: ANL-7655, pp. 78-79 (Dec 1969).

a. Cold-line Production and Assembly

The elements remaining when production of Mark-IA fuel elements was discontinued last month were bonded and bond tested. The cold line will continue to fabricate nonirradiated subassemblies and will complete the impact bonding of the 9764 unbonded vendor elements that remain to be processed. Production equipment for postbonding reclamation heat treatment of vendor-fabricated elements was assembled in the mockup area of the Fuel Cycle Facility and is being tested. Table I.F.1 summarizes the production activities for December 16, 1969 through January 15, 1970, for all of 1969, and for 1970 to date.

Eight Mark-IA subassemblies containing fuel elements made in the cold line were fabricated during the month.

No unbonded vendor elements were impact bonded during the month. Data relating to receipt, impact bonding, and acceptance of these elements are included in Table I.F.1.

The current number (as of January 15, 1970) of AGC elements available after verification inspection is 22,645. (This figure does not include the ANL-impact-bonded vendor elements.) Data relating to receipt and acceptance of the fuel produced by AGC are included in Table I.F.1.

G. EBR-II--Operations

1. Reactor Plant (G. E. Deegan)

Last Reported: ANL-7655, pp. 79-80 (Dec 1969).

During the period from December 21 through January 20, the reactor was operated for 817 MWd in Runs 39A and 39B. The cumulated total of EBR-II operation is 31,027 MWd.

TABLE I.F.1. Production Summary for FCF Cold Line

	12/16/69 through 1/15/70		1969 (Jan. 1-Dec. 31)		1970 (Jan. 1-15)
	Mark IA	Mark II	Mark IA	Mark II	Mark IA
Alloy-preparation runs					
New fuel	0	0	11	8	0
Remelts	0	0	18	3	0
Total	0	0	29	11	0
Injection-casting runs	6	0	52	10	0
Pins processed					
Accepted	408	0	4,860	941	0
Rejected	51	0	213	53	0
Elements welded	664	0	4,974	884	289
Elements rewelded	0	0	0	69[a]	0
Elements leaktested					
Accepted	752	0	4,645	804	577
Rejected	0	0	97	21	2
Elements bondtested					
Accepted	714	0	4,288	934	714
Rejected	28	0	423	9	28
Subassemblies fabricated (cold-line fuel)	8	0	38	6	7
Bonded elements received from vendor	0		24,313[b]		
Inspected and accepted	0		23,621[b,c]		
Inspected and rejected	0		1,251[b]		
Unbonded elements received from vendor for impact bonding by ANL	0		11,853[d]		0
Bonded, inspected, and accepted	0		1,979		0
Bonded, inspected, and rejected	0		190		0
Subassemblies fabricated (vendor fuel)	0		17[e]		0
Total elements available for subassembly fabrication as of 1/15/70					
Cold-line fuel					
Mark IA	847				
Mark II	234				
Vendor fuel (Mark IA)	22,645[f]				

[a]Includes 64 elements in which visual examination of welds indicated that they were not acceptable for potentially high-burnup experiments.
[b]Total includes figures for 1968.
[c]Includes fuel elements which were returned to vendor for rework to correct voids in sodium bond and after rework sent back to ANL for reinspection.
[d]Ten unbonded vendor elements were set aside for historical samples.
[e]Includes subassemblies made up of a mixture of vendor and cold-line fuel elements.
[f]This figure does not include vendor elements that were impact bonded by ANL.

On December 28, detection of smoke in the sodium-boiler plant was annunciated. An initial inspection revealed a small fire on the inlet piping of the secondary surge tank. The fire appeared to be of electrical origin. Heating circuits were de-energized, and the fire was extinguished. Further investigation revealed a small sodium leak at one of the valves for sodium vent on the side of the surge tank. Dripping sodium had apparently splashed on the lagging of the inlet line, thereby causing the fire. The reactor was immediately shut down, and the vent valve was closed. With the leaking stopped, an orderly cooldown of all systems to less than 400°F was conducted. The secondary system was drained, but all other systems were held at a temperature above 360°F to permit refilling as soon as the repair was made. The bellows on the vent valve was replaced, and leak detectors were installed in each of the five vent valves. After replacement

of lagging and heaters, the secondary system was filled, and all systems were heated to normal operating temperatures. Operation at 50 MWt was resumed until the end of the run, except for a brief test at reduced power and flow.

Fuel handling for Run 39B included insertion of the lower-leaky-weld test. A standard subassembly is used for this test, but the cladding of one of the elements has been predrilled to simulate a defective lower weld. After fuel handling, the seal trough of the small rotating plug was cleaned and filled. An approach to critical was performed; then the reactor was shut down for a reactivity adjustment. Upon restart, zero-power physics experiments were performed, after which power was raised to 50 MWt.

At the beginning of Run 39A, the capacity of the turbine-driven feedwater pump had been insufficient for 50-MWt operation. The pump was overhauled after the run. During the power increase in Run 39B, it performed satisfactorily and was returned to service.

After approximately three days of 50-MWt operation in Run 39B, levels of ^{133}Xe and ^{135}Xe activity in the cover gas had increased to more than a factor of two above their normal equilibrium backgrounds. Such an increase was not expected, even with the lower-leaky-weld test in the core. The reactor was shut down, and the test subassembly was replaced with a normal driver. The reactor then was restarted for Run 39C.

Fuel handling during the reporting period consisted mainly of the loading changes for Run 39B. These changes involved experimental sub-assemblies, as reported in Sect. I.E.4.a, and also included the following:

Four spent driver subassemblies were replaced. The 70%-enriched surveillance subassembly was reinstalled for irradiation during the last portion of Run 39. Following an approach to criticality, the reactor was shut down for a reactivity adjustment, which consisted of replacing a Row-6 half-worth driver subassembly with a depleted-uranium inner-blanket subassembly.

The loading change for Run 39C consisted only of replacing the lower-leaky-weld-test subassembly with a standard driver subassembly.

2. <u>Fuel Cycle Facility</u> (M. J. Feldman)

    a. <u>Surveillance</u> (M. J. Feldman, J. P. Bacca, and E. R. Ebersole)

        Last Reported: ANL-7640, pp. 80-81 (Nov 1969).

        (i) <u>Postirradiation Analysis of EBR-II Fuel</u> (J. P. Bacca)

            (a) <u>Surveillance of Vendor-produced Fuel</u>
                (A. K. Chakraborty and G. C. McClellan)

                (1) <u>Fuel-characterization Studies</u>

                      (A) <u>Subassembly C-2199</u>. The contents of Subassembly C-2199, which contained 27 fuel elements cast by the vendor and inpact bonded by ANL as well as 64 elements fabricated in the cold line, were examined after attaining a calculated maximum burnup of 1.35 at. % at the end of Run 38. Postirradiation fuel-swelling data for the 27 vendor fuel elements and 3 of the cold-line elements examined are summarized in Table I.G.1. None of these elements exhibited axial shortening of the fuel pin. Irradiation swelling of the fuel was similar to that observed in the past for ANL-fabricated fuel elements after comparable burnup.

TABLE I.G.1. Fabrication and Irradiation Data
for Driver Subassembly C-2199[a]

Calculated Burnup: 1.35 at. % max; 1.17 at. % avg.

Injection-casting Batch No.	Silicon Content of Fuel (ppm)	Number of Elements Examined	Element Burnup Range (at. %)	Total Volume Swelling of Fuel ($\Delta V/V$, %)	
				Average	Range
		Vendor Fuel			
AG 546	460	6	1.29-1.33	4.9	4.8-5.1
AG 577	440	8	1.27-1.34	5.0	4.7-5.5
AG 579	440	7	1.27-1.34	4.9	3.7-5.9
AG 580	390	6	1.27-1.34	5.3	3.7-6.3
		ANL Cold-line Fuel			
137 IH	440	3	1.33-1.35	4.9	4.3-5.6
		For Elements Examined		5.0	3.7-6.3

[a]Contained 27 vendor-cast, ANL impact-bonded fuel elements, and 64 ANL as-fabricated cold-line elements.

This subassembly is a part of the irradiation program intended to certify vendor-cast, ANL impact-bonded fuel elements for general use in EBR-II.

(B) <u>Subassembly C-2182</u>. Fuel elements from previously irradiated Subassembly C-2182, which attained a calculated maximum burnup of 0.88 at. %, have been reconstituted into a new subassembly (C-2251). These fuel elements were cast and centrifugally bonded by the vendor. As previously reported (see Progress Report for October 1969, ANL-7632, pp. 81-82), postirradiation examination of Subassembly C-2182 revealed axial shortening of the fuel pins that averaged 0.9 in. and ranged between 0 and 1.1 in. from the normal postirradiation pin length of 13.5 in. Even with this degree of fuel-pin shortening, diametral straining of the elements, as determined by precision measurements of the element diameters, was not observed. Reconstituted Subassembly C-2251, containing most (64) of the elements from Subassembly C-2182 and the remainder (27) from the cold line, has been proposed for irradiation for one more reactor run (in Run 40). This additional irradiation will result in an accumulated burnup of 1.3 at. % for the elements from Subassembly C-2182. This subassembly is a part of the irradiation program intended to investigate the allowable burnup capability of as-fabricated vendor fuel elements.

(C) <u>Subassembly C-2211S</u>. Fifty-six vendor-fabricated fuel elements from Subassembly C-2211S, which had attained a calculated maximum burnup of 0.39 at. %, have been reconstituted into a new subassembly (C-2252). As reported in ANL-7632 (pp. 78-79), these fuel elements, which had been cast and centrifugally bonded by the vendor, had been subjected to a corrective heat treatment by ANL. This treatment consisted of heating the elements to 660°C and holding them at that temperature for $1\frac{1}{2}$ hr, followed by air cooling to room temperature. This sequence was followed by heating to 500°C and holding for 2 hr in the cold-line bonders while the elements were subjected to 500 impacts. Postirradiation examination of elements from Subassembly C-2211S showed no shortening of the heat-treated fuel pins. Irradiation swelling of the fuel was similar to that observed in the past for ANL-fabricated fuel after comparable burnup. In addition to the 56 heat-treated vendor elements, reconstituted Subassembly C-2252 contains 35 ANL as-fabricated cold-line elements. It has been proposed to insert Subassembly C-2252 into the reactor at the beginning of Run 40 and to continue the irradiation of the elements from Subassembly C-2211S until they have attained an accumulated burnup of 1.5 at. %. Subassembly C-2252 is a part of the irradiation program intended to investigate the effectiveness of the ANL corrective heat treatment in removing preferred orientation (texture) in the fuel pins of the as-fabricated vendor elements.

(b) <u>Postirradiation Surveillance</u>. Results of the examinations performed on the subassemblies listed below are reported in Sect. I.E.7.b.

(1) <u>Controlled-flow Experiment</u>. Fuel-swelling data were obtained for Mark-IA and Mark-IB fuel elements that were in Subassembly C-2188S, which had achieved a calculated maximum burnup of 1.76 at. % by the end of Run 38.

(2) <u>Extended-burnup Subassemblies</u>. Subassemblies C-2168 and B-3039 were examined after achieving respective calculated maximum burnups of 1.78 and 1.73 at. %. Fuel-swelling data were obtained for elements from both subassemblies.

b. <u>Fuel Handling and Transfer</u> (P. Fineman)

Last Reported: ANL-7655, pp. 80-81 (Dec 1969).

Table I.G.2 summarizes the fuel-handling operations performed.

TABLE I.G.2. Summary of FCF Fuel Handling

	12/16/69 through 1/5/70	1969 (Jan. 1- Dec. 31)	CY 1970 (Jan. 1-15)
Subassembly Handling			
Subassemblies received from reactor			
Driver fuel (all types)	14	128	6
Experimental	1	22	0
Other (blanket)	1	6	0
Subassemblies dismantled for surveillance, examination, or shipment to experimenter			
Driver fuel	7	118	2
Experimental	2	22	0
Other (blanket)	1	4	0
Driver-fuel elements to surveillance	191	5602	61
Number from subassemblies	7	118	2
Subassemblies transferred to reactor			
Driver fuel			
From air cell	0	57	0
From cold line[a]	1	68	0
Experimental	1	9	1
Fuel-Alloy and Waste Shipments			
Cans to burial ground	2	29	0
Skull oxide and glass scrap to ICPP	4	7	0
Recoverable fuel alloy to ICPP			
Fuel elements	5 (87.15 kg of alloy)	35 (592.16 kg of alloy)	3 (52.28 kg of alloy)
Subassemblies	7 (34.26 kg of alloy)	20 (102.46 kg of alloy)	4 (20.55 kg of alloy)
Nonspecification material	0	5 (84.3 kg of alloy)	0

[a]Cold-line subassemblies, following fabrication and final tests, are transferred either to the reactor or to the special-materials vaults for interim storage until needed for use in the

c. Experimental Support (J. P. Bacca, N. R. Grant, V. G. Eschen, R. V. Strain, J. W. Rizzie, and C. L. Meyers)

Last Reported: ANL-7655, p. 81 (Dec 1969).

Subassembly XO44, a Mark-B7 irradiation subassembly containing one LASL capsule loaded with ceramic-insulator materials and six stainless steel dummy elements, was dismantled after attaining a calculated total fluence of 1.5×10^{22} nvt. After weight and diameter measurements and visual examinations of the LASL capsule were completed, the capsule was returned to the experimenter.

Interim examinations (weight, visual, and neutron-radiography) of the UNC mixed-carbide capsules (calculated maximum burnup of 6.0 at. %) from experimental Subassembly XO33, a Mark-A irradiation subassembly, were completed. Eighteen of these capsules will be reconstituted into a new subassembly (XO75), which will begin its irradiation at the start of reactor Run 40.

Interim nondestructive examinations of eight NUMEC mixed-oxide capsules that had attained a calculated maximum burnup of 6.3 at. % in experimental irradiation Subassembly XO15 also were completed. Subassembly XO70, a Mark-A irradiation subassembly, was assembled with these eight capsules plus the following ones: seven GE oxide-fuel capsules from Subassembly XO39; two LASL carbide-fuel capsules, one from Subassembly XO39 and one new; one new Westinghouse oxide-fuel capsule; and one new BMI nitride-fuel capsule.

Subassembly XO65A, a Mark-B37 irradiation subassembly containing 21 ANL helium-pressurized structural elements and 16 stainless steel dummy elements, was dismantled. The pressurized elements had accumulated a calculated total fluence of 0.4×10^{22} nvt. The diameters of the pressurized elements were measured. Preparations have been completed to reassemble these elements and a few new elements into Subassembly XO65B.

Unirradiated Subassembly XO74 was dismantled and examined in an attempt to determine why the flowrate of coolant when flowtesting the subassembly was lower than the rate when testing the prototype. (Subassembly XO74 is a Mark-H37 irradiation subassembly containing mixed-oxide fuel elements from the PNL-8 series.) No obvious explanation for the flow anomaly was found. The subassembly was reassembled using the same hardware and transferred to the reactor for additional flowtests.

PUBLICATIONS

A Study of the Dynamic Response of Various EBR-II Configurations to
Hypothetical Malfunctions in the Reactor System
    A. V. Campise
        ANL-7613 (Nov 1969)

Core-loading Diagrams for EBR-II Runs 4 through 38 (April 1965 through
mid-December 1969)
    J. C. Case
        ANL/EBR-007* (Dec 1969)

Measurements of Absolute Thermal Neutron Densities with Mica Fission
Track Recorders
    F. J. Congel,** J. H. Roberts,** R. J. Armani, H. Casson, R. Gold,
    J. Kastner, and B. G. Oltman
        Bull. Am. Phys. Soc. 15, 86 (Jan 1970)   Abstract

Investigation of Metallurgical Problems Associated with the EBR-II
Fusible Seals
    Charles C. Crothers
        ANL-7589 (Sept 1969)

Surveillance of EBR-II Blanket Subassemblies
    V. G. Eschen
        ANL-7597 (Sept 1969)

Absolute Calibration of Neutron Sources Having a Wide Range of
Emission Spectra
    A. DeVolpi and K. G. Porges
        Metrologia 5(4), 128-141 (Oct 1969)

The EBR-II Materials-Surveillance Program: I. Program and Results of
SURV-1
    Compiled by Sherman Greenberg
        ANL-7624 (Sept 1969)

Doppler Effect Studies Using Multilevel Formalism
    R. N. Hwang
        Nucl. Sci. Eng. 39, 32-49 (Jan 1970)

Analysis of the Linear Components of the Power-Reactivity Decrement
(PRD) in EBR-II
    John T. Madell and Richard E. Jarka
        ANL-7539 (Oct 1969)

---

*One of a series of "blueback" topical reports prepared by the EBR-II Project.
**Macalester College.

Spatially-Dependent Multigroup Cross Section Sets
    D. Meneghetti and K. E. Phillips
        A Review of Multigroup Nuclear Cross Section Preparation, Theory,
        Techniques, and Computer Codes, Workshop held at Oak Ridge,
        October 1-3, 1969. Radiation Shielding Information Center, USAEC
        Report ORNL-RSIC-27 (Jan 1970), pp. 69-72

Mathematical Model for Reaction Rate and Temperature Profile during
Oxidation of Magnetite Pellets
    K. Natesan and W. O. Philbrook*
        Ironmaking Proc., Toronto, TMS-AIME 28, 411-428 (1969)

Oxidation Studies of Zinc Sulfide Pellets
    K. Natesan and W. O. Philbrook*
        Abst. Bull. IMD-AIME, 26A (Dec 1968)

Oxidation Kinetic Studies of Zinc Sulfide in a Fluidized Bed Reactor
    K. Natesan and W. O. Philbrook*
        Abst. Bull. IMD-AIME, 26A (Dec 1968)

Argonne National Laboratory Critical Experiment Program
    C. E. Till, W. G. Davey, R. A. Lewis, and R. G. Palmer
        Proc. British Nuclear Energy Soc. Mtg. on Physics of Fast
        Reactor Operation and Design, London, June 24-26, 1969. Paper 1.3,
        p. 40-49

System for Measuring Sodium Level in EBR-II
    James B. Waldo and Lynn J. Christensen
        ANL-7623 (Oct 1969)

---

*Carnegie-Mellon University.

II. OTHER FAST REACTORS--OTHER FAST BREEDER REACTORS--FUEL DEVELOPMENT

A. Irradiation Effects, Mechanical Properties and Fabrication

1. Mechanical Properties of Austenitic Stainless Steels (R. Carlander)

Not previously reported.

As part of the transfer of GE-NSP's irradiation effects on cladding materials program* to ANL, irradiation capsules GEFP-2-107 and -138 were disassembled at the ANL Hot Cell Facility.

The capsules were irradiated in the ETR for three reactor cycles. The capsules contained tensile/creep-rupture specimens, 108 of Type 304 and 108 of Type 316 stainless steel in the annealed and 20% cold-worked conditions. The objective of the experiment is to determine the effects of a hardened neutron spectrum on the tensile and creep-rupture properties of austenitic stainless steels.

The irradiation conditions and capsule identifications are presented in Table II.A.1. The temperature history of the specimens during irradiation is being analyzed. Upon completion of the analysis, control specimens of the same composition and heat treatment will be thermally aged to simulate the in-reactor temperature effects on the mechanical properties of the two types of austenitic stainless steel. Both aged and irradiated specimens will be tensile and creep tested to determine the effects of irradiation in this neutron spectrum on the mechanical properties of Types 304 and 316 stainless steel.

TABLE II.A.1. Irradiation Conditions and Capsule Identification
of Austenitic Stainless Steels Irradiated in the ETR[a]

Capsule Identity	Design Features	Reactor Location	Estimated Fluence, n/cm^2 $(En > 1 \times 10^{21}\ MeV)$	Total Number of Specimens	Irradiation Temperature,[b] (°C)
GEFP-2-107	External boron and cadmium shields	K6SW	$1\frac{1}{2}$	36	480
				36	705
				36	590
GEFP-2-138	No shield	K6NW	$1\frac{1}{2}$	36	480
				36	705
				36	590

[a] Data furnished by C. V. Mullen, Jr., Idaho Nuclear Corporation.
[b] Design temperature.

---

*GEMP-1010, AEC Fuels and Materials Development Program Progress Report, No. 78, p. 46 (Dec. 31, 1968).

a. <u>Mechanical Properties of Cladding Materials</u> (F. L. Yaggee)

Last Reported: ANL-7655, p. 87 (Dec 1969).

All of the hardware necessary to study the effect of a vacancy flux on the minimum creep rate of austenitic stainless steel has been completed. The creep experiments will be performed while the specimen is irradiated in a cyclotron beam. The equipment is being assembled for proof testing, which will consist of conducting creep tests at temperatures between 25 and 600°C in the absence of cyclotron irradiation.

The temperature profile of the specimen-heating furnace will be determined between 200 and 800°C. Some difficulties have been experienced in obtaining a reasonably flat temperature zone across the specimen gauge length (1 in. long) when a single-element furnace (one zone) has been used. This difficulty is due to the chimney effect created by the draft through the vertical slot that provides access for the cyclotron beam to the specimen. If the slot is open at 300 and 400°C, the temperature gradient across the specimen is greater than 26°C; however, if the slot is closed at 200°C, this gradient is reduced to 10°C. Additional end windings and an aluminum microfoil (~0.0002 in. thick) may be used to cover the slot to reduce the temperature gradient. In order to gain operating experience with this equipment, the first proof tests will be made without the additional end heaters.

b. <u>Surface Defects as Failure Sites in Type 304 Seamless Stainless Steel Fuel-clad Tubing</u> (F. L. Yaggee)

Last Reported: ANL-7391, pp. 10-12 (Oct 1967).

It has been shown that surface defects penetrating only 4-5% of the wall of stainless steel fuel-cladding tubes (wall thickness of 0.015 to 0.020 in.) can seriously decrease rupture ductility, expressed in terms of diametral strain $(\Delta D/D_0)$, depending upon their location and orientation with respect to the axial tube direction. The previously presented data were for defect orientations parallel to the tube axis $(\beta = 0)$.* Specimens are being prepared for additional tests at 550 and 650°C for defect orientations of $\beta = 0, 45,$ and 90°. Information from these biaxial creep tests will be used to verify the predictions of an analytical analysis defining the effect of defect location and orientation on the rupture ductility.

---

*Yaggee, F. L., and Wang, I.-C., <u>Effect of Defects on the Rupture Ductility of Type-304 Stainless Steel Tubes under Biaxial Load</u>, Trans. Am. Nucl. Soc. 12(2), 570 (Nov 1969). Abstract

PUBLICATION

Parametric Influence of the Wall-Thickness Changes and the Bulk Strain
Behavior of Hollow-Drawn Tubing
J. E. Flinn

III. GENERAL REACTOR TECHNOLOGY

A. Applied and Reactor Physics Development

1. Theoretical Reactor Physics--Research and Development

    a. Theoretical Reactor Physics

        (i) Evaluation of Cross-section Data (D. A. Meneley)

Last Reported: ANL-7618, p. 83 (Sept 1969).

New versions of the codes CHECKER and DAMMET have been received from Brookhaven. These differ from previous versions in that some new formats are allowed. Both codes have been made operational with the CDC-3600, and are currently being converted for use with the IBM-360 system.

ENDF/B tapes 992, 997, and 991, containing preliminary Version II ENDF/B data, have been received. New formats pertaining to unresolved resonance parameters, inelastic scattering, and fission spectra require changes in ETØE and MC^2 before the data for 9 of the 12 new materials can be processed. Investigations into these changes are being made. In some cases the alterations required are quite extensive.

        (ii) Reactor Computations and Code Development (B. J. Toppel)

Last Reported: ANL-7655, pp. 90-96 (Dec 1969).

    (a) Flux Synthesis Calculations. In the Progress Report for November 1969, ANL-7640, p. 90, it was noted that gross errors in both the flux ϕ and k_{eff} occur in some flux synthesis calculations when using the boundary conditions $\phi = 0$ in the transverse direction. A more detailed analysis of the difficulty by means of another set of simplified calculations has shown that these results are not a consequence of errors in either the analytical formulation or its implementation in the synthesis code SYN1D. The difficulty, rather, is intrinsic to the system of synthesis equations and is associated with the fact that the required eigenvalue, the one that approximates the eigenvalue of the corresponding diffusion calculation, is not the dominant one. When this happens the iteration process built into SYN1D will naturally converge to the dominant eigenvalue and its corresponding flux, resulting in the gross errors reported.

A systematic study of the problem is now under way aimed at a better understanding of the difficulty and possible remedies for it.

(b) $\underline{MC^2 \text{ Capability in the ARC System}}$. The arrays in modules CSI001, CSC001, CSC002, and CSC003 have been variably dimensioned by the incorporation of BPØINTER into their structure. These modules have been tested for reliability by running problems with a wide variety of input options.

The MC^2 capability with these variably dimensioned modules permits the user to specify the amount of main core storage that he wishes to use for the variably dimensioned container array. For an MC^2 calculation with the IBM-360 computer, the container array in the main core of the computer is typically from 40,000 to 60,000 8-byte words in length. In addition, the user may specify additional storage for the container array in bulk memory. By means of BPØINTER the container array may be automatically extended into bulk storage and the user may specify any amount of storage up to 256,000 8-byte words. This flexibility enables the user to have a small container array (i.e., about 40,000 words) in the main computer core. This permits room for large buffers which will increase the running-time efficiency for I/Ø operations when large amounts of data are transferred from core to disk, and vice versa. With these variably dimensioned modules, one can limit the size of the container array, and this makes it possible to limit the total region size of the computer necessary to execute an MC^2 problem. This will enable us to run MC^2 problems and simulate a more restrictive computer region size than might be found in another computer installation.

Examples of computing-time comparisons for the various areas in the variably dimensioned MC^2 calculations in ARC are given in Table III.A.1. This table is an extension of Table III.A.6 in ANL-7655, p. 94. The timing considerations were run using the same problems as described in ANL-7655, but now with variably dimensioned arrays in modules CSI001, CSC001, CSC002, and CSC003 by the incorporation of BPØINTER into their structure.

A significantly longer running time was required for the variably dimensioned modules CSC001 and CSC003, which may be explained as follows. For a variably dimensioned subroutine in a module, the variables are passed through the subroutine argument list as opposed to the fixed dimensioned subroutine, where these quantities are passed through CØMMØN blocks. For a variably dimensioned subroutine, the compiler does not optimize as effectively as with a fixed dimensioned subroutine. This can be observed from the object module listing where there are added assembler language statements in the compilation of a variably dimensioned subroutine. The effect of the longer, less efficient compilation occurring in loops which are repeated a large number of times results in a longer running time for a variably dimensioned subroutine. One finds this most apparent in the resolved resonance calculation in module CSC001. This argument was true also for the variably dimensioned

unresolved resonance calculations in module CSC001, but this increase in running time was offset by the decrease in time spent in a revised version of subroutine QFJ.* This revised version uses an 8-point Gaussian integration to evaluate the J function. On the other hand, the old version of subroutine QFJ has a 16-point Gaussian integration. Both versions have comparable accuracy.

TABLE III.A.1. Timing Considerations

Module	Area	P1 Fine-group Problem Area (Time, sec)		P1 Ultrafine-group Problem Area (Time, sec)		Consistent P1 Ultrafine-group Problem Area (Time, sec)	
		Pres Prod MC^2 Capbl	Varbl Dimsn MC^2 Capbl	Pres Prod MC^2 Capbl	Varbl Dimsn MC^2 Capbl	Pres Prod MC^2 Capbl	Varbl Dimsn MC^2 Capbl
Input (CS1001)	Read Input, Adjust Broad-group Structure, and Make Consistency Check of All Input Data	2	2	2	2	2	2
	Total Time in Modules CS1001	2 (<1%)	(<1%)	2 (<1%)	(<1%)	2 (<1%)	(<1%)
Calculate Unresolved and Resolved Resonance Cross Sections (CSC001)	Reading Unresolved and Resolved Data, and W Table from ENDF/B Library	10	12	10	12	10	12
	Subroutine Finds the Maximum Number of Isotopes for the Materials in Problem, Max Number of Energy Points in Unresolved Calculation for Materials in Problem, and Max Number of Resolved Resonances in Problem	-	2	-	2	-	2
	Unresolved Calculation	80	61	80	61	80	61
	Resolved Calculation	631	714	708	802	708	802
	Total Time in Module CSC001	721 (87%)	789 (85%)	798 (47%)	877 (62%)	798 (44%)	877 (58%)
Calculate Nonresonant Cross Sections, Calculate Fundamental-mode Fluxes, and Iterate on Buckling to Critical (CSC002)	Subroutine Finds the Max Number of Energy, Sigma Pairs for Use in FIGERØ	-	6	-	6	-	6
	(Subroutine FIGERØ) Calculates Fine-group Effective Cross Sections for Nonresonant Quantities	44	44	49	49		49
	Subroutine Finds the Max Number of Energy, Sigma Pairs for Any Energy and for Any Material in INSCAT	-	12	-	12	-	12
	(Subroutine INSCAT) Calculates Inelastic and n,2n Cross Sections	12	11	12	12	12	12
	(Subroutine SØURCE) Calculate Fine- and Ultrafine-group Fission Spectrum	<1	<1	3	3	3	3
	Input/Output Operations	3	4	15	19	15	16
	Buffer Legendre Data from ENDF/B Library	-	-	69	64	69	64
	Calculation in Subroutine ALRAGØ for 1st Iteration	-	-	519	117	586	171
	Calculation in Subroutine PØNE for 1st Iteration	-	-	2	2	2	2
	Time Spent in Subroutine ALRAGØ for 2nd through 4th Iterations	-	-	24	9	37	21
	Time Spent in Subroutine PØNE for 2nd through 4th Iterations	-	-	6	6	6	6
	Total Time in Module CSC002	60 (7%)	78 (8%)	699 (41%)	299 (21%)	779 (43%)	362 (24%)
Calculate Broad-group-averaged Macroscopic and Microscopic Cross Sections, Calculate Broad-group Fundamental-mode Fluxes (CSC003)	(Subroutine AVER) Collapse the Ultrafine- and Fine-group Cross Sections	<1	1	11	6	19	9
	(Subroutine AVER1) Compute Individual Material Microscopic Cross Sections	42	48	188	224	201	241
	(Subroutine BGPØNE) Generate Homogenized Macroscopic Broad-group Cross Sections	<1	2	1	2	1	2
	Variable Dimension, Input/Output	-	2	-	4	-	4
	Total Time in Module CSC003	44 (5%)	53 (6%)	200 (11%)	236 (16%)	221 (12%)	256 (17%)
	Total Running Time for Problems (sec)	827	922	1699	1414	1800	1497

*Toppel, B. J., et al., ANL-7318 (June 1967).

In subroutine ALRAGØ in module CSC002, the data sets which write the microscopic elastic transfer cross sections for each Legendre material were changed from direct access I/Ø to sequential I/Ø. The DCB parameter for these data sets was set to

DCB=(RECFM=VB,LRECL=888,BLKSIZE=7108).

Note the significant decrease in running time in subroutine ALRAGØ for the first iteration calculation using this scheme. This is due to the fact that these data sets are actually sequential, so that using the direct access I/Ø resulted in a substantial loss in efficiency. These sequential data sets are then read in subroutine AVER1 in module CSC003.

A large buffer size, BLKSIZE=16000, was used to increase the efficiency for the I/Ø operations for transmitting the homogenized elastic-scattering matrices from disk storage to the main computer core. This is evident from the decrease in time spent in subroutine ALRAGØ for the second through fourth iterations in module CSC002, and also for the decrease in running time in AVER in module CSC003.

(c) <u>Reactor Computation System</u>. To provide the MC^2 cross-section package in ARC with the capability to perform precise resonance-absorption calculations, the incorporation of the combination of RABBLE and RABID algorithms as a module in ARC that can be optionally involved by MC^2 is being investigated. A serious problem with the current versions of the RABBLE and RABID codes is their long running times. That these codes run longer than other codes is unavoidable because they treat heterogeneities explicitly and accurately, instead of using equivalence methods to reduce a heterogeneous to a homogeneous system. However, the running time of RABID and RABBLE can be reduced appreciably by lowering the number of times the Doppler-broadened line-shape functions are computed. This can be accomplished by specifying that only the N closest resonances contribute to the cross sections at a given energy point.

A version of RABBLE for homogeneous systems has been written in which the N closest resonances contribute to the cross sections at a given energy point, where N is an input quantity. This code was run for a mixture of carbon, ^{239}Pu, and ^{238}U to compute resonance absorption between 2 and 300 eV with several values of N. The results of these computations are given in Table III.A.2. The absorption cross sections for ^{238}Pu and ^{238}U are for the energy range from 182 to 233 eV. Because this energy range contains the broad ^{238}U resonance near 190 eV, we have an indication as to how sensitive to N are group resonance cross sections. From the table it appears that including ten resonances will probably give adequate resonance cross sections for energy ranges in which both fissile and fertile nuclides have resolved resonances. At higher energies, where only the widely spaced resonances of ^{238}U are resolved, fewer resonances need be included.

TABLE III.A.2. Running Times for RABBLE
for a C/Pu/U Cell between 2 and 300 eV

N	CPu (sec)	σ_a^{49} (b)	σ_a^{28} (b)
2	29.4	19.219	12.748
6	39.8	19.393	15.719
10	50.4	19.578	15.931
14	60.3	19.694	15.896
18	69.9	19.754	16.092

When the same problem was run with an older version
of RABBLE, the running time was approximately 4 min. In the older ver-
sion, a resonance contributed to the cross section at an energy point if
(a) its energy was within the ultrafine group containing the energy point or
(b) the total cross section at the boundaries of the ultrafine group was
greater than a specified value. It is seen that the new procedure of including a
specified number of closest resonances reduces the RABBLE running time
for homogeneous cells to acceptable levels.

2. Nuclear Data--Research and Development

    a.   Cross Section Measurements   (N. D. Dudey)

    (i)   Spectrum-averaged Measurements

Last Reported: ANL-7632, pp. 100-102 (Oct 1969).

Determinations of capture-to-fission ratios (alpha) for
samples of fissile materials irradiated in various positions in EBR-II are
continuing. Radiochemical analyses of the ^{235}U samples have been com-
pleted, and mass-spectrometric analyses of the samples are nearing com-
pletion. Radiochemical analyses of the ^{240}Pu samples have begun.

A computer code MODSIG has been developed to compute
spectrum-averaged cross sections from differential cross sections and
multigroup reactor-physics calculations. The main feature of this code is
a calculation that smooths the group fluxes obtained from reactor-physics
calculations and provides the shape of the flux distribution in a differential
form. The differential cross sections are introduced into the code in the
form of a polynomial expansion obtained by weighted least-square fitting
to the cross-section data. The analytical expressions for the flux and
cross sections are then multiplied and numerically integrated over the
neutron-energy range of interest to provide a spectrum-averaged cross
section, $\bar{\sigma}$.

Several analytical forms for smoothing the group fluxes are being investigated. Evaluation has been completed of a Maxwellian function of the form

$$f(E) \propto E^{-1/\nu} \exp(-E/T), \tag{1}$$

where ν and T are adjustable parameters that define the shape of the function. Equation (1) has been used to smooth group fluxes of 16 groups, 22 groups (generated from two different cross-section sets), and 375 groups; in each case, the parameter ν was varied from 2 to 100, and T varied from 0.6 to 1.29; spectrum-averaged cross sections were generated by the method described above. A 22-group set was also used to generate spectrum-averaged cross sections by successively collapsing the groups to evaluate $\Delta\bar{\sigma}/\bar{\sigma}$ as a function of the number of groups. Finally, $\bar{\sigma}$ values were computed directly from the group fluxes with no smoothing applied, and these were compared with the $\bar{\sigma}$ values determined with smoothing.

The conclusions of the evaluation are as follows:

(1) If 12-16 energy groups are used over the energy region to which a monitor reaction is sensitive, the computed $\bar{\sigma}$ values are insensitive (to within <2%) to the choice of parameters in $f(E)$; in fact, the use of group fluxes without smoothing gives an accuracy of about 3%.

(2) If only 4 energy groups are used, as is often the case for threshold reactions, the details of the smoothing function can be very important; without smoothing, errors can be >20%.

(3) With 4 energy groups, a reasonable choice of the parameters ν and T enables computation of spectrum-averaged cross sections which agree to within 5% of $\bar{\sigma}$ values computed from a multigroup set of 375 energy groups.

(4) For spectra of the EBR-II type, the optimum parameters appear to be $\nu = 5$ and $T = 0.9$ near the core center, and $\nu = 20$ and $T = 0.7$ in the blanket region.

With the use of a Maxwellian form of smoothing function this method of calculating spectrum-averaged cross sections in EBR-II introduces, at worst, an uncertainty of 5%. (Uncertainties in the energy group fluxes and differential cross sections are additional sources of error.) Evaluations of other forms for smoothing the energy groups are now in progress.

b. Reactor Code Center (M. Butler)

Last Reported: ANL-7655, pp. 100-101 (Dec 1969).

During January, four new program packages were incorporated in the Center library. All were developed at Knolls Atomic Power Laboratory for the CDC-6600 computer.

STINT3 (ACC No. 389) solves static and time-dependent systems of coupled, one-dimensional diffusion-type equations in slab geometry. The code provides for temperature feedback and control-rod motion, and was designed primarily for solving single-channel flux-synthesis equations. SORSDB (ACC No. 391) was written to calculate the stress intensities and fatigue-usage factors for pressure vessels in accordance with ASME Code. The input requires the basic membrane and bending stresses generated by SOR2 (ACC No. 80). The two remaining packages are both associated with the KAPL DATATRAN System. One, ACC No. 406, consists of the DATATRAN two-dimensional geometry input modules; the second, ACC No. 407, contains the DATATRAN utility-plotting modules.

Distribution figures for the last quarter of calendar 1969 show a total of 197 program packages prepared and shipped to requesters.

Four programming notes were written and issued during January. Three were written to describe corrections and changes to be made in the GAMTEC-2 (ACC No. 185), FLANGE-1 (ACC No. 247), and the IBM-360 PDQ-7 (ACC No. 275) programs. The fourth contained information and additional material on the auxiliary DATATRAN program packages (ACC Nos. 406 and 407).

B. Reactor Fuels and Materials Development

1. Fuels and Claddings--Research and Development

a. Behavior of Reactor Materials

(i) Development of Temperature-gradient Vacuum Furnace (R. O. Meyer)

Last Reported: ANL-7640, pp. 96-98 (Nov 1969).

The design of a versatile temperature-gradient apparatus is essential for successful operation of our temperature-gradient migration program. The apparatus was described in ANL-7640 and is depicted in Fig. III.B.1.
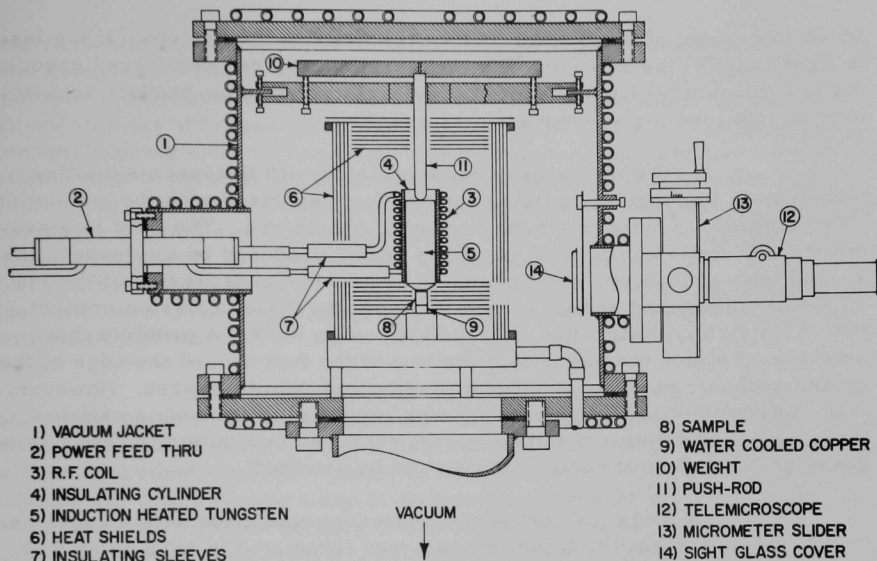
1) VACUUM JACKET	8) SAMPLE
2) POWER FEED THRU	9) WATER COOLED COPPER
3) R.F. COIL	10) WEIGHT
4) INSULATING CYLINDER	11) PUSH-ROD
5) INDUCTION HEATED TUNGSTEN	12) TELEMICROSCOPE
6) HEAT SHIELDS	13) MICROMETER SLIDER
7) INSULATING SLEEVES	14) SIGHT GLASS COVER

VACUUM

Fig. III.B.1. Temperature-gradient Vacuum Furnace

b.   Chemistry of Irradiated Fuel Materials (C. E. Crouthamel)

(i)   Development of Techniques of Fuel Analysis

Last Reported: ANL-7632, pp. 107-108 (Oct 1969).

Work is in progress to develop a method of determining the total quantity and relative radial distribution of noble fission-product gases retained in irradiated fuels. Current effort is directed toward developing techniques for determining the relative radial distribution of ^{85}Kr from analysis of microsamples taken by laser-beam vaporization. Previous attempts to analyze the released gases for total xenon and krypton with a quadrupole mass spectrometer were unsuccessful (see ANL-7632).

In the method of analysis presently being evaluated, a sample is beta-counted for ^{85}Kr (half-life of 10.5 yr) with a proportional counter; the actual amount of ^{85}Kr present will be determined from data obtained by counting selected samples with an absolute beta counter.*

The experimental procedure is as follows: (1) the laser is focused on a selected area of the fuel sample held within a vacuum chamber, (2) the chamber is evacuated and inactive krypton carrier gas is

*This work is being performed by J. Gray of the Chemistry Division.

added to prevent adsorption of ^{85}Kr on the walls of the system, (3) the laser is fired, and (4) the released ^{85}Kr and carrier gas are transferred cryogenically through a Millipore filter (to remove other fission-product activity) to a sample tube for subsequent beta-counting.

The major problem associated with the laser-sampling technique is in correlating the amount of fuel vaporized with the amount of ^{85}Kr released. Several methods are being considered. The first is a geometric calculation of the volume of the crater produced by the laser. The second method involves condensing the nonvolatile constituents of the fuel on a cover glass and analyzing this material for ^{144}Ce, a fission product that is uniformly distributed in irradiated oxide fuels. A problem that arises with either method is that melting of the fuel around the edge of the crater probably releases additional fission gas from that area. However, if the intensity of the laser beam can be regulated to produce a uniform temperature and uniform sample sizes, relative distributions of the fission gases as a function of radial position can be obtained.

An initial test of the procedure was made with a cross section of a 13% enriched UO$_2$ fuel pin that was irradiated in MTR to ~6.5 at. % burnup and cooled ~3 yr. Ten laser shots were made at various locations across the radius of the fuel pin. The gas released by the laser shots was beta-counted, and ^{85}Kr was easily detected in all regions of the fuel. Gamma-spectrometric analysis of the ^{85}Kr samples showed that separation from other long-lived fission products was excellent. In this preliminary test, sample sizes were estimated from the diameters of the craters on the assumption that the craters were hemispherical. Although large errors may be involved in this assumption, the results indicated that the concentration of ^{85}Kr in the outer, unrestructured region of the fuel was somewhat higher than in the columnar-grain region.

Work now in progress is being directed toward more accurate measurement of the sizes of the laser samples.

c. Thermodynamics of Fuel Materials

(i) Partial Pressures of Vapor Species in the Ternary U-Pu-C System (P. E. Blackburn and R. K. Edwards)

Last Reported: ANL-7632, pp. 108-109 (Oct 1969).

Mass-spectrometric studies of the vaporization of the uranium-plutonium-carbon LMFBR fuel are being made to determine the equilibrium pressures of the vapor species as functions of temperature and carbon concentration. These data are required to establish thermodynamic data for the fuel, including the activities of uranium, plutonium,

and carbon in the fuel. These activities are important in determining the fuel composition limits and/or fuel buffers necessary to limit uranium and plutonium activities to levels below those which would form low-melting alloys with the stainless steel cladding. In addition, the data may be used for establishing criteria necessary for limiting carbon solution in stainless steel to levels below those at which cladding embrittlement occurs, and for controlling activities of fission-product elements or carbides potentially corrosive to stainless steel. The data are also important in calculating material transport by vaporization, both in the operating fuel and during fuel synthesis. Studies will be made of $U_{0.8}Pu_{0.2}C_{1\pm x}$, corresponding to fuel with zero irradiation. Studies will then be made of simulated fuel with fission products.

The investigation of the binary Pu-C system, which had been undertaken first, was completed, and the final results were summarized in the Progress Report for July 1969, ANL-7595, p. 95; this work will be described in greater detail in the literature.* The Pu-C study was carried out with a Bendix time-of-flight mass spectrometer. However, the projected work with the ternary U-Pu-C system will be carried out with a quadrupole mass spectrometer, because the higher sensitivity of this instrument is required to measure with sufficient accuracy the partial vapor pressures of both uranium and plutonium over their ranges of anticipated variation. Studies of the Pu-O and U-Pu-O systems will also be made with this apparatus; this program is being supported under another activity.

The last report of the status of apparatus development was given with respect to the oxide studies in Progress Report for November 1969, ANL-7640, p. 125. The necessary performance tests of the effusion apparatus continue with uranium oxides prior to closing up the containing glovebox. The temperature of the effusion cell can apparently be held constant to better than our most sensitive detection limits ($\pm 5°C$). Because of this constancy, the effusing system should be truly invariant in a practical way at the congruently effusing composition; optimum conditions are consequently provided for determining the ionization-efficiency curves needed as part of the calibration information for our instrument. In the studies of uranium oxides, the preliminary curve for the UO species looks very satisfactory, and similar curves for the other species are being redetermined and evaluated for possible presence of ion fragments. Some slight drifting of ion-current values with time is being encountered, which may be due to drifts in either instrument electronics or sample temperature. Further work in calibration and assessment of the capabilities of the apparatus will precede the planned plutonium studies.

---

*Battles, J. E., Shinn, W. A., Blackburn, P. E., and Edwards, R. K., A Mass-spectrometric Study of the Volatilization Behavior in the Plutonium-Carbon System, High Temp. Sci. (in press).

Continuing theoretical analyses are directed toward simplifying the determination of ionization cross sections which are needed for converting ion-current observations to partial-pressure values, and toward analogous (but much more difficult) treatment of ternary systems.

d. Oxide Fuel Studies

(i) Fuel Element Modeling (T. R. Bump)

Last Reported: ANL-7595, pp. 2-4 (July 1969).

According to predictions of the fuel-element-lifetime code, SWELL, proposed mixed-oxide fuel elements for 1000-MWe LMFBRs often will fail first at the hot ends of the elements, where the cladding is the weakest. At least one of the 1000-MWe contractors has also predicted such behavior. Therefore, it would seem that longer-lived fuel elements might be obtained by (a) reducing the loads on the cladding at the hot end and/or (b) strengthening the cladding at the hot end.

According to the SWELL code (and other sources), loads on the cladding can be decreased by reducing effective fuel density (i.e., the fraction of the element cross section occupied by fuel), so that more room is provided inside the cladding to accommodate fission-product buildup. (This approach has merit only if the cladding loads are primarily due to fuel swelling rather than to gas-plenum pressure.) Thus it would appear that an optimum fuel-element design might employ a high effective fuel density at the cold end and a lower fuel density at the hot end, in order to increase fuel-element lifetime without degrading the average fuel volume fraction.

To illustrate the feasibility of this scheme, the SWELL code was modified to the SWELL-2D3 version,* which can treat effective fuel density as a function of axial position. SWELL-2D3 was used to investigate the effects of axial variations in effective fuel density on the lifetimes of mixed-oxide fuel elements having 0.300-in.-cladding OD, 0.015-in.-cladding wall thickness, a coolant inlet temperature of 780°F, a coolant temperature rise of 370°F, a plenum-to-fuel volume ratio (plenum at hot end) of 1.0, "EBR-II" constants, an average effective neutron flux of 4 x 10^{15} n/cm²-sec, average linear heat fluxes of 8-14 kW/ft, and an axial maximum-to-average neutron flux of 1.15. In the calculations, fuel enrichment was assumed to be constant and neutron flux was assumed to maintain its normal chopped-cosine axial distribution. The axial distribution of linear heat flux was varied accordingly to reflect the changes in axial distribution of effective fuel density. (In actuality, the axial distribution of neutron flux would also be changed somewhat with axial variations in fuel density.)

*SWELL-2D2 is also a new version that has the added capability of predicting overall changes of fuel-element length, as an aid to the comparison of predictions with experiments.

Two methods of varying the effective fuel density with axial position were studied: (a) only two discrete densities were used, the higher toward the element cold end, and the lower toward the hot end, and (b) linear density variation, again with the higher densities employed toward the element cold end. Either of these two methods appears to have the added benefit that the "fuel-slumping" accident would become less severe. The former method appears to be the simplest to apply in actual practice. A specific number of high-density pellets would be loaded into the cladding at one stage of assembly, with weights of individual pellets and total number and weight loaded monitored automatically. Subsequently, at a separate assembly stage, another number of lower-density pellets would be loaded and monitored in the same way.

Table III.B.1 gives some of the results obtained by studying the two-discrete-density method. According to these results, manipulating densities by this method should be done with care because fuel-element lifetime could be reduced instead of increased. Of all the combinations examined, Case 5 currently offers the most promise of delivering long life with a high average effective fuel density.

TABLE III.B.1. Predicted Effects of Employing Two Discrete Effective Fuel Densities in Mixed-oxide Fuel Elements

Case	Axial Avg Effective Fuel Density (% TD)	Effective Fuel Density at Fuel Cold End (% TD)	Fraction of Fuel Height Having Cold-end Fuel Density	Avg Linear Heat Flux (kW/ft)			
				8		14	
				Avg Burnup at End of Life (%)	Axial Position of Point of Failure (x/L_f)	Avg Burnup at End of Life (%)	Axial Position of Point of Failure (x/L_f)
1	85	85	1.00	5.2	0.75	5.0	0.58
2	85	90	0.50	3.8	0.42	4.2	0.25
3	85	95	0.50	2.2	0.42	4.6	0.42
4	85	90	0.33	5.8	0.75	4.2	0.25
5	85	95	0.33	11.0	0.75	9.4	0.58
6	75	75	1.00	8.8	0.75	8.6	0.75
7	75	80	0.50	13.2	0.75	9.4	0.92
8	75	85	0.50	4.4	0.42	8.4	0.08
9	75	80	0.33	10.8	0.75	10.0	0.92
10	75	85	0.33	13.2	0.75	8.4	0.08

Calculations were also performed in which the second method of varying effective fuel density, linearly with axial position, was employed. Here it was predicted that such variations should increase fuel-element lifetime as long as only gradual variations of density are used, but that steeper variations can cause lifetime to fall off.

Although some of the results seem inconsistent, when they are examined in detail they always are found to be consistent with the basic assumptions (correct or incorrect) of the SWELL code. These results

suggest that it would be worthwhile to investigate axial variations in clad-
ding wall thickness, simultaneously with effective-fuel-density variations,
to find a combination that would provide the maximum core fuel volume
fraction and minimum core steel volume fraction compatible with an
acceptably long fuel-element lifetime.

(ii) <u>Oxide-fuel Swelling Mechanisms and Models</u>
(R. B. Poeppel)

Last Reported: ANL-7640, pp. 103-106 (Nov 1969).

In order to provide a model for swelling and gas release in
oxide fuels, a counting procedure was developed (see Progress Report for
July 1969, ANL-7595, pp. 91-92) to calculate rather quickly, and with a
reasonable degree of accuracy, the fission-gas bubble-size distribution in
the fuel element. A rigorous derivation of this counting procedure was
given in ANL-7640. Before the procedure is employed in actual fuel-
element modeling, it should be tested against other methods of calculation.
Gruber[*] has performed the complete calculation of bubble coalescence in
which the bubbles undergo random walk by the mechanism of surface dif-
fusion. Gruber's analysis is completely dimensionless and can be applied
to any material.

In order to compare the new counting procedure with
Gruber's complete analysis, all of Gruber's approximations are taken
over directly. These include: (1) the gas can be described by the perfect
gas law, and (2) the gas pressure in the bubble is balanced by the surface
energy of the material. Gruber's Eqs. (1)-(3) were used in the present
calculation with $m = 2$. In Eqs. (2) and (3), $f(i)$ is given by

$$f(i) = 1/(m^n - m^{n-1}).$$

The largest n considered was $n = 10$, which corresponds to the largest
bubble considered, containing 1024 gas atoms. This is approximately the
size of Gruber's largest bubble. The contrast between the present calcu-
lation and Gruber's method is that Gruber used 200 equations and approxi-
mately 1 hr of computer time, whereas the present calculation uses
10 equations and less than 1 min of computer time. The results of the
two methods are identical for the mean radius and the total swelling.
Gruber's Fig. 3 was reproduced to within a few percent.

The short-cut counting procedure was also compared with
Gruber's results for biased migration. Mean radius and total swelling were
found to vary linearly with reduced time. The slopes, however, are greater
than those obtained by Gruber, 5.9 for the volume increase and 0.85 for the

[*]Gruber, E. E., J. Appl. Phys. <u>38</u>, 243-250 (1967).

mean radius. The calculation is quite sensitive to the largest bubble size considered. Gruber used bubbles that contained up to 10^6 atoms but, in the present calculation, the maximum n was 20 and m = 3, so that the largest bubble was 3^{20} or somewhat greater than 3 x 10^9 gas atoms.

(iii) <u>Fuel-element Performance</u> (L. A. Neimark, W. F. Murphy, and H. V. Rhude)

(a) <u>Irradiation of Group O-3 Fuel Elements</u>

Last Reported: ANL-7655, p. 103 (Dec 1969).

The Group O-3 encapsulated mixed-oxide fuel elements were loaded into EBR-II for Run 39. The elements are in Subassembly XO72 in position 6E2. At the end of Run 39A, 771 MWd had been accumulated toward the first target exposure of 9500 MWd (3.5 at. % burnup).

(b) <u>Out-of-reactor Simulation Experiments</u>

Last Reported: ANL-7640, p. 110 (Nov 1969).

A Centorr high-temperature furnace with controlled heating and cooling capabilities between 50 and 2500°C has been acquired for use in the study of fuel-cladding mechanical interactions. The tungsten heating element of the furnace will be enclosed in the center of a column of clad oxide fuel to simulate the internal heat generation within a fuel element. The furnace, which can be used with either a vacuum or an inert atmosphere, is being assembled. Tests with a furnace mockup showed that some modification of the lower liquid-metal contact of the axial tungsten heater will be necessary before temperatures above 1600°C can be achieved. At this temperature the liquid metal, which allows thermal expansion of the tungsten heating element, vaporizes significantly.

(iv) <u>Compatibility between Uranium-Plutonium Oxide and Cladding Alloys</u> (T. W. Latimer)

Last Reported: ANL-7581, p. 3 (June 1969).

Microhardness measurements were completed for three vanadium alloys containing 15 wt % chromium and 0-1 wt % titanium after contact with $(U_{0.8}Pu_{0.2})O_{1.97}$ for 1000 hr at 700°C. Previous compatibility tests have shown that oxygen diffused into vanadium and vanadium alloys at 700-800°C when in contact with this fuel composition. Although evidence of this increased oxygen content in the vanadium alloys cannot always be seen metallographically, these changes can be detected by microhardness measurements. The results of the microhardness measurements are

shown in Fig. III.B.2 and include the alloy V-15 wt % Cr-5 wt % Ti reported previously (see Progress Report for April-May 1969, ANL-7577, pp. 4-5). The vanadium alloys identified as V-15 wt % Cr-0.3 wt % Ti, V-15 wt % Cr-1 wt % Ti, and V-15 wt % Cr-5 wt % Ti actually contained 0.26, 0.97, and 5.5 wt % Ti, respectively.
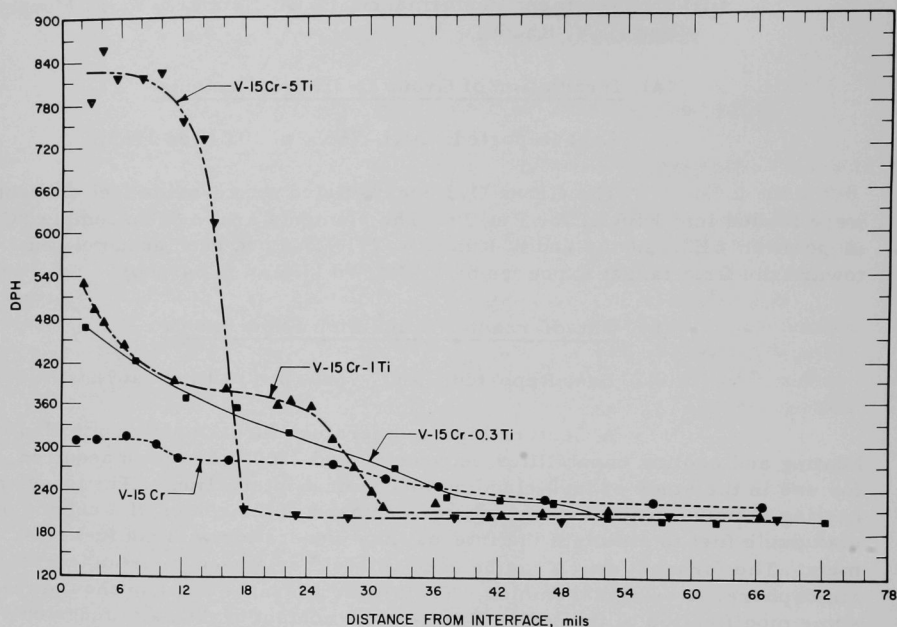

Fig. III.B.2. Effect of Titanium Additions on the Hardness Profiles of Vanadium-15 wt % Chromium Alloys in Contact with $(U_{0.8}Pu_{0.2})O_{1.97}$ for 1000 hr at 700°C

The tests show that even very small amounts of titanium in vanadium alloys significantly affect the hardness of these alloys in contact with $(U,Pu)O_{1.97}$. Previous tests at a temperature of 800°C have shown that vanadium alloys containing 0.75 at. % Zr (~1.3 wt %) were also considerably hardened by the fuel. The inverse relationship between the titanium content and the depth of the hardened zone found with alloys containing higher percentages of titanium was also found with these alloys (see Progress Report for October 1968, ANL-7513, pp. 3-4).

The hardness profiles of V, V-10 wt % Cr, and V-15 wt % Cr, after contact with $(U,Pu)O_{1.97}$ at 700°C, are compared in Fig. III.B.3. Under these test conditions, these curves tend to indicate that the relative change in hardness, and, therefore, the change in oxygen content, decreases as chromium is added to vanadium. Although the oxygen contents of the alloys were

not determined, studies of vanadium-chromium alloys containing 0-20 wt % Cr at equilibrium in cold-trapped sodium have shown a decrease by a factor of eight in the oxygen content as the chromium content was increased from 0 to 20 wt %.
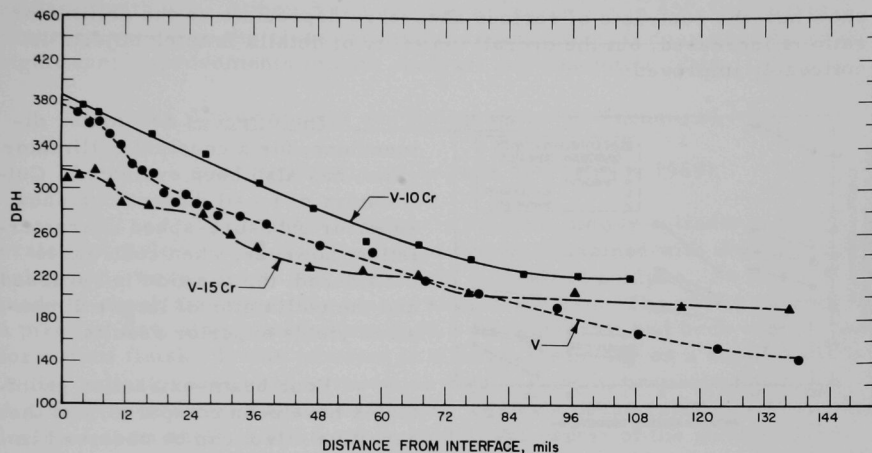

Fig. III.B.3. Hardness Profiles of Vanadium and Vanadium-Chromium Alloys after Contact with $(U_{0.8}Pu_{0.2})O_{1.97}$ for 1000 hr at 700°C

2. Techniques of Fabrication and Testing--Research and Development

a. Nondestructive Testing Research and Development (H. Berger)

(i) Neutron Radiography (J. P. Barton)

Last Reported: ANL-7618, pp. 96-97 (Sept 1969).

Studies of small-source neutron radiography that utilize a $141 - \mu g$ ^{252}Cf source are continuing.

A dominant effect in thermal-neutron radiography that uses a small source is the limitation of image quality due to interference effects from unwanted radiations. As the collimation is improved, the ratio of useful, collimated neutron radiation to interference radiation decreases. It is, therefore, important to determine the optimum combination of parameters, which include collimation ratio, collimation dimensions, beam-extraction geometry, detection, and shielding.

Collimator ratios over the range from 30:1 to 7:1 have been evaluated. The exposure times corresponding to a constant radiographic density do not vary in proportion to the square of the collimator ratio, as

would have been anticipated from considerations of inverse-square law. Reasons for this lack of proportionality could be that (1) radiographic density is not entirely due to collimated neutrons, (2) collimators with smaller aperture converge more precisely on the peak thermal flux, and (3) smaller collimators cause little flux depression in the source region. Results also show how the contrasts of various absorbers depreciate as the collimator ratio is increased, but the overall visibility of details in thick objects is noticeably improved.
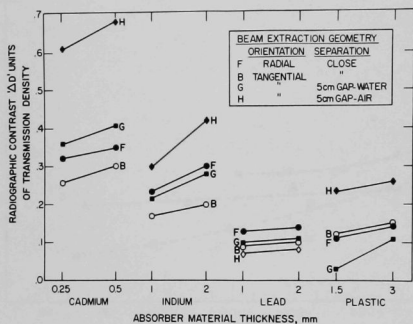
Fig. III.B.4

Experimental Evaluation of Contrast Capabilities in ^{252}Cf Thermal-neutron Radiography for Four Absorber Materials and for Four Beam-extraction Geometries. Collimator ratio in each case is 15:1, with an inlet aperture of 25 mm.

The effect of collimator dimensions, for a constant collimator ratio, has also been evaluated. Collimators of small dimensions show superior exposure-speed characteristics; however, when contrast is considered, the position is reversed and the collimator of larger dimensions yields superior results.

Four beam-extraction geometries have been compared, and the sensitive effect can be observed in Figs. III.B.4 and III.B.5. Geometry F corresponds to the collimator pointing directly at the source and with the aperture close to the source. Note the high contrast for lead, which is due to the gamma-ray contamination.
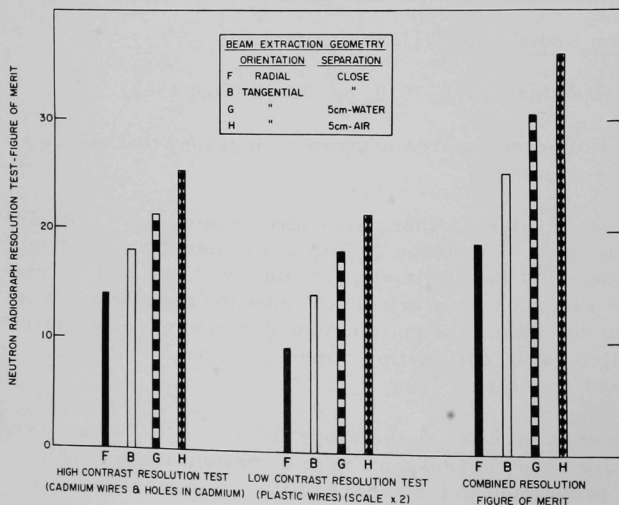

Fig. III.B.5

Resolution Capabilities in ^{252}Cf Thermal-neutron Radiography for Four Beam-extraction Geometries. Collimator ratio in each case is 15:1, with an inlet aperture of 25 mm.

Geometries B, G, and H correspond to the collimator passing tangentially by the source in order to avoid direct gamma radiation. In B the aperture is immediately beside the source, in G a 5-cm gap filled with water is between the aperture and the source, and in H the water in the 5-cm gap is replaced with air. Although the air-gap arrangement is 50% less rapid in exposure rate than the close tangential arrangement, it does provide very significant improvements in both contrast and resolution tests.

(ii) <u>Laser Studies and Holography</u> (N. Fernelius)

Last Reported: ANL-7640, p. 111 (Nov 1969).

The objects previously studied, mainly cylinders, had moderately complex surfaces. The fringe systems obtained with double-exposure holography were curved and, therefore, difficult to analyze. An attempt was made to check the theory for a very simple surface. The object chosen was a piece of flat, aluminum bar stock (6.5 cm wide) that had been vapor blasted for a matt finish. It was mounted in a moveable holder on a small lathe bed. A dial indicator was used to measure displacements, accurate to ±0.0002 in. A diverging reference beam was used. The axis of the reference beam was inclined at an angle of 20° from normal at the center of the photographic plate. The lathe bed axis was normal to the photographic plate. The double-exposure holographic-interferometry technique was used. Between exposures the aluminum bar was displaced along the axis of the lathe bed in one series of exposures, and perpendicular to the axis in another series. Reasonably vertical fringes were obtained for perpendicular displacements. For movement perpendicular to the axis of the lathe bed, a displacement of 0.0002 in. yielded 1 fringe, and a displacement of 0.008 in. yielded 40 fringes, which was about the limit of fringes that could be resolved easily. For movement along the lathe axis, 1 fringe was obtained for a displacement of 0.0005 in. and about 50 fringes for 0.010 in. The bar was mounted on a sextant head and rotated around a vertical axis between exposures. A rotation of 1/2° of arc, which was the smallest attainable, was great enough to wash out the fringe system. A He-Ne laser, with a wavelength of 25 μin. (6328 Å), was used. The smallest movement that yielded 1 fringe was 0.0002 in., or eight wavelengths. In summary, these studies indicate that holographic interferometry studies are not as sensitive as people had been led to believe. Claims have been made of sensitivity down to one-tenth of a wavelength.

b. <u>NDT Measurement of Effective Cold Work in Cladding Tubes</u>
(N. J. Carson and C. J. Renken)

Last Reported: ANL-7655, pp. 106-107 (Dec 1969).

This program is a study of the feasibility of measuring the effective cold work in cladding tubes by nondestructive testing (NDT)

techniques. The work is aimed specifically at AISI Type 316 stainless steel tubing of the size and shape to be used in FFTF. This program is divided into two elements: (1) the characterizing of cold-worked tubes to be used in standardizing the NDT techniques, and (2) the screening of potentially suitable nondestructive testing techniques.

A series of 18 rods, 0.300 in. in diameter, was prepared with reductions* of 0-40%. The starting material was AISI Type 316 stainless steel bar obtained from PNL. It was reduced from $1\frac{3}{16}$ in. in diameter to 0.566 in. in diameter by rolling, and was annealed for 30 min at 1850°F. The annealed rods were then reduced 48% to 0.408 in. in diameter and machined to make long, tensile specimens. The reduced diameter of each specimen was calculated to produce a rod 0.307 in. in diameter after a specific elongation. The tensile specimens were again annealed for 30 min at 1850°F.

Each tensile specimen was elongated and diameter measurements taken along its length. Percent reduction in area was calculated from diameter measurements made before and after, and plotted as a function of position for each rod. The heavier ends were then removed or reduced, and the entire rod was reduced to a uniform diameter on a centerless belt grinder. Each rod was then etched in a 50:50 solution of HCl and water at 70°F to a diameter of approximately 0.300 in.

The worked layer produced in centerless belt grinding penetrated less than 0.001 in. The amount of metal removed by etching, which was approximately 0.003 in. on the diameter, was more than sufficient to remove the worked layer.

One set of worked rods was preserved for screening NDT techniques; another set was sectioned for destructive analysis. Samples with reductions from 0 to 40% were prepared for transmission electron microscopy (TEM) and are being examined. Another series of samples are being examined by optical microscopy. Both longitudinal and transverse sections were prepared from samples with eight different degrees of reduction between 0 and 35%. Each sample was electrolytically etched twice: first in a solution containing equal parts of nitric acid and water, then in a solution of 5% oxalic acid in water.

The outstanding feature of the worked microstructure is the presence of deformation twins in the highly worked samples. Twinning became obvious at between 10 and 15% reduction, and continued to increase through 35% reduction. The sample reduced 35% was examined by X-ray diffraction and yielded a pattern indicative of a face-centered-cubic structure only.

---

*All reductions are in percent by area.

The fact that the presence of a deformation-produced second phase, such as body-centered-cubic martensite or ferrite, was not detected was encouraging, since it increased the probability that simple microhardness measurements could be used to indicate cold work. Indeed, this was found to be the case. A series of hardness measurements was made of annealed Type 316 stainless steel using loads of 50, 100, 200, 500, and 5000 g. Ten measurements were made at each load with sufficient distance between measurements to avoid any interaction. The average reading obtained was found to decrease as the load increased; however, the difference between the highest and lowest value obtained with a given load showed no significant trend.

Two of the lighter loads, 50 and 500 g, were used to make measurements on the worked specimens. The lighter loads were preferred since more readings could be obtained per unit length. This is important when making measurements across a narrow section such as a tube wall. Indentations made with a 50-g load could be placed completely within a single grain, those made with the 500-g load were slightly larger than an individual grain. Thus, the effect of the grain boundaries on the hardness values obtained with the 50-g load should be quite small, whereas the effect on the measurements made with the 500-g load should be near maximum.

The best curve obtained is that shown in Fig. III.B.6. Each point is the average of ten readings made with a Leitz MINILOAD Hardness Tester and a 500-g load. The correlation appears to be good for the entire range, and can be considered linear between 10 and 35% reduction.
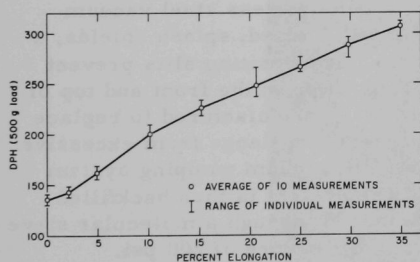

Fig. III.B.6. Microhardness of Type 316 Stainless Steel after Elongation at Room Temperature

Experiments were also conducted to determine the minimum distance required between readings in order to prevent interactions. This minimum distance was determined to be less than 0.005 in. when measuring the hardness of fully annealed steel with a 500-g load.

3. Engineering Properties of Reactor Materials--Research and Development

a. High Temperature Mechanical Properties of Ceramic Fuels

(i) Growth of Single Crystals of Uranium Carbide
(J. L. Routbort and M. D. Odie)

Not previously reported.

The mechanical properties of ceramics are determined by grain boundaries, porosity, and stoichiometry. The relative contributions of these variables are difficult to resolve from measurements obtained from polycrystalline material. The influence of stoichiometry may be studied best with single crystals. Changes in stoichiometry will have a great effect on all physical properties of the carbides because of the influence of the carbon atom on bonding. Single crystals are also necessary for reliable investigations of the elastic constants and diffusional parameters. In order to understand the fundamental plastic and elastic properties of candidates for advanced fuels, measurements must be obtained from both single and polycrystalline material.

In 1963 single crystals of UC were grown by electron-beam melting.* The high-temperature elastic constants** of these crystals were impossible to measure because of the high attenuation that resulted from the large subgrain structure. Crystals of good quality are difficult to grow in a vacuum because the melting point of most monocarbides is noncongruent. For this reason, the radiofrequency induction-heating technique, developed by Precht and Hollox[†] for the growth of TiC and VC, was used to grow UC crystals.

We have employed a modified commercial zone refiner manufactured by the Lepel High Frequency Laboratory. The apparatus consists of a 50-kW (450-kHz) radiofrequency generator, a vacuum chamber, and drive mechanisms. The water-cooled stainless steel vacuum chamber has two viewing ports with motorized, slotted, splash shields, a vacuum port, and a port for the power leads. The rotating slits prevent the windows from clouding, and permit observation of the front and top of the molten zone. A coaxial feedthrough is being manufactured to replace the straight feedthroughs to prevent the power-lead flange from excessive heating due to stray radiofrequency. The 2-in. vacuum pumping system evacuates the chamber to 3×10^{-6} Torr. The system is then backfilled with purified helium (ultrapure helium is passed through a molecular sieve and a titanium getter at 650°C) to a maximum pressure of 200 psi.

The cylindrical specimen is held in place by upper and lower support rods. These water-cooled stainless steel rods enter the vacuum chamber through "O"-ring seals. The upper rod may be driven up or down, independently of the lower rod, to change the shape of the zone or to accommodate density changes in the starting material. The lower rod may be rotated at speeds as high as 100 rpm to keep the liquid-solid interface flat in order to promote growth that would be normal to this interface. Both rods may be driven simultaneously so that the sample is

*Nadler, H., NAA-SR-7465 (1963).
**Routbort, J., and Maiya, P. S., ANL-7606 (1969).
[†]Precht, W., and Hollox, G., RIAS Report 68-c (1968).

moved through the coil at speeds from 1 to 600 mm/hr. The starting material, which is in the form of a cylinder, is fastened to the upper support rod by three set screws and to the lower support rod by tantalum clips. This arrangement allows the sample to contract in a strain-free manner upon cooling. Expansion effects are eliminated by having a gap between the halves of the starting material. A zone 3-5 mm high is achieved by a two-turn radiofrequency coil that is made from 4.8-mm square tubing with a 16-mm diameter. Power for this coil is supplied by the generator that operates through a 12-1 transformer.

Initial operation of the crystal-growing furnace has been satisfactory. A 1.25-cm-dia rod of UC was zoned at 18 mm/hr under 80 psi helium pressure, by using 15% of the available power. The large crystal that was produced is shown in Fig. III.B.7. The single-crystal portion has a length of 9 cm and a diameter of 1.25 cm, as well as a mass of ~140 g. A typical Laue back-reflection X-ray is also shown. X-rays taken along the length of the crystal indicated that it was a single crystal with very little subgrain structure. However, examination of the cross section of this sample revealed a few interior grain boundaries. This substructure possibly may be removed in subsequent passes by using slower zoning speeds, higher power, and a rotation at the liquid-solid interface.
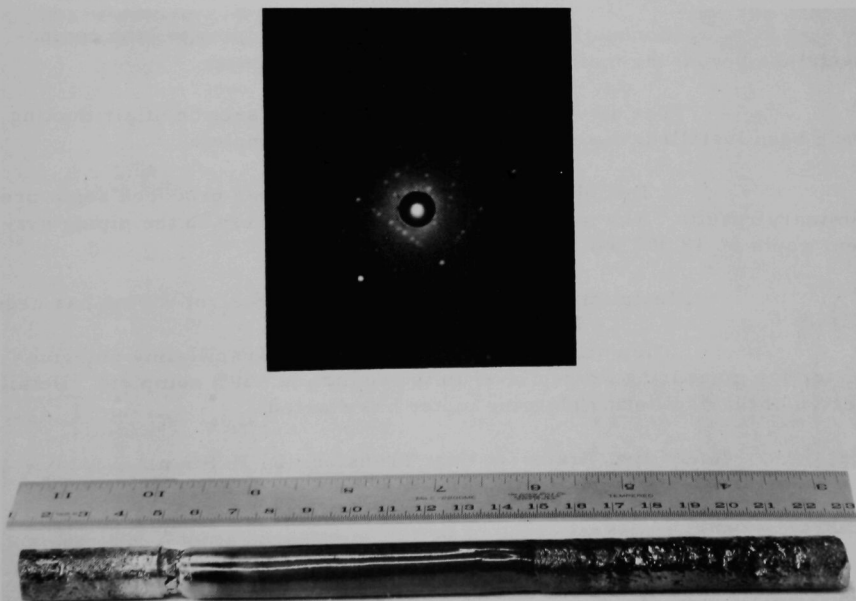

Fig. III.B.7. Single Crystal of Uranium Carbide (9 cm in length and 1.25 cm in diameter) Grown by Zone Melting Using Radiofrequency Induction Heating. A typical Laue back-reflection pattern is also shown.

Chemical analysis will determine if any concentration gradients exist in the crystal or if gas contamination has occurred during growth. If concentration gradients exist, either a zone-leveling technique or heat treatment in a suitable atmosphere will be used to control stoichiometry. A closed-loop feedback system is being designed to control the plate current, which will stabilize the radiofrequency power. This will make the operation semiautomatic. During the next several months, optimum growth conditions will be developed to produce high-purity, large, UC single crystals of varying stoichiometries.

C. Engineering Development--Research and Development

1. Heat Transfer and Fluid Flow (M. Petrick)

a. LMFBR Burnout Limitations (R. J. Schiltz and R. Rohde)

Last Reported: ANL-7655, p. 110 (Dec 1969).

(i) Preparation of Apparatus. A formal safety review of the system has been conducted; it revealed no major problems affecting the construction schedule.

Connection of sections of the main piping to loop components has begun; the main piping system is 60% complete.

The air-duct transition piece and a section of air ducting have been installed; the air-duct system is ~75% complete.

A flexibility analysis of the piping has produced some preliminary results. The largest thermally induced stress in the piping system would be 18,300 psi, which is satisfactory.

Installation of instrumentation and control wiring has begun.

The enclosure for a hot trap and an oscillating plugging meter for measuring oxygen level in the sodium is ~80% complete. Detail design of the oscillating plugging meter has started.

b. Nonboiling Transient Heat Transfer (R. P. Stein)

Last Reported: ANL-7655, pp. 110-111 (Dec 1969).

(i) Analyses of Heat-Flux Transients. A generalized mathematical relationship for predicting forced-convection heat transfer during heat-flux transients was given in the Progress Report for August 1969, ANL-7606, pp. 105-108. To apply this relationship, numerical values of certain coefficients are needed. A tabulation of these coefficients for the

case of a parallel plane duct was also given in ANL-7606. Coefficients for the circular tube case were given in the Progress Report for October 1969, ANL-7632, pp. 116-118.

The relationship can be used to approximate the pin-bundle case by considering that each pin is surrounded by an equivalent annular space with turbulent velocities and eddy diffusivities corresponding to zero shear stress at the equivalent outer wall. The relationship reduces to the same form as for the circular tube [see Eq. (1) on p. 116 in ANL-7632]. Because circumferential variations of temperature and heat flux are to be expected in a pin bundle, the surface temperature, wall heat flux, and fully developed heat-transfer coefficient that appear in this relationship are treated as circumferential-average values. Values of the various coefficients are listed in Table III.C.1 for cases of pitch-to-diameter ratios of 1.1 to 1.5. The usual hydraulic equivalent diameter is used in the Reynolds number and in the dimensionless axial length and time variables that appear in the equation.

TABLE III.C.1. Values of Coefficients for Pin-bundle Geometry Having Pitch-to-diameter Ratios of 1.1 to 1.5

Re	Pr	β	$-R_1$	R_2	$-R_3$
10^4	0.00316	2.804	0.181	0.169	0.167
	0.01	0.977	0.163	0.153	0.151
	0.0316	0.400	0.125	0.117	0.115
	1.0	0.137	0.0106	0.00985	0.00967
3.16×10^4	0.00316	0.938	0.172	0.162	0.159
	0.01	0.371	0.136	0.127	0.126
	0.0316	0.192	0.0816	0.0762	0.0751
	1.0	0.110	0.00429	0.00398	0.00391
10^5	0.00316	0.354	0.144	0.135	0.133
	0.01	0.176	0.0897	0.0838	0.0826
	0.0316	0.119	0.0408	0.0381	0.0374
	1.0	0.0929	0.00160	0.00149	0.00146
3.16×10^5	0.00316	0.164	0.0968	0.0905	0.0891
	0.01	0.108	0.0454	0.0423	0.0416
	0.0316	0.0895	0.0169	0.0157	0.0154
	1.0	0.0811	0.000580	0.000538	0.000528
10^6	0.00316	0.0990	0.0496	0.0463	0.0455
	0.01	0.0808	0.0188	0.0174	0.0171
	0.0316	0.0749	0.00633	0.00587	0.00577
	1.0	0.0722	0.000206	0.000191	0.000187

Computations were performed for pitch-to-diameter ratios of 1.1, 1.3, and 1.5. It was found that the coefficients are essentially independent of pitch-to-diameter ratio in this range. However, it must be pointed out that the model used to approximate the pin-bundle is not considered to be very accurate for computing average heat-transfer coefficients when the pitch-to-diameter ratio is less than 1.3.

c. Electron-Bombardment-Heater Development (R. D. Carlson)

Last Reported: ANL-7632, pp. 118-119 (Oct 1969).

(i) Preparation and Test of 7-pin Clusters (3/8 and 5/16-in. OD x 24 in.). Design drawings are being prepared for the 7-pin cluster heater. Heater construction will begin after completion of the drawings.

(ii) Preparation and Test of Single Pin (1/4-in. OD x 25 in.). Experiments with various types of filaments are continuing; the development of a long-life filament remains a major problem.

The straight-wire filament has been modified. It was centerless ground so that a shoulder existed on each end to eliminate the bowing and twisting action inherent in a straight-wire filament. Tests showed no improvement. A second filament has been designed and machined in a half-radius. The flat sides are ceramic coated so that they are electrically insulated from each other. The two halves, with the ceramic-coated sides bearing against each other, are welded at one end; at the other end, the two half-moon sections are connected to terminals for the application of power.

Still another filament being evaluated is a coaxial-type filament. It consists of a tungsten wire that is ceramic coated and over which a tantalum tube is placed. One end of the tungsten wire is welded to the tantalum tube and the other two ends, consisting of a tantalum tube and tungsten wire, form the two terminals. This unit also has power applied at one end. These two filament designs are being investigated to determine the feasibility of incorporating them in an open-ended 1/4-in.-pin EB heater.

(iii) Preparation of Single Pin (1/4-in. OD x 36 in.). Development and final assembly of a sodium-to-water-cooled single-pin heater are nearing completion. This unit will be able to operate at 1200°F.

d. Heat Transfer in Liquid-Metal Heat Exchangers (D. M. France)

(i) Feasibility Studies of Liquid-metal Steam Generators Employing Thermal-convection Tubes (D. M. France)

Not previously reported.

Studies of liquid-metal-heated steam generators have been resumed with emphasis on evaluating methods of heat-transfer prediction and exploring alternative conceptual approaches. The desirability of developing more accurate analyses and exploring new conceptual configurations is underscored by the poor test results obtained in the ALCO-BLH 30-MW prototype steam generator.* Wide discrepancies between predicted and measured performance occurred.

A new concept for a liquid-metal-heated steam generator is being analyzed. The new system is capable of performing the function of both the shell-and-tube steam generator and the shell-and-tube intermediate heat exchanger of the conventional system. It employs a modified heat pipe, termed a thermal-convection tube, to transfer heat directly from the primary sodium to the water at large heat fluxes and nearly isothermal conditions. The principal difference between a thermal-convection tube and a heat pipe is the absence of a wick in the thermal-convection tube. Thus, the problems of lifetime and boiling associated with the presence of a wick are eliminated. The mechanism of heat transfer in a heat pipe as well as in a thermal-convection tube is the latent heat of vaporization.

The deletion of an intermediate heat exchanger from the thermal-convection tube heat-transfer system is founded upon a comparison of radiation paths in this system and in the shell-and-tube system. A liquid-metal working fluid in the thermal-convection tubes serves the same purpose as the secondary sodium in the intermediate heat exchanger. Thus, the entire liquid-metal loop and peripheral apparatus associated with the intermediate heat exchanger can be eliminated. The thermal-convection tubes are individually sealed units, and stresses due to high-temperature expansion are circumvented because the tubes need not be rigidly fixed at the ends.

The thermal-convection tube heat-transfer system has two safety features not found in the shell-and-tube heat exchangers. In the event of a single rupture in a tube there would be no sodium-water contact in the thermal-convection tube system, and the water would not be continuously pumped into the sodium. Both of these phenomena occur subsequent to a tube rupture in a shell-and-tube system. Sodium-water contact would not occur in a thermal-convection-tube system unless two ruptures occurred in a single thermal-convection tube.

The performance parameters and characteristics of the proposed concept are being compared with current conventional designs of liquid-metal-heated steam generators. New and more detailed methods for heat-transfer prediction are being developed for this purpose.

---

*LMEC Monthly Report, August 1969, 69LMEC-2076, pp. 27-39.

2. Engineering Mechanics (G. S. Rosenberg)

    a. Structural Dynamics--Structure-Fluid Dynamics
       (M. W. Wambsganss, Jr.)

    (i) Mathematical Modeling of Parallel-flow-induced Vibration

        Last Reported: ANL-7640, pp. 120-123 (Nov 1969).

        In ANL-7640 an analytical solution for the displacement statistics of a simply supported rod in parallel flow was discussed. The solution was presented in the form

$$\Phi_{yy}(x,\omega) = D_e^2(\omega)\Phi_{pp}(\omega) \sum_n |H_n(\omega)|^2 \phi_n^2(x) J_n^2(\omega) \tag{1}$$

(this equation was inadvertently omitted from p. 121 of ANL-7640), where $\Phi_{yy}(x,\omega)$ is the mean-square-value spectral density of rod displacement, $D_e(\omega)$ is an effective rod diameter, $\Phi_{pp}(\omega)$ is the mean-square-value spectral density of the pressure, $\phi_n(x)$ is the orthonormal mode, $H_n(\omega)$ is the transfer function for the rod, and $J_n^2(\omega)$ is the joint acceptance. One of the several conclusions drawn from the analytical study is that the first bending-mode response is dominant.

        The effective rod diameter D_e, the joint acceptance J_n^2, and the mean-square-value spectral density of the pressure Φ_{pp} are typically presented as functions of the Strouhal numbers ν $(=0.275\ \omega D/V_c)$, γ $(=\omega \ell/V_c)$, and S $(=\omega \delta^*/V)$, respectively, where D is the rod diameter, ℓ is the rod length, δ^* is the displacement thickness of the boundary layer, V is the mean axial flow velocity, and V_c is the convection flow velocity. A parameter study based on the ranges of variables associated with planned tests of parallel-flow-induced vibration (these ranges are also typical of reactor components and environmental conditions) allows us to define the following realizable ranges on the Strouhal numbers as computed with the first-mode natural frequency: $(0.02 < \nu < 0.52)$, $(10 < \gamma < 180)$, and $(0.004 < S < 0.25)$. If the rod is relatively lightly damped, such that it is selective in responding to frequencies in the frequency range centered about its first natural frequency, the ranges defined above can be taken as the "effective" ranges of the Strouhal numbers. By means of the available experimental data, the effective diameter and joint acceptance can be approximated, within their respective ranges of effectiveness, by the power-function relationships

$$D_e = 1.3\ \nu^{1/2} = 0.68\ (\omega D/V_c)^{1/2};\ 0.02 < \nu < 0.52;$$

$$J_1 = 0.45\ \gamma^{-1/2} = 0.45\ (\omega \ell/V_c)^{-1/2};\ 10.7 < \gamma < 180, \tag{2}$$

respectively. Upon substitution into Eq. (1) the frequency dependence of the joint acceptance cancels with that of the effective diameter, and we obtain the simplified relationship for the first-mode response:

$$\Phi_{yy}(x,\omega) = (0.306/\epsilon)\phi_1^2(x)|H_1(\omega)|\Phi_{pp}(\omega). \tag{3}$$

The important feature of Eq. (3) remains the mean-square-value spectral density of the pressure. From Fig. III.C.1 of ANL-7640, we see that data are lacking in the effective range of Strouhal number S less than 0.25.

(ii) Preparation of Two Structural-dynamics Test Loops (P. L. Zaleski)

Last Reported: ANL-7640, p. 123 (Nov 1969).

The acoustic filter systems have been built. However, before they are installed upstream and downstream from the test section in the small flow loop, a flowtest is planned in which the characteristics of the pressure field in the test section will be measured. These data will be used to evaluate the effectiveness of the filters in reducing the acoustic disturbances induced by the pump and other sources.

b. Structural Dynamics--Flow Noise-Field Dynamics (M. W. Wambsganss, Jr.)

Not previously reported.

(i) Turbulent Boundary-Layer Wall-Pressure Fluctuation. The measurement and mathematical characterization of the convecting random pressure field are the cruxes of the study of parallel-flow-induced vibration. The spatially dependent characteristics of the pressure field, as obtained from cross-correlation measurements, enter into the equation for the mean-square-value spectral density of rod displacement, Eq. (1) above, through the effective diameter and joint acceptance terms; the time-dependent properties are implicitly contained in the mean-square-value spectral density of the pressure field. The required characterization of the pressure field necessitates cross-correlating signals from closely spaced transducers. To make these measurements, a procedure for constructing miniature pressure transducers was developed, and an instrumented tube containing six transducers mounted as three pairs of diametrically opposite transducers has been fabricated.

A flowtest was conducted using the instrumented tube. However, after several runs the rubber potting started to peel off several of the transducers and the test was terminated. The transducers have been rebuilt using a different potting technique; they are being calibrated before being flowtested further.

The pressure-time histories that were obtained from the abbreviated test have been analyzed. The resulting mean-square-value spectral densities are in good agreement with the results of earlier investigators (see Progress Report for November 1969, ANL-7640, p. 121, Fig. III.C.1). Of particular interest were the mean-square-value spectral densities at low Strouhal-number values (S < 0.25). In agreement with Willmarth and Wooldridge,* the spectra contained a large energy density at low frequencies; as a first approximation, the spectral density can be assumed inversely proportional to S for S < 0.25.

D. Chemistry and Chemical Separations

1. Fuel Cycle Technology--Research and Development

a. Adaptation of Centrifugal Contactors to LMFBR Processing (G. J. Bernstein)

Last Reported: ANL-7655, pp. 115-116 (Dec 1969).

The work in this program is directed toward extending a Savannah River centrifugal mixer-settler design to a configuration suitable for efficient handling of plutonium in the solvent extraction of LMFBR fuels. The principal advantage sought is an increase in nuclear safety through favorable geometry; additional advantages, demonstrated at Savannah River, include reduced radiation damage to the solvent and increased ease of operation. The scope of the program includes review studies of the design and performance of existing centrifugal mixer-settlers and correlation of performance with size and rotor speed. The correlations are to serve as a starting point for the design of an experimental unit of variable speed having the high length-to-diameter ratio required for adequate capacity and critically favorable geometry.

In the application of this design to the separation of dissolved plutonium and uranium from dissolved fission products in aqueous solution, the organic and aqueous phases would be fed into the top of an annular space, mixed by an axial rotor as they move downward (to extract uranium and plutonium into the organic phase), and would flow into the interior of the hollow rotor through an orifice in the bottom of the rotor. The phases would be separated by centrifugal force as they moved upward inside the rotor and would be discharged through ports at the top of the rotor into collector rings.

For plutonium concentrations expected in potential solvent-extraction processes, an ID of 5 in. for the stator (i.e., the casing) was calculated to be geometrically favorable to criticality control on the basis of

---

*Willmarth, W. W., and Wooldridge, C. Z., Measurement of the Fluctuating Pressure at the Wall beneath a Thick Turbulent Boundary Layer, J. Fluid Mech. 14, 187-210 (1962).

data* on safe diameters of infinite water-reflected cylinders of $Pu(NO_3)_3$ solution. Geometrically favorable configurations for the collector rings might be either a relatively small diameter and large height or a large diameter and small height. In any case, the diameters of the collector rings must be larger than the rotor diameter.

A plastic test unit has been built having a 3-in.-OD by 16-in.-long rotor spinning within a $3\frac{5}{8}$-in.-ID stator. Experiments on mixing-power input were conducted to establish whether adequate mixing power could be put into the annular mixing chamber to assure good contacting of the two phases. In these experiments, the inlet to the rotor was sealed so that the system would be nonflowing and no power would be used for pumping. The mixing-power input for this mixer under two different operating conditions (i.e., with and without baffles on the stator) was compared with the mixing power for a smaller mixer operated with and without baffles on the stator and blades on the rotor (see ANL-7655). Both mixers were operated at speeds up to ~2200 rpm. Although the difference in diameters of the two mixers was not great enough to allow a precise evaluation of the effect of an increase in diameter, results indicated that good contacting of the phases could be expected in larger units without blades on the rotor or baffles on the stator.

In other experiments with the larger plastic test unit having a 3/4-in. or $1\frac{1}{8}$-in. orifice in the base of the rotor, the water flow rate through the rotor was measured. Pumping rates as high as 16.8 gpm were obtained at 1700 ppm with the larger orifice, indicating that the desired throughput of 20 gpm will be achievable at ~3000 rpm with a new, larger unit that is being designed. The new centrifugal contactor will have a 4-in.-OD stainless steel rotor and an ~4.5-in.-ID stator. It will permit evaluation of the phase mixing and separating capacity of a two-phase system. Components for the latter unit, such as pumps and flowmeters, are being procured.

b. <u>Molten Metal Decladding</u> (R. D. Pierce)

(i) <u>Behavior of Volatile Fission Products</u>

Last Reported: ANL-7640, pp. 123-124 (Nov 1969).

(a) <u>Laboratory Process Development</u>. A portion of the fission-product iodine is expected to be present as elemental iodine in the annular and plenum regions of irradiated reactor fuel. In the present concept of decladding by use of a liquid metal, the iodine will be liberated when the cladding (stainless steel or Zircaloy) is dissolved in liquid zinc at 800°C.

The distribution of iodine between zinc, a cover salt, and the gas phase was measured in two experiments simulating the release

---

*Clark. H. K., Handbook of Nuclear Safety, DP-532, Table IV.28, p. 442 (Jan 1961).

of fission-product iodine during removal of cladding from fuel elements by dissolution in molten metal. In each experiment, a Pyrex capsule containing iodine was loaded together with zinc and LiCl-KCl salt into a quartz vessel. The capsule was immersed in zinc while the zinc was heated, and a stream of argon cover gas was passed through the quartz-vessel freeboard above the salt layer and into iodine absorbers downstream from the zinc. In these experiments, the capsule contained enough iodine to give a pressure of 10-15 atm at 800°C. As the capsule was heated, it softened. In the first experiment, rapid iodine release occurred at ~745°C. At the end of the experiment, no iodine was detected in samples of solidified zinc, in washings from the walls of the apparatus, or in the iodine absorbers. A substantial amount of iodine as zinc iodide was found in the LiCl-KCl cover salt.

In the second experiment, iodine release occurred at ~710°C. Again no iodine was found in the absorbers. Analysis of the cover salt for iodine by two methods gave results indicating that most or all of the iodine charged was in the cover salt.

The absence of iodine from all phases except the cover salt in these experiments indicates that the iodine gas bubbles reacted very rapidly with the molten zinc and that the resulting iodide ended in the cover salt. In current experiments, a mixture of 20 to 50 at. % iodine with argon is being used to simulate decladding conditions more closely.

c. Continuous Conversion of U/Pu Nitrates to Oxides (N. M. Levitz)

Last Reported: ANL-7655, pp. 117-118 (Dec 1969).

Conversion of uranium nitrate and plutonium nitrate solutions (produced in reprocessing plants) to an oxide is a necessary and presently expensive step in the nuclear fuel cycle. This conversion step must provide the fuel fabricator with powdered fuel oxides suitable for fabrication of fuel shapes. In addition, conversion of fissile nitrate solutions to a powder may be required for safe shipment.

Current conversion processes consist of a number of steps, among which are precipitation, filtration, and calcination. An alternative to these processes, which offers potential economic advantage, is continuous fluid-bed denitration of uranyl nitrate-plutonium nitrate solutions to a UO_3-PuO_2 powder form, followed by fluid-bed reduction to UO_2-PuO_2 powder suitable for fabrication into fuel shapes (pellets) for LMFBR fuels.

An integrated laboratory and pilot-scale program is in progress. Preliminary denitration experiments with uranyl nitrate solutions were done at 300, 400, 500, and 600°C to check out the laboratory-scale

equipment and the procedure. The solution was fed dropwise to a hot surface to effect denitration. Products formed at 400 and 500°C were selected for analysis by X-ray diffraction. The product formed at 500°C was determined to be gamma UO_3, whereas that formed at 400°C consisted of gamma UO_3 and $UO_3 \cdot H_2O$.

After installation of equipment in a glovebox, three experiments were done with $1.2\underline{M}$ $UO_2(NO_3)_2$-$0.3\underline{M}$ plutonium nitrate-2 to $4\underline{M}$ HNO_3 solutions at 300, 450, and 600°C. Approximately 6 g of oxide was prepared in each experiment. The product is being characterized by a number of analytical techniques, including X-ray diffraction, microscopic examination, and electron-microprobe examination.

Work is under way on a method for dissolving the oxide powder in nitric acid systems so that subsequently in the pilot-scale facility, denitration products may be recycled and the plutonium inventory minimized.

An absorption spectrophotometric technique is being developed to determine the nature (i.e., valence) of plutonium in feed solutions. Ultimately, the effects of the valence state on the character of the denitration product will be studied.

Accomplishments related to the pilot-plant facility for fluid-bed denitration included completion of the design of the fluid-bed denitration reactor and a start of installation of equipment items and instruments. A criticality safety concept for the facility is being reviewed that is based on maintaining a fixed maximum quantity of plutonium in the glovebox.

PUBLICATIONS

Fluid-Bed Fluoride Volatility Processing of Spent Reactor Fuel Materials
J. J. Barghusen, A. A. Jonke, N. M. Levitz, M. J. Steindler, and
R. C. Vogel
> Progress in Nuclear Energy, Ser. III, Process Chemistry, Vol. 4.
> Pergamon Press, Oxford, 1969, pp. 347-398

Stress-Strain Behavior of UO_2 at Elevated Temperatures
R. J. Beals and R. F. Canon
> Bull. Am. Ceram. Soc. 48(9), 879 (Sept 1969)   Abstract

High Temperature Mechanical Properties of Uranium Compounds
R. J. Beals, J. H. Handwerk, and G. M. Dragel
> High Temperature Technology, Proc. 3rd Int. Symp., Asilomar,
> California, 1967. Suppl. Int. Union Pure Appl. Chem., Butterworths,
> London, 1969, pp. 265-278

Behavior of Urania-Rare-Earth Oxides at High Temperatures
R. J. Beals, J. H. Handwerk, and B. J. Wrona
> J. Am. Ceram. Soc. 52(11), 578-581 (Nov 1969)

Some Experiments in Fast Neutron Radiography
H. Berger
> Mater. Eval. 27(12), 245-253 (Dec 1969)

Investigation of Laser Speckle from Surfaces of Vibrating Objects
N. Fernelius
> Bull. Am. Phys. Soc. 15, 44 (Jan 1970)   Abstract

Cladding Interactions in Mixed Oxide Irradiated Fuels
C. E. Johnson and C. E. Crouthamel
> J. Nucl. Mater. 34, 101-104 (Jan 1970)

Diffusion in Uranium Carbide by the Mass Transfer Method
P. S. Maiya and J. L. Routbort
> J. Nucl. Mater. 34, 111-113 (Jan 1970)

ERRATUM - Unitary Models of Nuclear Resonance Reactions [Phys.
Rev. 157, 907 (1967)]
P. A. Moldauer
> Phys. Rev. 182, 1360 (June 20, 1969)

Radiation Damage in Lithium Niobate
W. Primak, T. T. Anderson, and S. L. Halverson
> Bull. Am. Phys. Soc. 15, 52 (Jan 1970)   Abstract

Phase Diagrams for the Systems $MgCl_2$-MgF_2, $CaCl_2$-MgF_2, and $NaCl$-MgF_2
R. A. Sharma and I. Johnson
> J. Am. Ceram. Soc. 52, 612-615 (Nov 1969)

Study of the Reduction of UO_2 by Magnesium or Calcium Dissolved in Molten Chlorides
    R. A. Sharma and I. Johnson
        Met. Trans. 1, 291-297 (Jan 1970)

Fast Neutron Cross Sections of Hafnium, Gadolinium, and Samarium
    G. L. Sherwood, A. B. Smith, and J. F. Whalen
        Nucl. Sci. Eng. 39, 67-80 (Jan 1970)

Fast Neutron Incident on Holmium
    A. B. Smith and J. F. Whalen
        Bull. Am. Phys. Soc. 15, 86 (Jan 1970)   Abstract

Investigation of Low-Excitation States in ^{75}As by the $^{75}As(n,n'\gamma)$ Reaction
    D. L. Smith
        Bull. Am. Phys. Soc. 15, 86 (Jan 1970)   Abstract

Pyrometallurgical and Pyrochemical Fuel Processing Methods
    R. K. Steunenberg, R. D. Pierce, and L. Burris
        Progress in Nuclear Energy, Ser. III, Process Chemistry, Vol. 4.
        Pergamon Press, Oxford, 1969, pp. 461-504

Total Pressure of Uranium-Bearing Species over Oxygen-Deficient Urania
    M. Tetenbaum and P. D. Hunt
        J. Nucl. Mater. 34, 86-91 (Jan 1970)

Ultraviolet-Activated Synthesis of Plutonium Hexafluoride at Room Temperature
    L. W. Trevorrow, T. J. Gerding, and M. J. Steindler
        Inorg. Nucl. Chem. Letters 5, 837-839 (Oct 1969)

Some Mechanical and Physical Properties of Vanadium and Vanadium-Base Alloys
    F. L. Yaggee, A. R. Brown, E. R. Gilbert,* and J. E. Flinn**
        Abstract Bull. IMD-AIME, p. 75A (March 1969)

IV. NUCLEAR SAFETY RESEARCH AND DEVELOPMENT

A. LMFBR Safety--Research and Development

1. Accident Analysis and Safety Evaluation

  a. Initiating Accident Code Development (G. J. Fischer)

   Last Reported: ANL-7655, p. 96 (Dec 1969).

   (i) A New Routine for Slug Ejection of Coolant for SAS1A.
A model of coolant slug ejection similar to that of Cronenberg* is being
coupled with the heat-transfer routines in the SAS1A accident-analysis
code.** The new coolant routine will be an optional alternative to the model
of two-phase flow of coolant currently in SAS1A. The new slug routine
should require less computation time than the present routine. Also, the
slug model is probably more appropriate than the two-phase flow model for
flow-blockage cases and maybe for flow-coastdown cases.

   The new model will include the simultaneous solution of the
heat-transfer equations for the fuel, clad, and coolant, the momentum-
balance equations for the motion of the coolant, and the energy-balance
equations for the vaporization or condensation of the coolant.

   The physical model and the resulting differential equations
for use in the new coolant routine have been formulated, and so have been
the finite difference equations and numerical procedures for obtaining the
solution. The routine is currently being coded.

2. Coolant Dynamics (J. F. Marchaterre)

  a. Sodium Superheat (R. E. Holtz and R. M. Singer)

   Not previously reported.

   (i) Boiling from Surface Cavities

   (a) Out-of-pile Superheat Tests with Sodium from EBR-II.
Tests are planned to examine experimentally any effects on the incipient

---

*Cronenberg, A. W., III, Slug Expulsion of Boiling Sodium from a Reactor Coolant Channel, M.S. Thesis,
Northwestern University, Evanston, Illinois (1969).

**MacFarlane, D. R., Agrawal, A. K., Carter, J. C., Fischer, G. J., Heames, T. J., McNeal, N. A., Sha, W. T.,
Sanathanan, C. K., and Youngdahl, C. K., SAS1A, A Computer Code for the Analysis of Fast Reactor
Power and Flow Transients, to be published; MacFarlane, D. R., (Toppel, B. J., Ed.), The Argonne Reactor
Computation (ARC) System, ANL-7332, p. 191 (1967).

pool boiling of sodium that might be caused by long-term circulation of the sodium in the primary coolant loop of EBR-II. A representative sample of sodium from the EBR-II reactor system will be tested in a vessel identical to that used in the earlier low-heat-flux superheat tests so as to facilitate comparison with available data and to determine any possible differences.

b. <u>Sodium Expulsion</u> (R. M. Singer and R. E. Holtz)

Last Reported: ANL-7606, pp. 124-126 (Aug 1969).

(i) <u>Static Expulsion Tests. Analysis of Data and Interpretation in Terms of Physical Models</u>. Except for several runs to obtain additional pressure-pulse data, these tests have been completed. The data are being reduced and analyzed; a topical report or journal article will be prepared to summarize the conclusions.

(ii) <u>Forced-convection Expulsion Tests. Preparation of Transient Test Loop</u>. Work is continuing on the loop instrumentation and safety-interlock circuits. Void fraction, temperature, pressure, flowrate and liquid-film thickness instruments are being attached to a tubular test section before it is welded in place in the loop.

Continued tests of the high-speed data-acquisition system are under way. These tests are defining the capabilities and limitations of this system so that it can be adapted to meet the requirements of the Transient Test Loop.

c. <u>Sodium Simulations</u> (M. A. Grolmes and H. K. Fauske)

(i) <u>Expulsion of Nonmetallic Fluids from Single-tube Geometries (Static Tests)</u>

Last Reported: ANL-7655, pp. 128-131 (Dec 1969).

On-going experiments that produce the expulsion of non-metallic fluids superheated by rapid depressurization have shown two different modes of fluid ejection: a slug ejection and a flashing two-phase ejection (see Progress Report for January 1969, ANL-7548, p. 118). This latter phenomenon, as it applies to LMFBR accident analysis, appears to be important in later stages of expulsion in cooling action and coolant reentry in a blocked subassembly. Both Friz* and Gonidec** have reported

---

*Friz, G., "Coolant Ejection Studies with Analogy Experiments," <u>Proc. Conf. Safety, Fuels, Core Design in Large Fast Power Reactors</u>, ANL-7120 (Oct 1965).

**Le Gonidec, B., <u>et al.</u>, "Etudes Experimentales sur l'Ebullition du Sodium, Part II: Boiling by Plugging of a Canal," <u>Proc. Int. Conf. Safety of Fast Breeder Reactors</u>, Aix-en-Provence, France (Sept 1967).

a flashing ejection after depressurization to 1 atm of heated water. However, there are some important differences between those studies and the flashing phenomenon observed in recent ANL experiments that might influence the simulation. In particular, although no bubbles were observed and large superheats were recorded in the liquid column below the flashing interface in the ANL experiments, the presence of small bubbles in the liquid column was thought by Gonidec to indicate a saturated liquid condition. A typical pressure trace indicates that the pressure P_B at the base of the liquid column is much lower than the saturation pressure corresponding to the liquid temperature. Table IV.A.1 shows the rates of flashing expulsion and measured base pressures for six experimental runs. In all cases, significant liquid superheat is indicated during the expulsion. It has been suggested* that the two-phase flow from the interface is limited by critical flow and can be described by a model based on an energy, momentum, and continuity balance written about either side of the interface with the assumptions of saturated liquid conditions on one side and critical flow rate on the other. Although the assumption of a saturated liquid is not verified by the data listed in Table IV.A.1, it is interesting to note that an equilibrium critical flowrate

$$G = \left(\frac{\partial \rho}{\partial v}\right)_S^{-1/2}$$

(1)

evaluated at the measured liquid pressure P_B (which is different from the exit pressure) and an equilibrium quality X_{eq}, shows good agreement with three fluids. However, from visual observations, the flow might or might not be truly choked, depending on reservoir conditions (the extent of depressurization).

TABLE IV.A.1. Two-phase Flashing Expulsion Data for Freon-11, Water, and Methyl Alcohol

Run	Fluid	T_0 (°F)	P_R (in. Hg)	ΔT_{si}[a] (°F)	$\bar{P}_B$ (in. Hg)	ΔT_{SB}[b] (°F)	G_{exp} (lbm/ft²-sec)	G_{calc} (Eq. 1) (lbm/ft²-sec)
A	F-11	75	0.50	145	9.0 ± 3	54	98 ± 10	92
B	F-11	104	0.30	184	13.5 ± 3	66	130 ± 20	140
C	H_2O	161	0.30	117	6.5 ± 2	17	57 ± 4	50
D	H_2O	178	0.12	178	8.2 ± 2	25	69 ± 4	71
E	CH_3OH	123	0.21	133	5.66 ± 1	40	61 ± 6	60
F	CH_3OH	151	0.23	149	9.75 ± 1	36	78 ± 10	87

[a]Initial liquid superheat referred to reservoir pressure P_R.
[b]Liquid superheat during expulsion referred to liquid pressure P_B.

*Ibid., see previous page.

3. Core Structural Safety (C. K. Youngdahl)

Last Reported: ANL-7606, p. 127 (Aug 1969).

a. Dynamic Plasticity Analysis of Circular Shells

A topical report on load-equivalence parameters for dynamic loading of structures in the plastic range has been drafted and is being reviewed. A paper, "Correlation Parameters for Eliminating the Effect of Pulse Shape on Dynamic Plastic Deformation," has been submitted to a journal.

4. Fuel Meltdown Studies with TREAT

a. Transient In-pile Tests with Ceramic Fuels (C. E. Dickerman)

Last Reported: ANL-7632, pp. 131-134 (Oct 1969).

(i) Checkout-2 Experiment. The prototype loop, containing the UO_2 specimen used for the Checkout-2 loop meltdown test, has been shipped back to Argonne, Illinois, for disassembly and inspection of the sample remains. It was possible to ship the loop, containing the TREAT-irradiated UO_2, after a time delay for fission product decay by utilizing the loop "special form" container as a Spec 7-A shipping container. As reported previously, the sample failed vigorously in a transient which supplied approximately twice the energy required to melt UO_2. No detectable fuel fragments could be seen in the post-transient neutron radiographs of the loop test section and top and bottom return bends. The pump has too much structure for meaningful radiographs. After the transient, an attempt was made to reestablish sodium flow through the loop. Although the pump appeared to be all right electrically, no flow could be produced. A survey of loop activity has shown a strong source in the region of the top pump flange. Accordingly, this region of the loop will be checked carefully for an accumulation of fuel remains. The loop has been installed in the loop glovebox facility in the D-301 hot laboratory. The glovebox auxiliary transfer hood and transfer apparatus had been checked earlier with a "fresh" Mark-II loop. The prototype loop is now to be used for checkout of the complete facility before it is used for loops with mixed oxide pins. It appears likely that extensive disassembly of the loop, including removal of at least the pump section, will be required.

(ii) Power Calibration for Loop Meltdown Experiment with Irradiated UO_2. A meltdown experiment with a three-pin cluster of irradiated UO_2 fuel elements in a Mark-II loop is being planned. The pins to be tested are of 0.174-in.-OD, with 0.009-in. clad thickness and 0.150-in.-dia pellets. The fuel stack is 4.9 in. long. Original enrichment of the pins was

13 at. % and they have been irradiated to 6 at. % nominal burnup. The pins have been characterized by Stewart et al.*

In order to determine the ratio of sample energy release to TREAT energy release and to determine the power distributions within the three-pin cluster, a calibration mockup was irradiated in TREAT in January. The mockup consisted of pins geometrically identical to the test pins, but with 10% enriched, unirradiated UO_2 fuel. In addition, four fully enriched uranium foils were located outside the cladding of each pin, centered 1/8 in. and 3/8 in. above and below the axial centerline of the fuel stack. The foils were located at 90° intervals on the circumference of the pins.

Preliminary analysis of the data from the calibration run indicate that good uniformity of power density was obtained in the pins. The ratios of pin average power to assembly average power determined from gamma counting of the fuel pellets were 1.019, 1.001, and 0.980. The same ratios obtained from foil data were 1.014, 1.001, and 0.985. The axial power distributions obtained from gamma counts of the fuel pellets showed that no pellet had a power output that deviated from the average power output in its pin by more than 6%.

(iii) Mixed-oxide Pin Experiment. Another partially outfitted loop (the "B-1") was sent to TREAT during the report period for a calibration run with a mixed-oxide pin in preparation for the first TREAT loop mixed-oxide sample experiment. This experiment is to provide as complete as possible a check of the apparatus and procedures for this type of meltdown experiment. The energy input specified has been deliberately scaled down to 1350 J/g oxide, which is calculated to produce melting of about 30% of the oxide. (In Checkout-1, the pin received 1,700 J/g oxide without failing, and the rise of coolant outlet temperature was less than 100°C. In Checkout-2, the pin failed at an energy input of about 1,800 J/g.) The pin is contained inside a test-section mockup of a single flow channel, rather than a ring of dummy elements, in order to simulate the environment of a single pin inside a cluster. Since the first experiment, and the subsequent ones, are planned for less violent conditions than during Checkout-2, the simulation of flow-channel boundary conditions took precedence over simulation of distances available for fuel movement. The pin contains mixed oxide, highly-enriched in ^{235}U. Cladding is Type 316 stainless steel, with wall thickness and diameter the same as that for the FFTF reference fuel design. This pin is from the PFR fuel-development effort of the UKAEA, supplied for a series of joint TREAT experiments. Because of the high thermal-neutron cross section of the sample, the loop is enclosed in a

---

*Stewart, R. R., Dickerman, C. E., Stalic, N. R., and Doe, W. B., A Study of the Physical Properties of Nominal 0.7, 3, and 6 a/o Burnup UO_2 Fast-reactor Fuel Pins Preparatory to Transient TREAT Exposure, ANL-7571 (1969).

thermal-neutron shield (see Progress Report for December, ANL-7655, pp. 133-134) to reduce the power "spike" at the surface of the oxide. Calculations by transport theory predict that this thermal-neutron shield, which is thick enough to be essentially opaque to thermal neutrons, is worth ~3% Δk in TREAT. This calculation is in satisfactory agreement with measurement in TREAT. In order to compensate for most of this reactivity loss, the viewing slot for the neutron hodoscope has been filled in behind the loop. Background from the fuel in the slot, streaming past the loop sample, has been reduced by loading the slot with a 10-cm square cross-section, TREAT graphite dummy element between the slot fuel and the loop. This dummy thermalizes the neutrons from the slot fuel, which are then stopped from passing through the loop into the hodoscope by the loop thermal neutron shield.

In the absence of a shipping container for the loop (see Sect. IV.A.4.b below), it was necessary to ship the test pin separately from the meltdown loop ("B-3") for the experiment. During the report period, the B-1 loop and the thermal-neutron shield were used for a power-calibration run. The shield was removed from the B-1 loop and placed around the B-3 in preparation for the actual meltdown test.

Detailed results from the PFR pin tests are to be handled under the existing agreement between the USAEC and the UKAEA on data exchange.

b. <u>Experimental Support</u> (C. E. Dickerman)

Last Reported: ANL-7655, pp. 131-134 (Dec 1969).

(i) <u>Loop Operations</u>. The Mark-II Loop Operating Manual originally prepared for the checkout tests has been revised on the basis of actual experience at TREAT and routine improvements in the loop system. Revisions may be summarized as follows:

(a) deletion of one-time installation instructions needed for the checkout tests;

(b) change to strain-bridge pressure transducers (see Progress Report for November 1969, ANL-7640, pp. 133-136);

(c) changes in heater-power circuitry.

Drawings incorporating the changes have been supplied with the revised operating manual, which is designated as "Revision A." As additional revisions in the Operating Manual become necessary and as experience with the Mark-II system is accrued, these revisions will be keyed to specific page numbers or sections.

(ii) Shipping Cask. A data package consisting of the revised report for cask design, vendor shop drawings, ANL drawings of ANL-fabricated parts, and the ANL Quality Assurance Plan was submitted to the AEC on January 5, 1970 with a request for approval of the cask design. When approval is received, the order for cask fabrication will be issued to the vendor.

c. TREAT Operations (J. F. Boland)

Last Reported: ANL-7655, p. 134 (Dec 1969).

(i) Reactor Operations. Neutron radiographs were made of the capsules from experimental Subassembly XO33, one group of EBR-II driver-fuel elements, and 19 unirradiated EBR-II experimental capsules.

The reactor was reloaded for experiments using the Mark-II packaged sodium loop. Calibration irradiations of a three-rod cluster of UO_2 elements and a mixed-oxide PFR* pin were made under steady-state conditions. A PFR pin was loaded into a sodium-filled Mark-II loop and the instrumentation was checked out. Transient irradiation of the first PFR pin should be completed by February 6, 1970.

(ii) Development of Automatic Control System for Power Level. Preliminary tests of the hydraulic control-rod-drive system at the contractor's plant were witnessed during January. Minor modifications to the system should be completed by January 30, and an ANL representative will witness the final shop tests scheduled for the week of February 2. Shipment of the equipment is scheduled for the week of February 9.

5. Materials Behavior and Energy Transfer (M. G. Chasanov)

a. Theoretical Extrapolation of Measured Physical-property Data to Higher Temperatures

Last Reported: ANL-7632, pp. 138-139 (Oct 1969).

Information on high-temperature physical properties of materials of interest to fast reactor safety is becoming available as the result of various experimental programs at ANL and other laboratories. However, although the temperatures at which these data were obtained are very high from an experimental point of view (up to 3600°K), they are still markedly less than temperatures of interest to fast reactor safety analyses (up to 10,000°K). To correlate and extrapolate the experimental data for utilization at these significantly higher temperatures satisfactorily, recourse to existing theory is necessary.

*British Prototype Fast Reactor.

The scaled-particle theory has had outstanding success in cal-culations of physical properties of molten salts.* We have made some preliminary calculations for liquid UO_2 based on this theory. The theory requires only two input parameters: the density of the liquid and the dis-tance of closest approach of the ions. In the absence of density data much above the melting point, we employed the estimates of liquid density of Robbins** for a critical temperature of 10,000°K. The distance of closest approach was chosen to be the sum of the ionic radii at the melting point; a corresponding-states behavior was assumed for higher temperatures.

Using the equations given by Reiss,* we calculated surface tension, compressibility, and volume expansivity for UO_2 at the melting point; the results were of the correct magnitude. These properties were then computed at higher temperatures; the results are shown in Table IV.A.2. At present, there is no way to establish the accuracy of these values. How-ever, as physical-property data at higher temperatures become more available, a test of this theory for use with UO_2 should be possible.

TABLE IV.A.2. Calculated Physical Properties of Molten UO_2 Based on Scaled-particle Theory

Temp (°K)	Surface Tension (dynes/cm)	Isothermal Compressibility (cm^2/dyne x 10^{12})	Volume Expansivity (°K^{-1} x 10^5)
4000	830	2.7	8.8
5000	750	4.0	9.1
6000	580	6.9	9.3
7000	460	10	9.4
8000	410	13	9.4

6. 1000 MW(e) Safety Analysis Studies

a. Contract Management, Technical Review, and Evaluation (L. W. Fromm)

Last Reported: ANL-7632, pp. 139-140 (Oct 1969).

(i) Babcock & Wilcox Co. Subcontract

(a) Phase I: Malfunction and Safety Problem Survey. The Phase-I work has been completed and the Phase-I report, Fault Trees and Malfunction Catalog (BAW-1344), is being reviewed.

---

*Reiss, H., Advances in Chemical Physics IX, 1 (1965).
**Robbins, E. J., Limits for the Equation of State of Uranium Dioxide, TRG 1344 (R) (1966).

(b) Phase II: Accident Analysis and Selection of Safety Features. Phase II is proceeding on schedule. B&W completed the studies of flow abnormalities; the results are being documented. Studies of reactivity-insertion accidents, reactivity-coefficient calculations, and fuel-assembly bowing are being reported.

The B&W studies to identify the possible violent events in a single-pin failure or a chain of pin failures have been initiated. Efforts continue to evaluate the response of core structures to accident conditions and to study the sodium-vapor explosions. Difficulties encountered by B&W in getting the SAS1A code operational have been resolved.

Work by B&W continued on the identification and review of candidate safety features. The list of required protective actions generated in the Follow-on Study was reviewed in terms of the Phase-I and early Phase-II results. No significant changes were identified. The scoping investigation of the post-DBA cooling system was completed, major emphasis was on a transient-temperature analysis of the external meltdown pan to define the magnitude of the potential melt-through problem. B&W reviewed the existing safety features on the 1000-MWe LMFBR reference concept; the various safety functions performed by these design safety features have been cataloged.

Other studies either initiated or continued by B&W include: a survey of reactor internal components to determine their potential effects on the primary containment, study of methods to incorporate an energy absorber radially around and below the core, study of candidate methods of core support as related to the cover structure, and study of the potential for installing a machinery dome over the primary-tank cover.

Work is continuing at B&W on producing input data for calculations on fires in the secondary containment.

7. Violent Boiling (R. O. Ivins)

a. Particle Heat-transfer Studies (D. R. Armstrong)

Last Reported: ANL-7595, p. 120 (July 1969).

(i) Transient Boiling from a Single Solid Sphere. The transient boiling phenomenon associated with the contact of hot fuel fragments with sodium is being investigated. Initial experiments involve measuring temperature and pressure behavior when single spheres are rapidly immersed in sodium.

The experimental apparatus has been constructed, and the mechanical equipment and instrumentation are being checked. Although

preliminary tests with water as the quenching medium showed that all instrumentation performed well and that good reproducibility of data was achieved in duplicate runs, it was observed that the impact of the falling-sphere assembly induced a shock that was recorded by the pressure transducers and sonic detector. This shock, which persisted for about 0.5 sec and masked the output from these instruments, made detection of other signals during this interval practically impossible. The apparatus is being modified to reduce this effect. After the modifications are made, the apparatus will be sealed in a drybox and tests will be conducted with sodium.

    b.   Violent Boiling with Molten Fuel and Sodium (D. R. Armstrong)

      (i)   Fragmentation and Mixing Experiments (D. Cho)

        Last Reported: ANL-7632, p. 140 (Oct 1969).

To establish a relationship between the extent of breakup and boiling characteristics of the coolant, studies of fragmentation of molten tin quenched in water have continued. Correlations developed in these studies will be evaluated in future experiments with reactor materials (e.g., molten stainless steel in sodium).

Experiments were conducted to examine the effects of molten-metal temperatures as well as different degrees of water subcooling. The results indicate that there is a certain range of molten-metal temperature for which violent boiling enhances fragmentation ("violent-boiling range"). For water at 22°C (subcooling of 78°C), the violent-boiling range was from 300 to 600°C. This range changed little when the entrance velocity of the quenched tin was varied from 100 to 773 cm/sec. The observed violent-boiling range seems to coincide with the maximum-heat-flux region of subcooled boiling of water. Moreover, it appears that increasing the degree of subcooling results in shifting the violent-boiling range toward higher tin temperatures and in increasing the extent of fragmentation. However, because the data are limited, it is difficult to make a quantitative comparison with the known characteristics of boiling of subcooled water. Additional runs are being made to complete the data.

    c.   Simulations of Fuel Dispersal (J. J. Barghusen)

      Last Reported: ANL-7632, pp. 141-142 (Oct 1969).

The first draft of a work plan concerning simulation of fuel dispersal has been completed.

d. Mathematical Models of Fuel-Coolant Dynamics
(D. R. Armstrong)

(i) Fuel-Sodium Interaction and Heat Transfer Leading to
Pressure Generation

(a) Parametric Model of Pressures due to Dispersal of
Molten Fuel (D. Cho)

Last Reported: ANL-7632, p. 143 (Oct 1969).

As part of detailed modeling efforts, studies have been
made of the expansion of the cold bubble suddenly formed in a hot liquid.
The studies represent a first step toward examining the case in which cool-
ant is entrapped or dispersed in molten fuel.

The problem considers an inert-gas bubble initially at
temperature T_0 suddenly formed in an infinite volume of liquid initially at
temperature T_∞ ($>T_0$). The bubble is initially in mechanical equilibrium
with the surrounding liquid. As heat transfers from the hot liquid into the
cold bubble, the bubble pressure increases, causing expansion of the bubble.
The course of pressure rise and bubble growth is determined by the inter-
action between two competing processes: the heating of the bubble, and the
bubble expansion. The problem involves simultaneous solution of the
equations of state, motion, and energy. The bubble is assumed to be an
ideal gas. The motion of the bubble wall is described by the extended
Rayleigh equation. The energy equations (which are partial differential
equations) are reduced to ordinary differential equations by the integral
method. The resulting set of ordinary differential equations are solved
numerically.

Two limiting cases have been examined: in Case I, the
heat-transfer process is controlled by the bubble phase; in Case II, the
process is controlled by the surrounding liquid medium. Case I assumes
a liquid constant temperature (T_∞) at the bubble wall; Case II assumes a
uniform bubble temperature (T_b). The thermal conductivity of a gas is
much lower than that of a liquid, so Case I is a better approximation.

The studies have revealed the following salient features
of the problem:

1. Initially, the bubble pressure rises above the final
equilibrium value. (In the absence of surface tension, the equilibrium value
is equal to the ambient pressure.) The initial rise of the bubble pressure is
followed by a damped oscillation about the equilibrium value. The bubble
radius oscillates in a similar manner. The oscillations are damped even

when the surrounding liquid is inviscid. Such damping is attributed to the irreversible effect of heat transfer. Heat transfer occurs in such a way that the overexpansion or overcontraction of the bubble is impeded.

2.   The most important parameter that determines the mode of pressure rise and bubble growth is $P_\infty R_0^2 / \rho \alpha_{b_0}^2$ for Case I, and $(\rho_{b_0} C_{v_b} / \rho C_p)^4 (P_\infty R_0 / \rho \alpha^2)*$ for Case II, where P_∞ is liquid initial pressure, R_0 is initial radius of bubble, ρ is liquid density, α_{b_0} is $k_{b_0} / \rho_{b_0} C_{P_b}$, k_b is initial thermal conductivity of bubble, ρ_{b_0} is initial density of bubble, C_{P_b} is specific heat at constant pressure of bubble, C_{v_b} is specific heat at constant volume of bubble, and α is $k / \rho C_p$; k is liquid thermal conductivity, ρ is liquid density, and C_p is liquid specific heat at constant pressure. When the parameter (either of the two, as the case may be) is sufficiently smaller than unity, the growth of the bubble can be approximated by an instantaneous heating followed by isothermal expansion. The initial rise of the bubble pressure is maximum in this case. When the parameter is sufficiently larger than unity, the growth of the bubble may be approximated by a constant-pressure process ("heat-transfer-controlled growth"). However, the actual criteria depend somewhat on the value of T_∞ / T_0.

3.   In most cases, the viscosity and the surface tension of the surrounding liquid have only negligible effects on the initial value of the pressure rise. As expected, viscosity contributes to the damping of the oscillations, and the final equilibrium values of the bubble pressure and radius depend on surface tension.

The results of a sample calculation is presented in Fig. IV.A.1, where P_b is bubble pressure, R is bubble radius, T_b is bubble temperature (Case II), and T_s is temperature at the bubble center (Case I). The calculation describes the expansion of a cold air bubble suddenly formed in molten glass. Both Cases I and II are presented for the purpose of illustration, although Case I is more realistic. The conditions and property values used are: P_∞ = 1 atm, T_∞ = 1500°K, k = 0.0035 cal/sec-cm-°C, C_p = 0.3 cal/g-°C, ρ = 2.5 g/cm³, viscosity μ = 100 poise, surface tension σ = 150 dynes/cm for the liquid glass, and T_0 = 300°K, R_0 = 0.1 cm, k_b = 0.00015 cal/sec-cm-°C, C_{P_b} = 0.25 cal/g-°C, C_{P_b}/C_{v_b} = 1.4, and ρ_{b_0} = 0.00118 g/cm³ for the air bubble. For Case I, the value of parameter $P_\infty R_0^2 / \rho \alpha_{b_0}^2$ is 1.6 x 10⁴; for Case II, the parameter is

---

This is true when $(\rho_{b_0} C_{v_b} / \rho C_p) \ll 1$. In an unlikely case where $(\rho_{b_0} C_{v_0} / \rho C_p) \gg 1$, the parameter should be $(\rho_{b_0} C_{v_b} / \rho C_p)^2 (P_\infty R_0^2 / \rho \alpha^2)$.
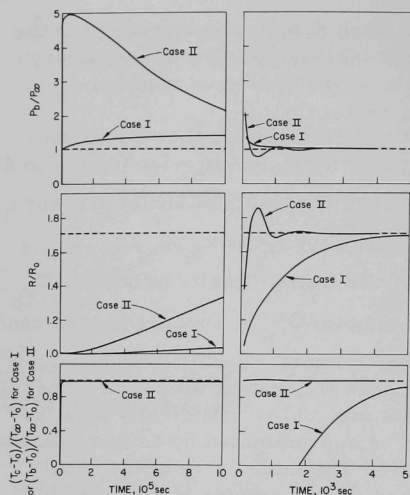
Fig. IV.A.1

Expansion of an Air Bubble Suddenly Formed in Molten Glass. (Broken lines indicate final equilibrium values.)

1.43×10^{-8}. As expected from the discussion above, Case I does not differ much from a constant-pressure growth, but Case II represents a process of nearly instantaneous heating followed by isothermal expansion. The rapid damping of the oscillations is due to the high viscosity of the glass melt.

8. Post-accident Heat Removal (R. O. Ivins)

a. Engineering Analyses (J. C. Hesson)

(i) Thermally Stable Fuel-debris Configurations in Sodium

Last Reported: ANL-7640, pp. 137-138 (Nov 1969).

In a study of the cooling of porous piles of fuel debris by natural convection of sodium, analyses of heat removal from collapsed or molten cores under liquid sodium are continuing. Recent work includes studies of the cooling of porous piles or beds of fuel debris by natural convection of liquid sodium.

If a porous pile of pieces of fuel debris exists under liquid sodium, the fission-product decay heat in the fuel debris will cause a thermal-convection circulation of the sodium up through the porous pile. The driving force for this circulation is the pressure due to differences in densities between the sodium in the pool and the heated sodium in the porous pile. The resistance to the circulation is the flow friction loss through the porous pile. The circulating sodium removes heat from the pile and, for a pile sufficiently small, will keep the pile from overheating and melting.

An equation was developed to calculate the maximum depth of a uniform pile of fuel pieces under sodium that can be cooled by natural convection of the sodium. The sodium is assumed to have free entry to the bottom of the pile and free exit from the top of the pile.

In this discussion, condition 0 refers to subcooled liquid sodium, condition 1 refers to boiling or saturated liquid sodium, and condition 2 refers to saturated sodium vapor. These conditions are indicated by the corresponding subscripts. The sodium in the pool can be subcooled (condition 0) or boiling (condition 1). If it is subcooled, it can leave the top of the pile as all liquid, all vapor, or as a mixture of vapor and liquid. If saturated, it will leave the top of the pile as all vapor or as a mixture of vapor and liquid.

The equation is general in that it can be used for any of the above cases. Computations indicate that if the sodium in the pool is considerably subcooled, a maximum value of depth will occur when the sodium leaves the top as a boiling or saturated liquid (condition 1). The equation also shows that if the sodium in the pool is boiling (condition 1), a maximum depth will occur when the sodium leaves the top as a saturated vapor (condition 2).

The equation for the maximum depth of the pile is

$$L = \left[\frac{\Delta H}{q} \left(\frac{\epsilon}{1-\epsilon} \right)^{\frac{3}{2-n}} (\phi D)^{\frac{1-n}{2-n}} \right]$$

$$\left\{ \left(\frac{1}{6^{1+n}} \right) \left(\frac{g}{m} \right) \left(\frac{\rho_0^2}{\mu_1^n} \right) \frac{L_1 \left[1 - \frac{1}{\frac{\rho_0}{\rho_1} - 1} \ln \frac{\rho_0}{\rho_1} \right] + L_2 \left[1 - \frac{\rho_1}{\rho_0} \frac{1}{\frac{\rho_1}{\rho_2} - 1} \ln \frac{\rho_1}{\rho_2} \right]}{L_1 \left[\frac{1 + \frac{\rho_0}{\rho_1}}{2} \right] + L_2 \left(\frac{\mu_2}{\mu_1} \right)^n \frac{\rho_0}{\rho_1} \left[\frac{1 + \frac{\rho_1}{\rho_2}}{2} \right]} \right\}^{\frac{1}{2-n}}$$

(1)

where D = effective diameter of particles in cm, g = acceleration due to gravity in cm/sec², ΔH = heat difference in sodium between (entrance and exit) conditions in cal/g, q = decay heat rate in fuel in cal/sec-cm³, L = depth of bed in cm, L_1 = depth of bed at condition 1 in cm, L_2 = depth of bed between conditions 1 and 2 in cm, m = friction-factor coefficient (0.7 for turbulent flow Re > 2, or 5.0 for viscous flow Re < 2),* n = friction-factor exponent (0.15 for turbulent flow, or 1.0 for viscous flow),

*Perry, J. H.(Ed.), Chemical Engineer's Handbook, 3rd Ed., McGraw-Hill Book Co., Inc., (1950), p. 394.

ϕ = particle-shape factor (1 for spheres), ϵ = fraction void in bed, ρ = sodium density in g/cm^3, μ = sodium viscosity in poise, and L_1/L_2 = $\Delta H_1/\Delta H_2$ = ratio of heats required to heat sodium from conditions 0 to 1 and 1 to 2.

The equation is based on uniform flow through the bed and additive or homogeneous volume relationship for two-phase flow. The value of L is affected only slightly if other types of two-phase flow relationships are used.

As an example, sodium at its boiling point 900°C (1.18 atm) enters the bottom of the pile and all is evaporated just as it reaches the top of the pile. Table IV.A.3 shows pertinent sodium values. In this case, the flow is turbulent and m = 0.7, n = 0.15, L_1 = 0 and L_2 = L. On substituting these values in Eq. (1) we have

$$L = \frac{480}{q} \left(\frac{\epsilon}{1-\epsilon}\right)^{1.621} (\phi D)^{0.621}$$

If ϕ = 1 (spheres), D = 1 cm, ϵ = 0.354 and q = 6 cal/sec-cm^2, then L = 30 cm.

TABLE IV.A.3. Sodium Properties

	Condition		
	0 (subcooled liquid)	1 (saturated liquid)	2 (saturated vapor)
Temperature, °C	300	900	900
Density ρ, g/cm^3	0.8805	0.7343	0.0003146
Specific volume v, cm^3/g	1.1357	1.3618	3178
Enthalph H, cal/g	0.0	180	921
Viscosity μ, 10^{-4} poise	34.0	16.7	1.97

As a second example, subcooled sodium at 300°C enters the pile and just reaches its boiling of 900°C (1.18 atm) as it leaves the top of the pile. In this case, the flow is also turbulent and m = 0.7, n = 0.15, L_2 = 0, L_1 = L. On substituting in Eq. (1),

$$L = \frac{1080}{q} \left(\frac{\epsilon}{1-\epsilon}\right)^{1.621} (\phi D)^{0.621}$$

If ϕ = 1, D = 1 cm, ϵ = 0.354, and q = 6 cal/sec-cm^2, then L = 68 cm.

In using the above equation, values of the properties of sodium as well as parameters involving the porous bed of fuel particles are needed. In general, the necessary values of sodium properties are available; however, pertinent values for the porosity ϵ, the effective particle diameter D, and the shape factor ϕ, for porous piles of fuel that might be formed are largely unknown and must be estimated. Future experimental work involving interactions of molten fuel should enable better estimates of these parameters.

PUBLICATIONS

Studies of Fast Reactor Fuel Element Behavior under Transient Heating to Failure. III. In-pile Experiments on Irradiated UO_2 Fuel Pins in the Absence of Coolant
   R. R. Stewart, C. E. Dickerman, L. E. Robinson, and W. B. Doe
      ANL-7552 (March 1969)

A Study of the Physical Properties of Nominal 0.7, 3, and 6 a/o Burnup UO_2 Fast-Reactor Fuel Pins Preparatory to Transient TREAT Exposure
   R. R. Stewart, C. E. Dickerman, N. R. Stalica, and W. B. Doe
      ANL-7571 (May 1969)

PUBLICATIONS